Aus der Abteilung für Klinische Pharmakologie
Leiter: Prof. Dr. med. Stefan Endres
Medizinische Klinik und Poliklinik IV
Klinikum der Universität
Ludwigs-Maximilians-Universität München
Direktor: Prof. Dr. M. Reincke

Characterization of MAVS-dependent antiviral signaling

Dissertation

zum Erwerb des Doktorgrades der Naturwissenschaften
an der Medizinischen Fakultät
der Ludwig-Maximilians-Universität München

vorgelegt von
Friederike Saathoff
aus Hannover
2014

Gedruckt mit Genehmigung der Medizinischen Fakultät

der Ludwig-Maximilians-Universität München

Betreuerin: Prof. Dr. med. Dr. rer. nat. Carole Bourquin

Zweitgutachter: Prof. Dr. rer. nat. Karl-Klaus Conzelmann

Mitbetreuung durch die promovierten Mitarbeiter:

Prof. Dr. med. Simon Rothenfusser

Dekan: Prof. Dr. med. Dr. h.c. M. Reiser, FACR, FRCR

Tag der mündlichen Prüfung: 17.12.2014

„Der Mensch muss das Gute und Große wollen,

der Rest hängt vom Schicksal ab.“

Alexander von Humboldt (1769-1859)

Meinen Eltern Reinhard und Barbara,

sowie meinem Bruder Jan-Hinnerk

Erklärung nach § 7 Abs. 4 der Promotionsordnung vom 16. Juli 2010

Hiermit versichere ich, dass diese Dissertation selbstständig angefertigt wurde, ich mich außer den angegebenen Hilfsmitteln keiner weiteren bedient habe und alle Erkenntnisse, die aus dem Schrifttum ganz oder annähernd übernommen wurden, als solche kenntlich gemacht und nach ihrer Herkunft unter Bezeichnung der Fundstelle einzeln nachgewiesen sind.

Des Weiteren versichere ich, dass die hier vorgelegte Dissertation nicht in gleicher oder in ähnlicher Form bei einer anderen Stelle zur Erlangung eines akademischen Grades eingereicht wurde.

München, den 20.06.2014

.....

Friederike Saathoff

Table of contents

1 Introduction

1.1 General principles of innate immune responses

Infection of multicellular organisms by microbial pathogens leads to an inflammatory response by the immune system. The innate immune system is thereby the first-line of defense against microorganisms, such as bacteria, fungi and viruses, and the main contributor to acute inflammation [1]. The system primarily depends on the recognition of pathogen associated molecular patterns (PAMPs) and damage associated molecular patterns (DAMPs) by innate receptors. PAMPs do not occur in the host and are usually molecules essential for the life cycle and viability of a pathogen. Thus, PAMPs are highly conserved, making them an ideal target for recognition. Examples include bacterial and viral nucleic acids, fungal β-glucan and α-mannan cell wall components, the bacterial protein flagellin, components of the peptidoglycan bacterial cell wall, and lipopolysaccharide (LPS) from Gram-negative bacteria. DAMPs, also known as alarmins, are endogenous molecules normally found in cells that get released during necrosis and contribute to sterile inflammation. Examples include ATP, the cytokine IL1α, uric acid, the calcium-binding, cytoplasmic proteins S100A8 and S100A9, and the DNA-binding, protein HMGB1 [2, 3]. The germ line-encoded receptors for PAMPs and DAMPs are highly conserved in all multicellular organisms and are collectively referred to as pattern-recognition receptors (PRRs) [4]. PRRs include membrane bound receptors, such as Toll-like receptors (TLRs) and C (calcium dependent)-type lectin receptors (CLRs) as well as cytosolic receptors such as retinoic acid-inducible gene I (RIG-I)-like receptors (RLRs). PRRs are not only expressed in specialized immune cells like macrophages and DCs but also in many other cell types.

Sensing of PAMPs or DAMPs by PRRs results in transcriptional up-regulation of genes encoding for pro-inflammatory cytokines, type I interferons (IFNs), chemokines and antimicrobial proteins, as well as many uncharacterized proteins [5]. NLRs *e.g.* are known to additionally regulate interleukin-1ß (IL-1ß) maturation through the activation of caspase-1 [6]. These initial, locally restricted, immune responses limit replication and expansion of the pathogen (*e.g.* viruses) and can in turn convert resting dendritic cells (DCs) into potent antigen-presenting cells, capable of promoting the expansion and effector differentiation of naive pathogen-specific T cells [7, 8]. PRR-induced IFN is also required to promote T cell survival and clonal expansion after antigen presentation [9] Moreover, interferon potently induces the cytolytic activity of natural killer cells and cytotoxic lymphocytes [10] and plays an

important role in promoting B cell differentiation and antibody production [11]. On the other hand, PRRs can (directly) function as co-stimulatory molecules for antigen-specific T cell responses and participate in the maintenance of T cell memory [12, 13].

Nucleic acid motifs are the main virus-derived PAMPs to be recognized by the innate immune system. Four classes of PRRs have been shown to be involved in the recognition of viral nucleic acids by the innate immune system: TLRs, RLRs, NLRs and Cyclic GMP-AMP synthase (cGAS) [14, 15]. Viral RNA is sensed by TLR3, TLR7 and TLR8 in the endosomes of pDCs and myeloid DCs [16-18] and in the cytosol of many cell types by RLRs [19, 22-24], and a subset of NLRs [25, 26].

1.2 RIG-I-like receptors (RLR)

RLR proteins are key players of antiviral innate immunity and act by recognizing viral RNA in the cytosol. The RLR protein family comprises three members: the retinoic acid-inducible gene I (RIG-I) [27], melanoma differentiation-associated gene 5 (MDA5) [28] and laboratory of genetics and physiology-2 (LGP2) [29].

RLRs belong to the superfamily 2 (SF2) helicases/ATPases and share a central ATP-dependent helicase domain as well as a carboxy (C)-terminal regulatory (RD) domain. In addition, RIG-I and MDA5 each bear two amino (N)-terminal caspase-recruitment domains (CARDs), which are essential for protein-protein interactions with the downstream signaling molecule mitochondrial anti-viral signaling (MAVS) [27, 30].

Due to a differing affinity for RNA patterns, RIG-I and MDA5 recognize different RNA viruses with partial overlap [19]. Activation of RIG-I depends on RNAs of a minimal length of 18 to 20 bases that carry a triphosphate moiety at the 5’-end and a base-paired region in the range of 10 to 20 nucleotides in the direct proximity of the free 5’-triphosphate end [31, 32]. RIG-I is thus required for innate responses to many ssRNA viruses, such as the negative-stranded viruses of the orthomyxoviridae *e.g.* influenza A and B virus, paramyxoviridae *e.g.* Newcastle disease virus (NDV), Sendai virus (SeV), respiratory syncytial virus (RSV) and measles virus and rhabdoviridae *e.g.* vesicular stomatitis virus (VSV) and rabies virus [20, 24]. Moreover, detection of positive-stranded flaviviruses including hepatitis C virus (HCV) and Japanese encephalitis virus (JEV) was found to be RIG-I-dependent [33]. In addition, RIG-I can also be activated by cytoplasmic DNA after RNA polymerase III-mediated transcription of AT-rich DNA into RNA [34, 35].

MDA5-dependent signaling is induced by long double-stranded RNA (dsRNA), most likely involving a complex RNA structure [36]. Up to now however, the structures serving as the MDA5 PAMP, are not entirely elucidated. For *in vitro* studies, the commercially available

RNA analog poly (I:C) is widely used as an MDA5 ligand. *In vivo*, MDA5 is required for protection against picornaviruses such as the polio virus, encephalomyocarditis virus (EMCV), Theiler's virus, mengovirus, norovirus and murine hepatitis virus [22, 23, 37]. Similarly to RIG-I, MDA5 has also been implicated in DNA virus detection. Vaccinia virus, a dsDNA virus of the poxvirus family, activates MDA5 via a yet to be characterized mechanism [36].

Even though LGP2 has significant sequence identity within the helicase domain and RD to RIG-I and MDA5 it lacks CARD domains and therefore cannot induce signaling on its own. It is supposed to have regulatory functions on RIG-I and MDA5, however the functions of the protein in antiviral signaling have remained controversial, as different experimental strategies have demonstrated seemingly antithetic biological activities for Lgp2 [38].

In addition to the immediate innate immune response, RLR signaling also affects adaptive immune responses by driving the maturation of dendritic cells and other antigen presenting cells (APCs) in order to induce tailored T-cell responses to viral infection [39, 40]. These parameters serve to control cell-mediated defenses and modulate the adaptive immune response to virus infection. Thus, the development of RLR-based therapies that trigger specific innate immune programs and lead to selective effector gene expression and function have a beneficial impact on the control of virus infection and antiviral immune enhancement against both chronic and acute viral infections and have already been successfully tested in several studies [21, 41, 42]. RLR-induced immune responses can furthermore be exploited for anti-tumor therapy approaches. Targeting tumor cells with bifunctional triphosphate RNA to induce RLR-mediated immunogenic cell death in these cells in combination with small interfering RNA (siRNA) to disrupt tumor-promoting pathways have proven to beneficial in several studies on tumor models [43-45].

1.3 The antiviral receptor protein MAVS

Upon activation, RIG-I and MDA5 undergo conformational changes and can bind via CARD-mediated interactions to their shared adaptor protein MAVS, also known as Interferon promoter stimulator-1(IPS-1), Caspase recruitment domain (CARD) adaptor inducing IFN-β (Cardif) and Virus-induced signaling adaptor (VISA) [46-49]. In addition to a single N-terminal CARD, the protein bears a proline rich region (PRR) and a C-terminal transmembrane (TM) domain. MAVS was initially described as a strictly mitochondrial outer membrane (OM) protein with its localization being crucial for signal activation [49]. In a later report, MAVS has also been shown to locate to peroxisomes, and both localizations are thought to be necessary for an adequate antiviral response [50].

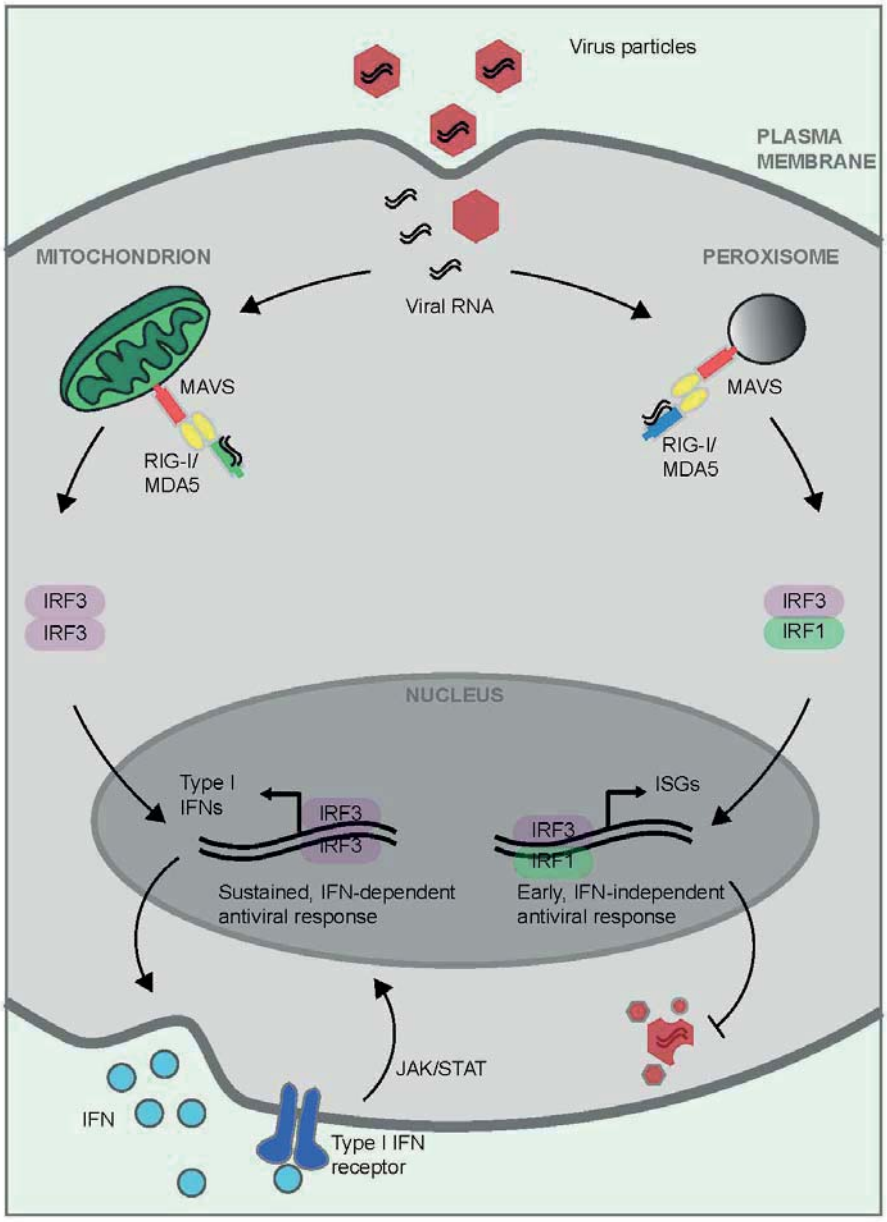

Figure 1-1 Illustrations of differential RLR signaling via mitochondria and peroxisomes. Upon activation by viral RNA the receptors RIG-I and MDA5, undergo conformational changes and bind to MAVS both on mitochondria and peroxisomes. Mitochondrial MAVS initiates antiviral signaling via activation of the transcription factor IRF3, leading to a sustained antiviral response with expression of type I IFNs and subsequent induction of ISGs via JAK/STAT signaling. Peroxisomal MAVS induces ISGs in an IFN-independent manner, induced by activation of IRF3/IRF1 heterodimers. Activation of peroxisomal MAVS results in an early and transient antiviral response, supplementing the longer sustained mitochondrial mediated antiviral response.

Upon activation by RLRs, mitochondrial MAVS homo-oligomerizes and activates antiviral signaling by recruiting various downstream signaling molecules to form a MAVS “signalosome” [51]. Association of tumor necrosis factor (TNF) receptor associated factor (TRAF) 3 and TRAF6, as well as TRAF family member-associated nuclear factor κ B (NF-κB)

activator (TANK) and TNF receptor 1-asscociated death domain protein (TRADD) lead to the phosphorylation of interferon regulatory factor 3 (IRF3) and IRF7 by the TANK binding kinase 1 (TBK1) and IKKε, as well as activation of NF-κB to induce type I interferons (IFNs) and proinflammatory cytokines (*e.g.* interleukin 6), respectively. The PRR domain of MAVS contains consensus binding sites for various proline-associated immune proteins, such as TRAF2, TRAF3 and TRAF6 [47, 52]. The protein has also been shown to interact with FADD and RIP1 [53, 54]. Upon virus infection, the CARDs of MAVS form prion-like fibrils which convert MAVS into functional aggregates on the mitochondrial membrane, leading to the recruitment of E3 ligases TRAF2, TRAF5, and TRAF6 and the activation of IKK and TBK1 [55].

MAVS activation on peroxisomes creates rapid and transient antiviral signaling. Upon activation of peroxisomal MAVS, TRAF3 and TRAF6 are recruited to stimulate phosphorylation of IRF3 and IRF1. This leads to direct stimulation of ISGs, independent of IFN expression [50].

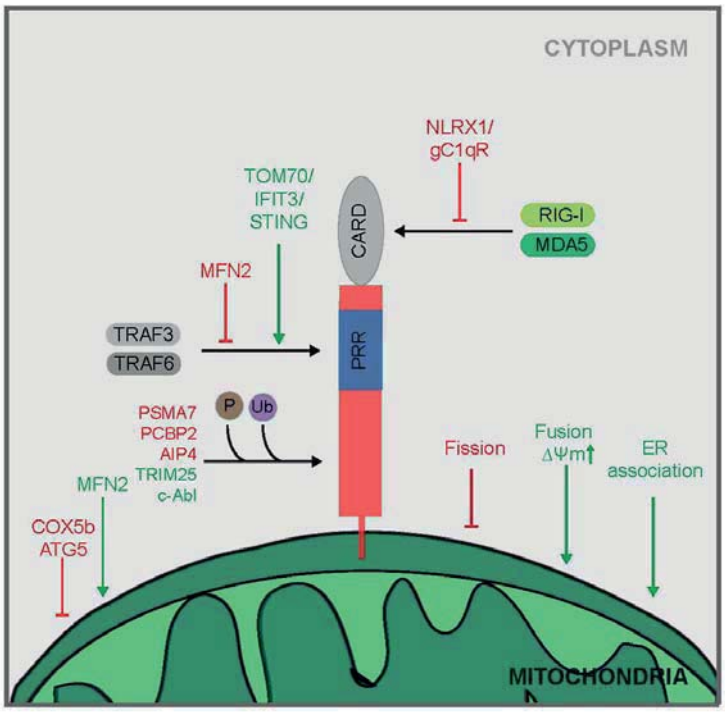

Figure 1-2 Mechanisms of MAVS regulation. MAVS is tightly regulated by host cell factors that inhibit MAVS signaling by direct protein–protein interactions, by altering mitochondrial properties or dynamics, or by post-translational modifications. Positive regulations of MAVS signaling are shown in green, negative regulations of MAVS signaling are shown in red.

Several proteins regulate antiviral signaling by direct interaction with MAVS. Following RIG-I, but not MDA5 activation, the stimulator of interferon genes (STING) interacts with MAVS at

MAMs, facilitating TBK1 recruitment [56, 57]. The nod like receptor 1 (NLRX1) interacts with MAVS via its CARD and is postulated to disrupt formation of the signalosome [58]. Interestingly, NLRX1 selectively inhibits signaling of mitochondrial MAVS, whereas signaling of peroxisomal MAVS is unaffected [50]. The mitochondrial proteins mitofusin 2 (MFN2) and translocase of the outer mitochondrial membrane 70 (TOM70) both interact with MAVS to inhibit and activate signaling, respectively [59, 60]. The receptor for globular head domain of complement component C1q (gC1qR) was shown to translocate to mitochondria to negatively regulate signaling via direct interaction with MAVS [61]. The IFN induced protein tetratricopeptide repeats 3 (IFIT3) is a positive regulator of MAVS signaling, facilitating interactions of TBK1 and MAVS [62].

Additionally, post-translational modifications play a key role in regulation of MAVS-dependent antiviral responses. The proteasomal component PSMA7, poly(rC) binding protein 2 (PCBP2), tripartite motive protein 25 (TRIM25), Ndfip1 and the Nedd4-like E3 ubiquitin ligase AIP4 can stimulate ubiquitination of MAVS and promote proteasomal degradation of the protein [63-66]. Phosphorylation of MAVS can both activate and inhibit antiviral signaling. Phosphorylation at Thr234 by a yet unknown kinase facilitates binding of polo-like kinase 1 (PLK1), thereby blocking interaction with TRAF3. The tyrosine kinase c-Abl was identified as a positive regulator of MAVS by direct interaction and phosphorylation [67]. An overview of regulation mechanisms of MAVS on the mitochondrial surface is shown in Figure 1-2.

Even though the physiological importance of many of these protein interactions remains to be determined, it is now established that upon activation, MAVS forms a signaling scaffold whereby the recruitment of TNF-receptor-associated factor (TRAF) 3 leads to the induction of IFN-dependent responses whereas the recruitment of TRAF6 leads to the inflammatory response [1].

1.4 Mitochondria

1.4.1 Structure and morphology of mitochondria

Mitochondria are double-membrane bound organelles, forming four compartments with distinct functions: the outer membrane (OM), intermembrane space (IMS), inner membrane (IM) and matrix [68]. The composition of the OM is similar to that of other eukaryotic membranes and the presence of porins permits free transportation of metabolites and molecules of less than 10 kDa into the inter-membrane space. In contrast, the IM resembles prokaryotic membranes in its physiological properties and composition. The protein/lipid ratio is significantly higher compared to the OM and the membrane is very rich in cardiolipin (CL),

a lipid found also in bacterial membranes. CL is crucial for the proper activity of several IM enzymes and responsible for the convolution of the inner membrane into cristae-structures, the site of oxidative phosphorylation (OXPHOS). The IMS contains proteins (*e.g.* cytochrome C, DIABLO/Smac), which play a major role in energy homeostasis and apoptosis. The matrix is composed of proteins involved in the citric cycle reaction [69]. In addition, it contains a circular 16 kb genome (mtDNA) encoding for 13 proteins of the respiratory chain as well as for mitochondrial rRNAs and tRNAs. Unlike nuclear genomes, which are inherited equally from both parents, the mitochondrial genome is strictly passed on along the maternal line [70] . This maternal inheritance pattern of mtDNA is due to its localization in the cytoplasm. When an egg is fertilized, the cells of the resulting embryo contain the mtDNA and cytoplasm of the egg, not the sperm. As the embryo continues to develop, all of the cells in the resulting human contain the cytoplasm and clonal mtDNA of the mother. Therefore, mitochondria-associated disease mutations are also always inherited maternally. Mutations in mtDNA lead to severe neuromuscular diseases mostly due to an impaired bioenergetic status [71].

Mitochondria form a tubular network throughout the cell. Their ultrastructure and distribution is highly dynamic and controlled by a continuous equilibrium of fusion and fission processes [72]. In addition, mitochondria are in close contact to the endoplasmic reticulum (ER) tethering at multiple contact sites to form specific domains termed mitochondria-ER associated membranes (MAMs). MAMs possess distinct biochemical properties and a characteristic set of proteins [73]

1.4.2 Function of mitochondria

Mitochondria are implicated in a variety of cellular functions. In addition to their function in aerobic respiration, apoptosis, aging and Ca^{2+}-homeostasis, mitochondria form an integral platform for innate immune signaling (Figure 1-3). Furthermore, mitochondria are tightly connected to cell cycle control [74] and alterations are observed in aging [75] and disease [76].

One of the most important functions of mitochondria is the production of energy in form of ATP by aerobic respiration. Mitochondrial respiration is composed of two intimately linked processes: the tricarboxylic acid (TCA) cycle and oxidative phosphorylation. In a first step nutrients (such as glucose, amino acids) are processed to metabolic intermediates (*e.g.* pyruvate, acetyl CoA) that are subsequently metabolized and decarboxylated by eight different enzymes in the tricarboxylic acid (TCA) cycle in the mitochondrial matrix. The decarboxylation steps are coupled to the transfer of electrons to NAD^+ producing NADH. During oxidative phosphorylation NADH is oxidized by complex I of the electron transport

chain (ETM) and free electrons are passed onto complex II, III and IV to reduce O_2 to H_2O in a series of redox reactions. This electron transfer results in pumping of protons through complexes I, III, and IV into the IMS. This creates a temporary form of stored energy, the protonmotive force (PMF), which is used by complex V to produce adenosine triphosphate (ATP) from adenosine diphosphate (ADP) and phosphate (P_i). Electron transfer through the respiratory chain and nutrient oxidation also produces reactive oxygen species (ROS) by electron leakage from complex I and III. Electron leakage to oxygen results in the formation of two types of superoxides, namely, O_2^- and H_2O^- in its anionic form [77]. At high enough concentrations ROS can activate the mitochondrial apoptotic machinery, which ultimately leads to cell death. However, at low concentrations ROS serve as important signaling molecules [78].

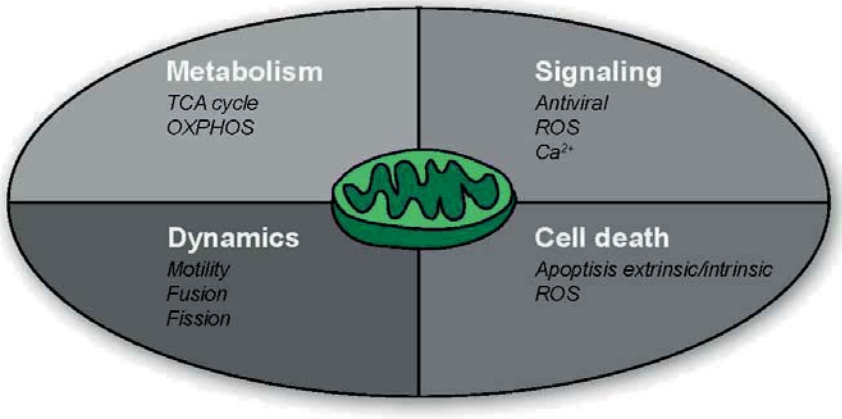

Figure 1-3 Overview of mitochondrial functions. Due to continuous fission and fusion processes, mitochondria are highly dynamic organelles. Mitochondria fuel cell processes by producing ATP through oxidative phosphorylation. The reactive oxygen species (ROS) generated as a byproduct of mitochondrial respiration are potent signaling molecules that can modulate protein functions. Additionally, the intracellular energy status as well as a variety of cellular stresses are detected and, in case of privation, mitochondria can respond with the initiation of cell death. Mitochondria play an essential role in antiviral defense and are modulating and are modulated by innate antiviral signaling.

Besides their function as the “powerhouse” of the cell, mitochondria are implicated in calcium (Ca^{2+}) sensing and signaling. By acting as a second messenger, Ca^{2+} regulates many cellular processes [79]. When transported into mitochondria, Ca^{2+} stimulates oxidative phosphorylation, which then results in faster respiratory chain activity and higher ATP output, meeting the cellular ATP demand [52].

Mitochondria are furthermore able to promote apoptosis [80-83]. Two major pathways, the extrinsic and the intrinsic are involved in triggering apoptotic cell death. The extrinsic pathway is initiated by the ligation of death receptors (*e.g.* tumor necrosis factor or Fas ligand

receptor) by their cognate ligands, leading to the recruitment of adaptor molecules such as FAS-associated death domain protein (FADD) and then caspase 8. This results in the dimerization and activation of caspase 8, which can then directly cleave and activate the effector caspases 3 and 7, ultimately leading to apoptosis of the cell [84].

The intrinsic apoptosis pathway can be induced by DNA damage or endoplasmic reticulum (ER) stress, which in turn activate B cell lymphoma 2 (BCL-2) homology 3 (BH3)-only proteins leading to BCL-2-associated X protein (BAX) and BCL-2 antagonist or killer (BAK) activation [81]. BAK and BAX promote mitochondrial outer membrane permeabilization (MOMP), leading to the release of proapoptotic molecules, such as cytochrome C and SMAC/DIABLO from the mitochondrial intermembrane space [80]. The release ultimately initiates activation via the apoptosome and caspase 9 of the effector caspases 3 and 7. Both the extrinsic and the intrinsic processes congregate at the activation of downstream effector caspase 3, which is responsible for inducing the morphological changes observed in an apoptotic cell, such as cell shrinkage, nuclear fragmentation, chromatin condensation and membrane blebbing [85]. Crosstalk between the extrinsic and intrinsic pathways occurs through caspase 8 cleavage and activation of the BH3-only protein BH3-interacting domain death agonist (BID). Activated BID (truncated BID; tBID) is required in some cell types for death receptor-induced apoptosis [83].

1.4.3 Mitochondria in antiviral signaling

Due to the localization of MAVS at the OM, mitochondria serve as signaling platforms for antiviral immune responses. In addition, mitochondrial function and morphology are intimately linked to antiviral signaling processes [59, 86-89].

Activation of RLR signaling induces elongation of mitochondria which increases mitochondria-ER tethering and facilitates MAVS downstream signaling [90]. This effect is mediated by an interaction between MAVS and an effector of the mitochondrial fusion machinery mitofusin 1 (MFN1), which is described to positively regulate MAVS-mediated signaling [88]. Furthermore, the mitochondrial membrane potential ($\Delta\Psi_m$) is crucial for MAVS-dependent signaling as reduction of $\Delta\Psi_m$ leads to abrogation of antiviral responses. For example over-expression of the mitochondrial protein, uncoupling protein-2 (UCP-2) to depolarize the membrane, greatly reduced MAVS dependent IFN production [86]. Upon activation, MAVS forms multimers on the outer mitochondrial membrane to propagate downstream signaling [55]. Loss of $\Delta\Psi_m$ might in turn prevent these structural rearrangements of the MAVS [86].

$\Delta\Psi_m$ is determined by the electrochemical gradient that forms along the mitochondrial membrane. Additionally, it is the driving force behind ATP-production. The $\Delta\Psi_m$ dependence therefore also links antiviral signaling to calcium uptake. Furthermore, mitochondrial ROS are reportedly involved in the RLR signaling pathway. Increase of mROS production, generated through mitochondrial respiration and accumulation of dysfunctional mitochondria, leads to enhanced IRF3 activation and IFN expression [91-93]. Ultimately, activation of RLRs also initiates pro-apoptotic signaling via mitochondria, independent of type I IFNs [94].

Some viruses show evolutionary adaptation to the profound role of mitochondria in antiviral signaling. Upon infection hepatitis C virus (HCV) expresses the serine protease NS3/4A and induces cleavage of MAVS from the membrane thus dislocating the protein from mitochondria. This greatly reduces the ability to induce interferon expression in HCV infected cells [95].

Taken together, mitochondria are playing an important role in host defense and are modulating and are also modulated by innate anti viral signaling.

1.5 Peroxisomes

1.5.1 Biogenesis and morphology of peroxisomes

Peroxisomes are organelles usually 0.1–1 µm in diameter bound by single membranes that enclose dense matrices primarily containing metabolic enzymes. Depending on cell type and environment, peroxisomes vary significantly in size and function. While usually spherical, peroxisomes can change their shape to be elongated with formation of reticular structures [96]. In addition, they are able to increase in size and number in coordination with morphological changes in other subcellular compartments, including mitochondria [97].

De novo synthesis of peroxisomes involves vesicular transport of peroxisomal membrane proteins from the ER. Peroxisomal membrane proteins (PMPs) insert into the ER and assemble into three pre-peroxisomal sub-complexes, which fuse after vesicular budding from the ER to form mature peroxisomal organelles [98]. In addition, mature organelles can multiply by growth and fission. Fission cycles begin with membrane remodeling and addition of vesicular structures from the ER. After elongation, the organelle becomes constricted by a yet unknown mechanism [99]. Interestingly, the fission step is regulated by GTPases also implicated in mitochondrial fission, namely the Dynamin-Like Protein 1 (DLP1) [100], mammalian Fission 1 (hFIS1) [101] and mammalian Mitochondrial Fission Factor (MFF) [102]. The molecular basis of peroxisomal biogenesis and protein import is highly dependent on the protein family of peroxins and will be described in more detail in section 1.5.3.

1.5.2 Function of peroxisomes

Peroxisomes play a central role in the regulation of metabolic processes in the cell, carrying out various oxidative reactions that are tightly regulated to adapt to the changing needs of the cell and varying external environments. A major function is the β-oxidation of many classes of fatty acids including very long, branched-chain, and polyunsaturated fatty acids. ß-oxidation is simultaneously present in mitochondria as well as in peroxisomes. However, processes are catalyzed by different enzymes and play functionally complementary roles [103, 104]. Catalyzing only a limited number of ß-oxidation cycles, peroxisomes act as a chain-shortening system in order to prepare medium chain fatty acids from very long chain fatty acids (>C20) for subsequent degradation in the mitochondrial ß-oxidation [105]. Peroxisomal β-oxidation results in generation of H_2O_2, which is degraded into H_2O and O_2 by the peroxisomal enzyme catalase. Furthermore, peroxisomes play a role in the production of bile acids important for the adsorption of fatty acids and fat-soluble vitamins, such as vitamins A and K in hepatocytes and bile duct cells [106]. The organelles are additionally implicated in the synthesis of phospholipids required by the nervous, immune and cardiovascular systems (plasmalogens) and are involved in signaling and the protection of cells from damage through reactive oxygen species (ROS) [107].

Peroxisomes and mitochondria share common metabolic functions as well as the members of their fission machinery, DRP1 and FIS1 [100, 108, 109]. In addition it has been shown that active interchange of metabolites, membrane proteins and lipids *e.g.* through vesicular transport between the organelles is possible [110-112].

1.5.3 Peroxisomal biogenesis disorders

Peroxisomal biogenesis disorders (PBDs) are a heterogeneous group of diseases affecting the formation of functional peroxisomes, clinically characterized by sensorineural hearing loss, pigmentary retinal degeneration, multiple organ dysfunction and psychomotor impairment. PBDs comprise two clinically distinct subtypes: the Zellweger syndrome spectrum (ZSS) disorders and rhizomelic chondrodysplasia punctata (RCDP) type 1 [113]. RCDP type 1 is clinically clearly distinct from the ZSS disorders and characterized by proximal shortening of the limbs (rhizomelia), multiple punctuate epiphyseal calcification (chondrodysplasia punctata), cataracts, facial dysmorphism, microcephaly, small stature, and psychomotor retardation [114]. The Zellweger syndrome spectrum (ZSS) consists of three overlapping clinical phenotypes: the cerebrohepatorenal syndrome or Zellweger syndrome

(ZS), neonatal adrenoleukodystrophy (NALD), and infantile Refsum disease (IRD). ZS classically presents with severe hypotonia and characteristic craniofacial features including a large anterior fontanel, a prominent forehead, shallow orbital ridges, epicanthal folds, a high arched palate, a broad nasal bridge and a small nose with anteverted nares. Ocular abnormalities such as cataracts, glaucoma and corneal clouding are common and in some cases patients show seizures, renal cysts and hepatic dysfunction, evident as neonatal jaundice and elevation in liver function tests. Infants with the most severe ZS presentation are most likely to die within the first year of life [115]. The clinical course of patients with the NALD and IRD presentation is variable and manifests in developmental delay, hypotonia, liver dysfunction, sensorineural hearing loss, retinal dystrophy and vision impairment. Children with NALD may reach their teens, while patients with the IRD presentation may reach adulthood [116].

The PBDs are autosomal recessive disorders and can be caused by a defect in any of the 14 different peroxin (*PEX)* genes described in humans. These *PEX* genes encode for proteins named peroxins that are involved in various stages of peroxisomal protein import and/or the biogenesis of peroxisomes [106] (Figure 1-4).. Mutations in PEX7 exclusively cause RCDP type 1 whereas mutations in the remaining 13 PEX genes manifest in ZSS.

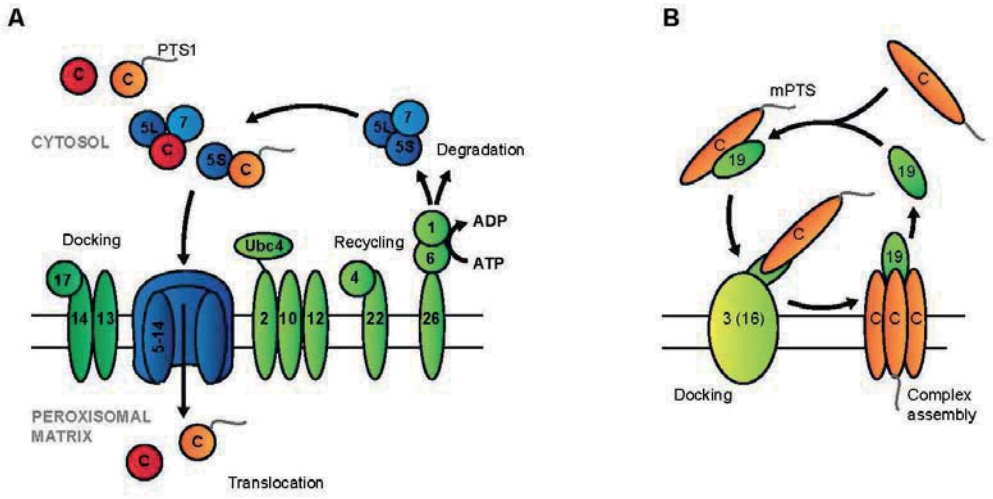

Figure 1-4 Import machinery for peroxisomal protein import. Schematic presentation of the human import machinery for peroxisomal matrix and membrane proteins indicating the different roles of the 13 different peroxins, the cargo protein is depicted as “C”. For detailed description see text.

The transport of proteins to the peroxisomal matrix or membrane is highly selective and mediated by specific import sequences known as peroxisomal targeting sequences (PTSs). Peroxisomal proteins destined for the matrix contain a C-terminal peroxisomal targeting

sequence PTS1 [117] or, with less frequency, an internal peroxisomal targeting sequence PTS2 [118] and are recognized by cytoplasmic PEX5 and PEX7, respectively (Figure 1-4A). PEX5 is expressed as a long (PEX5L) and a short (PEX5S) isoform. Both variants can bind PTS1 proteins and direct these to the peroxisomal membrane. In addition, PEX5L contains a PEX7-binding domain required for binding and shuttling of matrix protein-loaded PEX7 to the peroxisomal membrane [119]. After docking to PEX13 and PEX14, cargo proteins are translocated into the lumen and shuttling proteins are released from the membrane for another transportation cycle [120]. A similar but less characterized cycle has been proposed for the transport and membrane incorporation of peroxisomal membrane proteins (Figure 1-4B). Proteins destined for the peroxisomal membrane contain specific internal targeting sequences, recognized by the cytosolic shuttling protein PEX19 [121]. PEX3 is one of the earliest membrane proteins found in peroxisomal membranes. However, incorporation mechanism is independent of PEX19 [122].

Due to their distinct functions in peroxisomal import and biogenesis, mutations in *PEX* genes result in particular phenotypes. Mutations in the *PEX1, PEX2, PEX5, PEX6, PEX10, PEX12, PEX13, PEX14* and *PEX26* genes typically affect only the import of peroxisomal matrix proteins and cells of patients with aberrations in these genes usually contain peroxisomal membrane remnants. Due to the involvement of *PEX3, PEX16* and *PEX19* in the transport and incorporation of peroxisomal membrane proteins, mutations in these genes affect the import of both peroxisomal matrix and membrane proteins. Consequently, cells with defects in these genes are completely devoid of any peroxisomal structures.

1.5.4 Peroxisomes during viral infection

Due to the localization of MAVS in the peroxisomal membrane, the organelle is a platform for antiviral signaling, initiating an early and IFN-loop independent response via expression of ISGs. In addition, activation of peroxisomal MAVS signaling is accompanied by morphological changes of the organelle, leading to the aggregation of peroxisomes and the formation of peroxisomal tubules. Some viruses, such as vesicular stomatitis virus (VSV), interfere with the host cell’s induction of interferon via mitochondrial MAVS by viral proteins [123]. Consistent with this shut down of the mitochondrial interferon induction pathway, the remaining cellular antiviral response to VSV was found to be mediated mainly by peroxisomal MAVS [50].

Furthermore, a number of viruses exploit peroxisomes during infection. The Nef protein, expressed by human immunodeficiency virus (HIV), interacts with the peroxisomal acyl-CoA thioesterase 8 (ACOT8). Interestingly, this interaction results in down-regulation of CD4 in

HIV-infected cells [124] and enhanced enzymatic activity of ACOT8 [125]. However, the impact of this effect is yet unknown. The nonstructural influenza virus A protein 1 (NS1) binds to peroxisomal 17-b-hydroxysteroid dehydrogenase 4 (17b-HSD4), an enzyme involved in oxidation of cholesterol and long- chain branched fatty acids. This interaction potentially leads to inhibition of the enzyme, since overexpression of 17b-HSD4 results in reduced expression of influenza proteins, impaired viral assembly and budding [126]

1.6 Screening approaches to identify organelle-associated proteins with implication in RLR signaling

Two complementary but distinct approaches can be defined in proteomics. Firstly, expression proteomics that aims at describing the proteome, defined as the ensemble of all proteins expressed, and its dynamic changes upon perturbation, stimulation, or disease condition. A second approach represents interaction proteomics that focuses on mapping the protein-protein interaction (PPI) network by testing direct pair-wise interaction or by defining protein complex composition. In order to investigate RLR signaling, we used SILAC-based proteomics as an unbiased approach to study changes in the mitochondrial proteome. Furthermore, we performed BRET to investigate PPIs of MAVS with peroxisomal proteins.

1.6.1 Quantitative mass spectrometry via SILAC

A powerful method to analyze complex protein mixtures is bottom-up proteomics, also referred to as shotgun-proteomics. In this approach, proteins are further fractionized into peptides and analyzed by mass spectrometry. Peptides in comparison to proteins are easier to solubilize and separate, which allows better interpretation by mass spectrometry (MS). Identification of only few peptides is generally sufficient to unambiguously identify a protein. Shotgun proteomics does not focus on specific sites or proteins of interest and thus offers a hypothesis-free and proteome-wide analysis, well suited for screening approaches.

To systematically capture the transient and spatiotemporal regulated nature of cellular immune responses, direct comparison of different physiological states is required. Quantitative high-resolution proteomics, such as stable isotope labeling of amino acids in cell culture (SILAC) offers the tools to evaluate proteome compositions under changing conditions with great sensitivity and thereby allows the characterization of cellular processes in an unbiased manner [127].

SILAC relies on the metabolic incorporation of stable isotopes of amino acids (^{2}H instead of H, ^{13}C instead of ^{12}C, or ^{15}N instead of ^{14}N). Incorporation of the heavy amino acid into a

peptide leads to a mass shift compared to the peptide containing the light version of the amino acid. For labeling of cells, the essential amino acids arginine and lysine are chosen to ensure that cells have to incorporate the added, labeled amino acid into their proteome [128]. As shown in Figure 1-5, for a standard SILAC experiment two separate cell populations are cultured with either labeled or unlabeled amino acids. One of the populations can be subjected to a stimulus, whereas the other population remains untreated. The two populations are subsequently combined and processed simultaneously. The proteome of the sample is extracted and measured by MS/MS analysis. Since both populations are prepared simultaneously measurements of the peaks of corresponding peptides can be compared directly and abundances can be quantified via their peak intensities. If the SILAC peptide pair appears in a one-to-one ratio no difference in the abundance is seen in the proteomes. A higher peak intensity of the peptide which contains a heavy amino acid indicates a bigger abundance in the designated population [128]. A major advantage of this method is the possibility to label all peptides without the need of further chemical modifications. Therefore the method is relatively easy to apply as well as compatible with multistage purification procedures. However, a prerequisite for SILAC is that the cells of interest tolerate and proliferate in the special medium that usually contains dialyzed serum [129].

Unlike in shotgun proteomics with unlabeled peptides, SILAC allows mixing of two samples early in the proteomics workflow and thus makes the quantification independent of variations that may be introduced during sample preparation, *e.g.* cellular fractionation or LC-MS/MS analysis, ensuring considerably higher accuracy in measurements.

SILAC was only developed in recent years [130], but has already become a useful tool to study changes in protein abundances, modification patterns or protein-protein interactions in the context of immune signaling [131-135] and has additionally been applied in tumor biology [136, 137], virology [132, 138], apoptosis [139] and cytoskeleton dynamics [140]. It has also been proven to be a valuable method to study changes in subcellular localization of proteins [141-143].

1.6.2 Determination of protein-protein-interactions in living cells via BRET

Virtually every cellular function is dependent on signal transduction cascades. Activation and regulation of these processes rely on transient interactions between two or more proteins. The method of bioluminescence resonance energy transfer (BRET) allows the *in vivo* study of protein-protein interactions as well as the study of conformational changes within proteins or molecular complexes and is thus a powerful tool to study the molecular basis of signaling pathways. BRET relies on the non-radiative (dipole-dipole) transfer of energy from a light-

producing donor enzyme after substrate oxidation to a complementary acceptor fluorophore. Since the efficiency of resonance energy transfer is inversely proportional to the sixth power of the distance between donor and acceptor dipoles, any changes in the spatial orientation of donor and acceptor can be detected at high sensitivity [144].

In order to perform BRET experiments expression vectors with genetically encoded luciferase donor and fluorescent acceptor proteins, fused to two potential interaction partners, respectively, are transfected into cells. Energy transfer between donor to acceptor occurs only if the distance between the two is below 10 nm, thus a positive signal indicates that the proteins of interest are likely to be interacting with each other, either by direct interaction or as part of a complex. The resulting acceptor energy emission can be detected and, in proportion to the donor luminescence signal, relates to the BRET ratio. BRET can be measured using a luminometer (microplate or single-tube) or scanning spectrometer, with the capacity to sequentially or simultaneously detect filtered light of two distinct wavelengths [145].

The most common BRET techniques are based on Renilla luciferase (hRluc) in combination with coelenterazine as a substrate and VENUS, a derivate of the yellow fluorescent protein ($BRET^1$) or a DeepBlueC substrate in association with green fluorescent protein (GFP) ($BRET^2$). However, due to better quantum yields, the use of VENUS was found to provide better BRET signal detection [146], and was applied in our study. The BRET technology is most suited for studying protein-protein interactions in living cells where they are expressed in a near-physiological environment in the correct cellular compartment. However, due to its high distance dependency, variations in BRET ratios can occur in response to changes of donor to acceptor proportions or conformational changes of the interacting proteins. Taking this fact into consideration, BRET experiments for one protein pair are performed with tags either fused to the C-Terminus or the N-terminus, respectively. Additional evidence for interaction specificity is commonly provided using a BRET-based saturation assay. The BRET technology has been used successfully for a wide range of assay types including protein-protein interactions [147], functional assays on G-protein coupled receptors (GPCR) [148], and receptor oligomerization as well as protease activity assays in living cells [149]

.

1.6.3 Objectives and aims

Up to now, diseases caused by viral infections remain a challenging global health issue. Innate immunity is the first line of defense against these viral infections. A hallmark of antiviral innate immune responses is the production of type I IFN and pro-inflammatory cytokines. These molecules do not only rapidly contain viral infection by inhibiting viral replication and assembly but also play a crucial role in activating the adaptive immune system to eradicate the virus. RIG-I-like receptors (RLRs) are essential for the detection of cytoplasmic viral RNA of many human pathogenic viruses, such as hepatitis C virus, influenza A virus, norovirus or dengue virus. The adaptor protein MAVS coordinates the signals from activated RLRs and is crucial for the initiation of the antiviral signaling cascade. Due to its location in the outer mitochondrial membrane as well as in the membrane of peroxisomes studies focusing on MAVS hypothesized that the surfaces of mitochondria and peroxisomes act as signaling platforms for antiviral immune responses and postulated an intricate bi-directional interplay between mitochondrial and peroxisomal organelle-function and antiviral signaling. In the literature, many details of the interplay between organelle function and MAVS mediated signaling have already been elucidated [59, 60, 86, 88, 150, 151]. However, many aspects of the interplay between mitochondria, peroxisomes and antiviral signaling are still unknown or a matter of debate. The presented dissertation therefore focused on the following scientific questions:

a) Is it possible to identify and characterize new candidate proteins with implication in antiviral signaling using quantitative shotgun proteomic analyses of mitochondria after stimulation of RLR signaling?
b) Does RLR signaling influence mitochondrial respiration and the mitochondria-mediated production of reactive oxygen species?
c) Is it possible to identify peroxisomal protein interaction partners of MAVS, utilizing a BRET-based approach to screen a peroxisomal protein library?
d) Is it possible to elucidate the potential role of peroxisomes in RLR-mediated signaling, using a cell culture model deficient of functional peroxisomes?

2 Material and Methods

2.1 Material

2.1.1 Technical equipment

1-ml Luer Lock Gas-Tight Syringe	SGE Supelco (Bellefonte, USA)
Alpha Imager HP	Alpha Innotech (San Leandro, CA, USA)
Cell homogenizer	Isobiotech (Heidelberg, DE)
Cell incubator	Heraeus (Hanau, DE)
CELLview glass bottom dish	Greiner bio-one (Frickenhausen, DE)
Centrifuge 5415 R	Eppendorf (Hamburg, DE)
Centrifuge Sepatech Omnifuge	Heraeus (Hanau, DE)
FACS Calibur	BD Biosciences (Heidelberg, DE)
FluoroMax-P Fluorimeter	Horiba Jobin Yvon (Unterhaching, DE)
Freedom Evo 200 Workstation	Tecan (Männedorf, CH)
GE Ettan LC System	GE Healthcare (Munich, DE)
Ice machine	Ziegra (Isernhagen, DE)
Inolab benchtop pH meter 720	WTW (Darmstadt, DE)
Lamin Air Flow (HB 2448)	Heraeus (Hanau, DE)
LTQ-Orbitrap	Thermo Fischer Scientific (Schwerte, DE)
LUMIstar OPTIMA	BMG (Ortenberg, DE)
MidiMACS	Miltenyi Biotec (Bergisch Gladbach, DE)
Microscope	Zeiss (Jena, DE)
Multiplate Reader Mithras LB 940	Berthold Technologies (Bad Wildbach, DE)
NanoLC system	Agilent (Waldbronn, DE)
NanoPhotometer	Implen (Munich, DE)
Nucleofector 96-well Shuttle	Lonza Inc (Walkersville, USA)
Power Pac 200 voltage device	Biorad (München, DE)
Scale LP 6209	Sartorius (Göttingen, DE)
Scale SBC 21	Scaltec Instruments (Heiligenstadt, DE)
SF96 Analyzer	Seahorse Biosciences (North Billerica, USA)
Thermocycler T3	Biometra (Göttingen, DE)
Trans-Blot SD Semi-Dry Transfer Cell	Biorad (Munich, DE)
Shaking device	Janke & Kunkel (Staufen, DE)

2.1.2 Kits

Annexin V apoptosis detection kit	BD Biosciences (San Diego, CA, USA)

Cell Line Nucleofector Kit (100 RCT)	Lonza, (Cologne, Germany)
Human IL6 ELISA Set	BD Biosciences (San Diego, CA, USA)
Human IP-10 ELISA Set	BD Biosciences (San Diego, CA, USA)
JETQUICK Plasmid Spin Kit	Genomed (Löhne, DE)
MACS mitochondria isolation Kit	Miltenyi (Bergisch Gladbach, DE)
MegaShortscript T7 Kit	Fa. Ambion (Darmstadt, DE)
Mitochondria Stressor Kit	Seahorse Biosciences (Massachusetts, USA)

2.1.3 Chemicals

ELISA

Bovine serum albumin (BSA)	Roth (Karlsruhe, DE)
Polyoxyethylen(20)-Sorbitan-Monolaurat	Roth (Karlsruhe, DE)

SDS-Polyacrylamide gel electrophoresis and western blot

Ammoniumpersulfate (APS)	Sigma-Aldrich (Steinheim, DE)
Blotting paper	Schleicher & Schuell (Dassel, DE)
Bromphenol blue	Roth (Karlsruhe, DE)
Enhanced chemiluminescence detection system (ECL)	Amersham (Little Chalfont, GB)
Ethylenediaminetetraacetic acid (EDTA)	Roth (Karlsruhe, DE)
Glycine	Roth (Karlsruhe, DE)
Methanol	Merck (Darmstadt, DE)
β-Mercaptoethanol	Biorad (München, DE)
Milk powder	Roth (Karlsruhe, DE)
Sodium chloride	Roth (Karlsruhe, DE)
Sodium dodecyl sulfate	Roth (Karlsruhe, DE)
Nitrocellulose membrane	Amersham (Little Chalfont, GB)
Prestained protein molecular weight marker plus	Fermentas (St. Leon-Roth, DE)
Rotiphoresis Gel 30 (37,5:1)	Roth (Karlsruhe, DE)
Tetramethylethylendiamine (TEMED)	Roth (Karlsruhe, DE)
Tris hydroxymethylaminomethan (TRIS)	Roth (Karlsruhe, DE)
TRIS hydrochloride	Roth (Karlsruhe, DE)

Transfection reagents	
Genejuice	Merck Chemicals (Darmstadt, DE)
Lipofectamine 2000	Invitrogen (Carlsbad, CA, USA)
Lipofectamine RNAiMax	Invitrogen (Carlsbad, CA, USA)

DNA gel electrophoresis	
Agarose	Sigma-Aldrich (Steinheim, DE)
Ethidium bromide	Sigma-Aldrich (Steinheim, DE)
Formamide	Sigma-Aldrich (Steinheim, DE)
GeneRuler DNA Ladder Mix	Fermentas (St. Leon-Roth, DE)
Urea	Roth (Karlsruhe, DE)
Rotiphoresis gel 40	Roth (Karlsruhe, DE)
Tris-Borat-EDTA (TBE)	Sigma-Aldrich (Steinheim, DE)

Cell culture	
SILAC amino acids	Pierce Bioscience (Bonn, DE)
Aqua ad injectabilia	Braun (Melsungen, DE)
Calcium chloride	Sigma-Aldrich (Steinheim, DE)
Ciprofloxacin	Stada (Bad Homburg, DE)
Dulbecco's Modified Eagle Medium (DMEM)	Sigma-Aldrich (Steinheim, DE)
Dulbecco's Modified Eagle Medium (DMEM), no phenol red	Sigma-Aldrich (Steinheim, DE)
Dulbecco's Modified Eagle Medium (DMEM), suitable for SILAC	Sigma-Aldrich (Steinheim, DE)
Fetal calf serum	GibcoBRL (Paisley, GB)
Fetal calf serum, dialyzed	GibcoBRL (Paisley, GB)
Hoechst 33342 fluorescent stain	Pierce Bioscience (Bonn, DE)
L-Glutamine	PAA (Linz, A)
MCDB 153	Sigma-Aldrich (Steinheim, DE)
Opti-MEM	Invitrogen (Carlsbad, CA, USA)
Phosphate-buffered saline (PBS)	PAA (Linz, A)
Streptomycin	PAA (Linz, A)

Trypan blue	Sigma-Aldrich (Steinheim, DE)
XF assay medium	Seahorse Bioscience (North Billerica, USA)

Cell lysis

Glycerol	Roth (Karlsruhe, DE)
Nonidet P-40	Fluka Biochemika (Buchs, CH)
Phenylmethylsulfonylfluoride (PMSF)	Fluka Biochemika (Buchs, CH)
Protease inhibitor cocktail for mammalian cells	Sigma-Aldrich (Steinheim, DE)
Sodium orthovanadate	Sigma-Aldrich (Steinheim, DE)

TLR-agonists and cytokines

CpG	Invivogen (San Diego, USA)
dAdT	Invivogen (San Diego, USA)
IFN-ß	Sigma-Aldrich (Steinheim, DE)
Poly (I:C) , HMW	Invivogen (San Diego, USA)

Enzymes

Calf intestine alkaline phosphatase, CIAP	Fermentas (St. Leon-Roth, DE)
Desoxyribonucleotide	Fermentas (St. Leon-Roth, DE)
Lys C	Promega (Münster, DE)
Pfu-polymerase	Fermentas (St. Leon-Roth, DE)
RNase-inhibitor	Fermentas (St. Leon-Roth, DE)
Trypsin, sequencing grade	Roche (Mannheim, DE)

2.1.4 Antibodies

alexa fluor 488 goat anti mouse	Mol.Probe (Darmstadt, DE)
alexa fluor 488 goat anti rabbit	Mol.Probe (Darmstadt, DE)
alexa fluor 568 goat anti mouse	Mol.Probe (Darmstadt, DE)
alexa fluor 568 goat anti rabbit	Mol.Probe (Darmstadt, DE)
Ms mAb- anti-ß-Actin, HRP-linked	Santa Cruz (Santa Cruz, USA)
Rat mAb-anti-MAVS	Dr. Elisabeth Kremmer (Helmholtz Zentrum München, DE)

Rb pAb- anti-COXIV	Abcam (Cambridge, UK)
Rb pAb- anti-HSP60	Santa Cruz (Santa Cruz, USA)
Rb pAb-anti-Cytochrome C	Cell Signaling (Detroit, USA)
Rb pAb-anti-TOM40 (H-300)	Santa Cruz (Santa Cruz, USA)

2.1.5 Viral strains

Infection assays were performed with Sendai virus (SeV) cantell strain, obtained from Charles River Laboratories, and vesicular stomatitis virus (VSV) Indiana strain, generously provided by Prof. Dr. Anne Krug (LMU München).

2.1.6 Cell lines

The human melanoma cell line 1205Lu cell line [152] was used for the investigation of changes in the mitochondrial proteome and mitochondrial respiration rates upon stimulation of RLR signaling. The cells were kindly provided by Dr. Robert Besch (LMU München).

Human fibroblasts extracted from patients with Zellweger syndrome were generously provided by Prof. Ania Muntau (LMU München). The PEX3-deficient cell line was described by Muntau et al. [153].

2.1.7 Software

Adobe Creative Suite	Adobe Systems (San Jose,USA)
FlowJo Tree Star	FlowJo (Ashland, USA)
GraphPad	GraphPad Software Inc. (California, USA)
Microsoft Office	Microsoft (Redmont, USA)
MaxQuant	Max Planck Institute (Munich, DE)
Perseus	Max Planck Institute (Munich, DE)

2.2 Molecular biology methods

2.2.1 Polymerase chain reaction

Polymerase chain reaction (PCR) is a method to amplify a defined part of an extracted DNA sample. To define this part, two specific primers are needed that flank the region of interest, one upstream and one downstream primer. The general range of a primer is 15-30 bases, and the guanosine and cytosine amount should be 40-60%. The maximum size of the DNA fragment, which can be amplified with a standard PCR, is 10.000 bases. A PCR consists of several cycles. After each cycle the amount of amplified DNA is doubled.
The PCR method was used for the amplification of specific cDNA fragments. The polymerase PfuUltra (Fermentas) was used to prevent mutations. This enzyme has a 3' to 5' exonuclease activity and thereby provides a higher fidelity than normal polymerases.

The composition of a standard PCR 50 µl reaction mix is shown below:

PCR	
As required	DNA (100 pg to 500 pg)
5 µl	10x PfuUltra II Reaction Buffer
1 µl	dNTP mix 10 mM
1 µl	upstream primer 10 µM
1 µl	downstream primer 10 µM
1.25 U/50µl	PfuUltra DNA polymerase
As required	Nuclease-free H_2O

Standard PCR cycling conditions:

Function	**Duration**	**Temperature**	
Initial DNA denaturation	5 min	95°C	
DNA denaturation	20 sec	95°C	30 cycles
Primer annealing	20 sec	65°C	
Primer extension	15 s	72°C	
Final extension	3 min	72°C	
End	∞	4°C	

2.2.2 Gel electrophoresis

DNA fragments were separated in a length-dependent manner by gel electrophoresis. For separation, a 1-2% agarose gel (1-2% agarose in 100ml 1x TAE) was used. After boiling the

agarose was cooled down, 0.003% ethidium bromide was added, and the gel was poured. While cooling down, the gel forms a crosslinked polymer allowing the separation of DNA fragments according to their size. The DNA samples were supplemented with 1x DNA loading dye and loaded onto the gel. Due to the negative charge of DNA, molecules move from the negative pole to the positive pole when an electric field is applied. The DNA fragments of different sizes are separated at 100 V for 30 min. For size determination a 1 kb DNA Ladder (Fermentas - GeneRuler™) was used.

2.2.3 Purification of PCR products via gel extraction

The JETQuick Gel Extraction Kit was used to re-isolate double-stranded DNA fragments out of gel-slices after separation and purification of PCR samples by gel electrophoresis. The kit purifies DNA fragments of a length from 40 bp up to 20 kb. The DNA adsorbs to the silica-membrane of the JETQuick spin column in high-salt buffer while contaminants pass through the column. JETQuick gel extraction was done according to manufacturer`s protocol.

2.2.4 Digestion of DNA with restriction enzymes

For analytical purposes 0.2-2 µg of DNA were digested with 1 U of one or two restriction endonucleases in an appropriate 1× buffer. Restriction digests were carried out for 1 hour at 37°C. After digestion samples were separated by gel electrophoresis and extracted via gel extraction kit or directly purified by JETQuick PCR Purification Kit. DNA amounts were determined by photometric measurement.

2.2.5 Isolation of plasmid DNA

For plasmid DNA purification bacteria were grown on LB-plates, containing antibiotics for selection, and isolated clones were picked and cultivated in 2 ml LB-medium under antibiotic selection for 16 h at 37°C. Bacteria were harvested by centrifugation at 12,000 g for 2 minutes and plasmid DNA purification was performed with the GenJET™ Plasmid Miniprep Kit according to the manufacturer’s protocol.

2.2.6 RNA purification

Total RNA was isolated from 1 x 10^5 - 2 x 10^6 cells using the RNeasy Mini Kit (Qiagen) according to the manufacturer’s protocol.

2.2.7 cDNA synthesis

First-strand cDNA was generated from 1 µg of total RNA using Oligo(dT) primer and murine leukemia virus reverse transcriptase.
The following reagents were subsequently added and the reaction mix was incubated at 42°C for 60min, then at 70°C for 10min.

The composition of a standard 20 µl reaction mix is shown below:

PCR	
4 µl	5x reverse transcriptase buffer
0.5 µl	RiboLock RNase Inhibitor
2 µl	dNTP mix 10 mM
2 µl	RevertAid H Minus Reverse Transcriptase 10000U
	Nuclease-free H_2O

Standard conditions for reverse transcription:

Function	**Duration**	**Temperature**
Reverse transcription	60 min	42°C
Enzyme inactivation	10 min	70°C
End	∞	4°C

2.2.8 Quantitative real-time polymerase chain reaction

Quantitative real-time polymerase chain reaction (qRT-PCR) was used to quantify the relative amount of specific mRNAs in samples. Relative gene expression of each gene was calculated as the ratio of gene of interest mRNA and hypoxanthine phosphoribosyltransferase (HPRT) mRNA, both determined in the same sample. qRT-PCR was performed with the LightCycler 480 instrument. For specific primers and probes see 8.2.

For all runs the standard Roche protocol for mono color hydrolysis probes with 45 amplification cycles was used according to the following protocol:

Volume	Reagent
1 µl	cDNA
5 µl	2x Kappa Probe Fast mastermix
0.2 µl	upstream primer (100 µM)
0.2 µl	downstream primer (100 µM)
0.1 µl	fluorescent hydrolysis probe
3.5 µl	nuclease-free H_2O

2.2.9 Molecular cloning

Molecular cloning is a technique to integrate selected DNA sequences into a vector for amplification in bacteria. In order to get the vector and the integrated sequence amplified, the cloning vector must carry an origin of replication. Additionally, one or more prokaryotic antibiotic resistance genes are needed for selection. Molecular cloning was carried out using the Gateway recombination system [154], which is based on the site-specific recombination system found to be used by phage λ to integrate its DNA in the *E. coli* chromosome. Both organisms have specific recombination sites called *att*P in phage λ site and *att*B in *E. coli*. The integration process is catalyzed by 2 enzymes: the phage λ encoded protein Int (integrase) and the *E. coli* protein IHF (integration host factor). Upon integration, the recombination between *att*B and *att*P sites (BP reaction) generate *att*L and *att*R sites that flank the integrated DNA fragment. The process is reversible and the excision is again catalyzed by Int and IHF in combination with the protein Xis. The *att*L and *att*R sites surrounding the inserted DNA recombine specifically during the excision event to reform *att*P and *att*B sites (LR reaction) (Figure 2-1). The method is advantageous to transfer DNA sequences back and forth between a common intermediate clone (the entry clone) and a variety of different destination vectors.

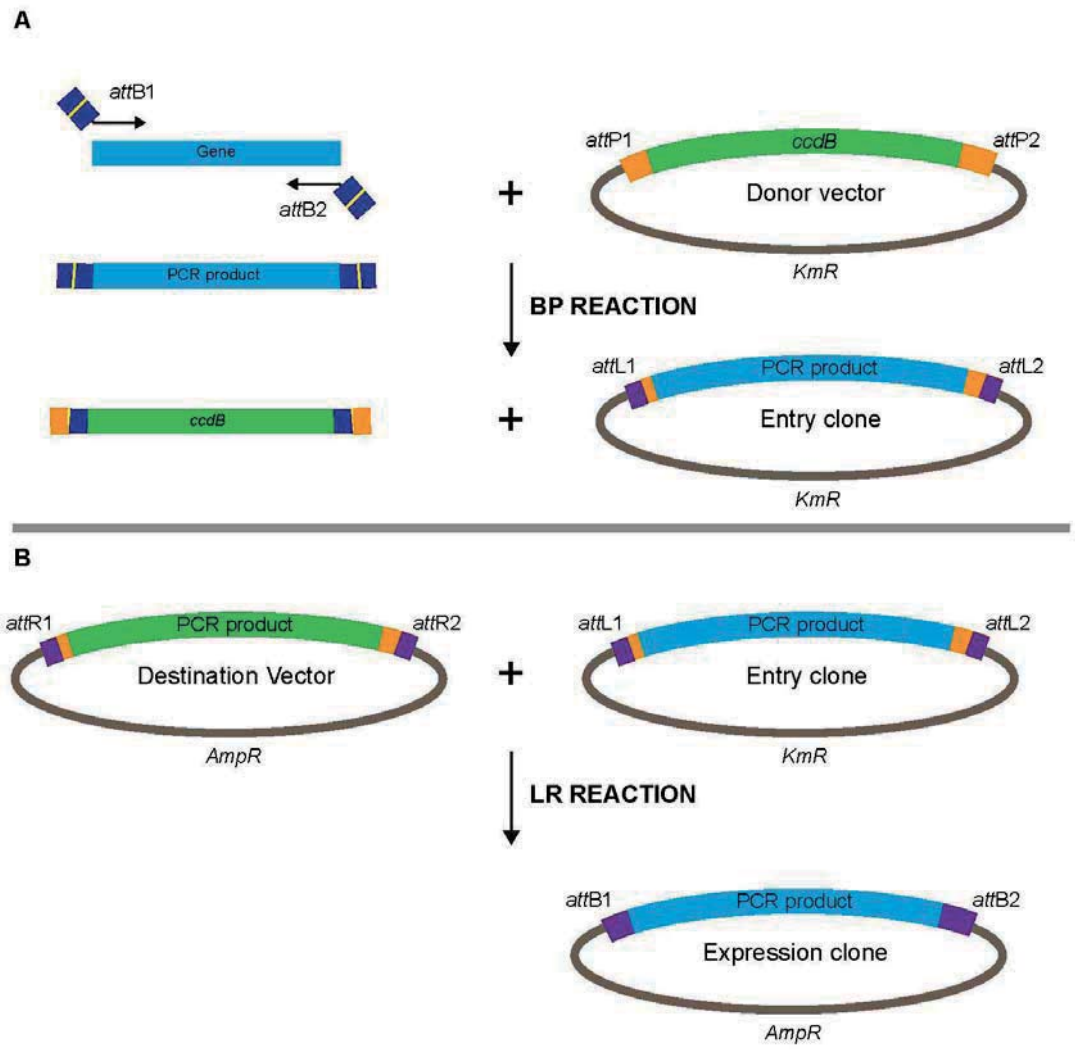

Figure 2-1 General Gateway cloning scheme. This diagram presents a schematic representation of the standard Gateway reactions, identifying the different plasmid types found in the BP (A) and LR reactions (B) along with the relevant selection markers.

For the cloning process *attB* sequences were attached to the sequence of interest via PCR amplification using PCR primers with incorporated attB sequences. In order to generate the entry clones, 50fmol of the PCR product was combined with 150 ng of the donor vector (pDONR™), containing *attP* sites and Gateway clonase enzyme. After incubation at 25°C for 18h, 2 µg of proteinase K was added to inactivate the BP-clonase and incubated for 15 min at 37°C. The entry clone was amplified by transformation into chemically competent *E.coli* Dh5α using kanamycine as a selection marker and the integration of the PCR product was confirmed by DNA sequencing through an external provider (Eurofins Genomics).

In order to produce expression vectors, 100 ng of the entry clone was combined with 150 ng of the destination vector (pENTR™) and 2 µl of LR-clonase. The reaction was incubated for 18 h at 25°C and the recombination reaction was stopped with 2 µg proteinase K for 15 min

at 37°C. The entry clone was amplified by transformation into chemically competent *E.coli* Dh5α using ampicillin as a selection marker and the correct size of the expression vectors were analyzed by restriction enzyme digestion.

BP reaction

pDONR™ (150 ng/µl)	1 µl	
PCR product (50 fmol *)	X µl	25°C/ 18h
H_20	2µl	
BP clonase	1 µl	
Proteinase K	2 µl	37°C/ 15 min

LR reaction

pENTR™ (150 ng/µl)	1 µl	
Entry clone (100ng)	X µl	25°C/ 18 h
H_20	2µl	
LR clonase	1 µl	
Proteinase K	2 µl	37°C/ 15 min

2.3 Biochemical methods

2.3.1 SDS-polyacrylamide gel electrophoresis (PAGE) analysis

Separation of proteins by sodium dodecyl sulfate polyacrylamide gel electrophoresis (SDS-PAGE) was performed using 10 % separation and a 5 % stacking gels and 1x running buffer. For denaturation, the protein samples were diluted in the appropriate volume of 6x Laemmli sample buffer and heated to 95°C for 5 min. Electrophoresis was performed setting the power supply to 30 mA per gel with SDS-PAGE running buffer. The run was stopped when the dye front was 2 to 3 mm away from the bottom edge of the gel. The PageRuler “Prestained Protein Ladder” (Invitrogen) was used as a marker for protein sizes.

Buffer	Composition
4x Separation buffer	3 M Tris (pH 8.5), 0.4% SDS
4x Stacking buffer	0.5 M Tris (pH 6.8), 0.4% SDS
10% Separation gel	2.5 ml H_20, 2.5 ml separation buffer, 5 ml acrylamide, 50 µl 10% APS, 5 µl TEMED
5% Stacking gel	2.5 ml H_20, 1 ml separation buffer, 500 µl acrylamide, 40 µl 10% APS, 4 µl TEMED
1x Running buffer	3.02 g Tris, 14.4 g glycine, 1 g SDS in 1l ddH_20

2.3.2 Western blot analysis

After electrophoresis, proteins were transferred from the gel to a PVDF membrane, pore size 0.45 µm, using a wet blotting system and western blot transfer buffer. The wet transfer was performed setting the power supply to a voltage of 100 volt for 50 min.

After plotting the membranes were washed in TBS-T buffer and blocked for 1 h at room temperature in blocking buffer. Subsequently the membranes were incubated for 2 h with the primary antibody, washed again and incubated with a HRP-conjugated secondary antibody for 1 h at room temperature. Membranes were washed 3 times for 10 min after incubation with each antibody. The HRP-reaction was visualized using the ECL-Plus chemiluminescence kit (Amersham BioScience) and the alpha imager HP-system.

Buffer	Composition
TBS-T	10 mM Tris/base pH 7.5, 0.1 M NaCl, 100 mM gylcine, 1 mM EDTA, 0.1% Tween 20
Western blot transfer buffer	10 mM Tris (pH 6.8), 0.4% SDS, 100 mM gylcine
Blocking buffer	TBS-T, 5% fat free dry milk
Antibody buffer	TBS-T, 5% BSA, 0.05% NaN_3

2.4 Immunological methods

2.4.1 Virus infection assay

Cell lines were plated in 48-well plates at a density of 5 x 10^4 cells per well and incubated over night. The next day the serum-containing medium was removed and the cells were infected with vesicular stomatitis virus (VSV) in serum-free medium at a multiplicity of infection (MOI) of 0.5 or Sendai virus at 40 U per ml diluted in Opti-MEM. After 1 h of incubation, extracellular virus was removed by washing with PBS and serum-containing DMEM medium. Cells were harvested at the given time points after the infection.

2.4.2 $TCID_{50}$ assay (tissue culture infectious dose 50%)

This endpoint dilution assay is performed to quantify the unknown amount of infectious virus particles in a sample by comparison with a virus stock of known concentration. This assay is only possible for viruses that cause cytopathic effects (CPE) in the cell line used to perform the assay and defines to which degree the virus containing sample needs to be diluted to cause 50% of all cells in the assay to die.

For the quantification of the $TCID_{50}$ for VSV, 1x10^4 1205Lu cells were seeded into a 96-well plate to adhere over night. After adherence, a wild-type VSV stock solution with a starting concentration of 10^7 MOI/ml was diluted 1:10 in 150µl Opti-MEM in a separate plate with 96-well format. Cells were washed in 100 µl PBS per well and 100µl of virus dilutions were transferred onto the cell-containing 96-well plate. After 1 h of incubation, cells were washed in 100 µl PBS per well and 100 µl of culture medium was added. The samples were incubated at 37°C and monitored daily for CPE by microscopy over a period of one week. Wells containing living and dead cells were recorded and $TCID_{50}$ values were calculated using a Reed-Muench calculator [155].

2.4.3 Enzyme-linked immunosorbent assay (ELISA)

To measure the amount of IP10 and IL6 in the supernatant of cells, a ”sandwich” ELISA for IP10 and IL6 (BD Biosciences ,San Diego, CA, USA) was performed according to the manufacturer’s protocol.

2.4.4 Detection of apoptosis and cell death by flow cytometry using staining with annexin V and propidium iodide

Propidium iodide (PI) can be used in conjunction with annexin V to determine if cells are viable, apoptotic, or necrotic through differences in plasma membrane integrity and permeability. In viable cells, phosphatidylserine (PS) is located on the cytoplasmic surface of the cell membrane. However, in the early stages of apoptosis, PS is flipped from the inner to the outer leaflet of the membrane, exposing PS to the external cellular environment where it can be detected. Staining with fluorescein isothiocyanate (FITC) conjugated to annexin V, a calcium-dependent phospholipid-binding protein, provides a quick and reliable detection assay for studying the externalization of phosphatidylserine. Additionally, in late apoptotic and necrotic cells, the integrity of the plasma and nuclear membranes decreases, allowing PI to pass through the membranes, intercalate into nucleic acids, resulting in a red fluorescent signal [156].

For annexin-FITC and PI staining, cells were harvested and washed once in PBS and once in 1x binding buffer, respectively. The cells were resuspended in 1x binding buffer at a concentration of $5x10^6$ cells per ml. 5 µl of annexin V were added per 100 µl cell suspension and incubated for 30 min on ice protected from light. The cells were washed in 1x binding buffer and resuspended in 200 µl 1x binding buffer. 1 µl of propidium iodide was added per sample and cells were analyzed by flow cytometry.

2.5 Cell culture and cell fractionation

2.5.1 General cell culture conditions

All cell lines were cultivated at 37°C, 95% humidity and with a supplementation of 5% CO_2. All experiments were performed under sterile conditions. When cells reached a confluency of approximately 80%, the medium was removed and cells were washed with PBS. Cells were detached by trypsin supplemented with 0.5% EDTA and diluted to the desired concentration in complete growth medium. For experimental procedures, cells were counted with a Neubauer hemocytometer. The viability of cells was determined using trypan blue, a dye selectively staining dead cells. In viable cells this stain is excluded, due to an intact membrane potential in these cells.

2.5.2 Transfection of cells with siRNA and expression plasmids

For knockdown experiments via *small-interfering* RNA (siRNA), $5x10^4$ cells were cultivated in 24-well-plates in 200 µl DMEM. Per well 10 pmol of siRNA and 1 µl Lipofectamine RNAiMax were diluted in 25 µl Opti-MEM each, and incubated separately for 5 min. The reagents were then mixed and incubated for another 20 min before they were transferred to the supernatant of the cells. siRNAs were transfected twice in a 24 h interval and knock-down efficiencies were controlled 24 h after the second transfection.

For over-expression assays 5×10^4 cells were cultivated over night in 24-well-plates in 200 µl DMEM. Per well 100 ng plasmid DNA and 0.5 µl gene juice transfection reagent were diluted in 50 µl Opti-MEM. After 20 min the complex of DNA and transfection reagent was added directly to the supernatant of cultured cells. Plasmids encoded GFP-fusion proteins which allowed verification of transfection efficiency 24 hours post transfection via immuno-fluorescence.

2.5.3 Purification and subfractionation of mitochondria

For the isolation of mitochondria, a cell homogenizer (Isobiotec, Germany) was combined with 1-ml Luer Lock Gas-Tight syringes to mechanically rupture the cell membranes. The homogenizer was pre-cooled on ice to ensure cooling of the samples during the isolation. Before the isolation start, a 10 mm tungsten carbide ball was inserted and the homogenizer was equilibrated with isolation buffer (PBS supplemented with protease inhibitor cocktail for mammalian cell (Sigma-Aldrich)). 5×10^6 1205Lu cells were resuspended in 1 ml of isolation buffer and passed three times through the system. To recover the whole homogenate, the system was rinsed once with 1 ml of isolation buffer. The pooled homogenate was cleared from cell debris and nuclei by centrifugation (800×*g*, 5 min at 4 C) and the supernatant was collected to further purify mitochondria.

2.5.3.1 Mitochondria purification via differential centrifugation

To obtain a crude mitochondrial fraction the cleared homogenate was centrifuged at 9000×*g* (10 min at 4 C) and the mitochondria-containing pellet was resuspended in 50 µl of isolation buffer.

2.5.3.2 Mitochondria purification via magnetic cell sorting

The Mitochondria Isolation Kit (Miltenyi Biotech) was used to isolate intact mitochondria from 1205Lu cells. This kit is based on the MACS (Magnetic Cell Separation) technology to isolate mitochondria from human cell lines and tissue. Two homogenates of $5x10^6$ cells were prepared according to the protocol described in 2.5.3. The cell lysate was incubated with a monoclonal anti-TOM22 antibody covalently coupled to magnetic MicroBeads for 1 h under shaking conditions in separation buffer according to manufacturer's protocol. This antibody specifically binds to the translocase of outer mitochondria membrane 22 (TOM22) of human mitochondria. The labeled cell lysate was loaded onto a midi-MACS column and placed in the magnetic field of a MACS separator. Labeled mitochondria were retained in the column, whereas unlabeled cell components were washed out as the column emptied by gravity. After removing the column from the magnetic field, the magnetically retained mitochondria were eluted with 1 ml separation buffer. The eluate was centrifuged at 13.000 x *g* and washed twice in 100 µl PBS. At the end the mitochondria-containing pellet was resuspended in 50 µl PBS. All steps were carried out at 4°C, buffers and solutions were kept on ice.

2.5.3.3 Isolation of the outer mitochondrial membrane

Mitochondria isolated from 8 x 10^7 1205LU cells via MACS according to the protocol described in 2.5.3.2 were pooled in 1ml PBS. After centrifugation (9000 *g*; 10 min; 4°C) the mitochondrial fraction was resuspended in 1 ml hypotonic buffer (20mM KPO_4 supplemented with 0,2% BSA), causing swelling of the organelles and rupture of the outer mitochondrial membrane. After incubation on ice for 20 min, 2 M sucrose in 20 mM KPO_4 was added to a final concentration of 0.75 M sucrose to achieve hypertonic conditions. The sample was incubated for additional 10 min. Ruptured Mitochondria were subsequently pelleted by centrifugation (16,000 *g*; 30 min; 4°C). After resuspension in 1 ml hypotonic buffer, the outer membrane was separated from mitoplasts by dounce homogenization. The sample was incubated with a monoclonal anti-TOM22 antibody covalently coupled to magnetic MicroBeads for 1 h under shaking conditions in 10 ml separation buffer (Mitochondria Isolation Kit (Miltenyi Biotech). The labeled mitochondrial fraction was loaded onto a midi-MACS column and placed in the magnetic field of a MACS separator to recover the crude outer membrane. Antibody-labeled outer mitochondrial membrane was retained in the column, whereas unlabeled components were washed out as the column emptied by gravity. After removing the column from the magnetic field, the magnetically retained outer mitochondrial membrane was eluted in 1 ml separation buffer The eluate was centrifuged at

13.000 x *g* and washed twice in 100 µl PBS and the pellet was subsequently resuspended in 50 µl PBS. All steps were carried out at 4°C, buffers and solutions were kept on ice.

2.5.3.4 Proteolytic digestion of mitochondrial surface proteins

Mitochondria isolated from $1x10^7$ 1205LU by MACS separation as described above were washed three times in PBS and resuspended in buffer A (20mM Hepes, 100 mM NaCl, 2 mM $MgCl_2$ – pH7.4). The protein concentration of the sample was determined by Bradford assay. 20 µg Trypsin per 1 mg mitochondrial protein was added and incubated for 15 min on ice. Reaction was stopped with 1 mM PMSF (5 min, on ice). The sample was centrifuged at 13.000 x *g* for 10 min to separate digested peptides from the remaining organelle. After centrifugation, the peptide-containing supernatant was collected ant immediately stored at -80°C. The mitochondrial pellet was washed twice in 100 µl PBS supplemented with protease inhibitor cocktail (Sigma Aldrich) and was resuspended in 50 µl PBS for western blot analysis.

2.5.4 Immunofluorescence imaging by confocal microscopy

For immunofluorescence imaging 5 x 10^4 1205Lu cells were cultivated on 12 µm glass cover slips and fixed with 4% paraformaldehyde for 15 min at 37°C. Samples were carefully washed three times in PBS and permeabilization was performed using 0.2% Triton-X-100 for 10 min at RT. Subsequently, samples were treated with blocking buffer (2% BSA in PBS-T) for 1 h at RT. The samples were incubated with the primary antibody (1 µg/ml dilution in blocking buffer). After 3 washing steps in PBS-T (10 min; RT), the samples were incubated in fluorescently-labeled secondary antibody (1 µg/ml dilution in blocking buffer). To stain DNA, samples were incubated with the DNA binding dye Hoechst 33342 (5 µM*)* or DAPI (3 µM*)*, respectively, for 1 min at RT.

For life cell imaging, 5 x 10^4 HEK cells or 1205Lu cells, respectively, were seeded into a CELLview glass bottom 4-compartment dish (Greiner bio-one) for adhesion over night. HEK cells were transfected with a VENUS-containing plasmid according to the protocol described in 2.5.2 and analyzed 12-24 h post-transfection. 1205Lu cells were infected with transgenic, GFP-bearing, VSVwt or VSV-M51R according to the protocol described in 2.4.1 and analyzed 8 h post infection. To stain DNA, samples were incubated with the DNA binding dye Hoechst 33342 (5 µM*)* or DAPI (3 µM*)*, respectively, for 1 min at RT.

Results were imaged using a Leica TCS SP5 confocal microscope. If not otherwise indicated, all steps were carried out at room temperature

2.5.5 Visualization of mitochondria via MitoTracker CMXRos staining

In order to stain mitochondria, the cells were washed in PBS and incubated with 100nM MitoTracker CMXRos (Molecular Probes) in pre-warmed DMEM for 30 min at 37°C. Prior to fixation, the cells were washed twice in PBS. Mitochondrial distribution was assessed by confocal microscopy as described in 2.5.4.

2.5.6 Quantification of mitochondrial ROS via MitoSOX^{TM} Red

MitoSOX™ Red (Thermo Fisher scientific) permeates live cells and selectively targets mitochondria where it is oxidized by superoxide but not by other reactive oxygen species (ROS) and reactive nitrogen species (RNS). The oxidized product is in turn highly fluorescent upon binding to nucleic acid. Due to its high selectivity for mitochondrial ROS, the dye is suitable for visualization and quantification of intracellular mROS levels.

1205Lu cells were seeded into a 24 well plate or glass bottom dish, respectively, at a density of 10^5 cells per well and incubated over night for attachment. MitoSOX™ Red was added to a final concentration of 5 µM according to the manufacturer's recommendation and incubated for 30 min to allow entrance of the dye into the cell. Subsequently, cells were washed twice with PBS and prepared for analysis. For confocal microscopy, cells in glass bottom dishes were treated with Hoechst33342 (5 µM) to stain nuclear DNA and analyzed using a Leica TCS SP5 confocal microscope. MitoSOX™ Red staining was captured at a wave length of 580 nm. For FACS analysis, cells were treated with poly (I:C), 3pRNA and CO4 for 6 h and 48 h, respectively. As a positive control, cells were treated with 100 µM antimycin A for 6 h. Subsequently, cells were transferred to FACS tubes and washed three times in 1 ml PBS. For the determination of mitochondrial superoxide by flow cytometry, the measurements were carried out using FAScalibur (BD Bioscience). MitoSOX Red was excited by laser at 488 nm in the FL2 channel.

2.6 Stable isotope labeling of amino acids in cell culture

1205Lu cells were cultured in SILAC-DMEM medium supplemented with ciprofloxacin, L-glutamine, dialyzed FCS and the light or heavy isotopes of lysine and arginine (Pierce Bioscience, Bonn, DE), respectively. Arginine was supplemented at concentrations of 48 µg/ml and 42 µg/ml, respectively. Lysine was supplemented at 146 µg/ml. Cells were allowed to incorporate the labeled amino acids for six passages and lysates from labeled cells were prepared, trypsin digested and analyzed by LC-MS to determine the incorporation efficiency of the isotopes. Raw files were processed using MaxQuant [157].

2.6.1 SILAC sample preparation

Cells of the 1205Lu line were cultivated in light and heavy medium and one part of the population was stimulated with 1 µg/ml poly (I:C) for the indicated period of time. After stimulation the cells were harvested by trypsinization and washed twice in PBS. The cell number was determined with a Neubauer counting chamber and mitochondrial fractions were prepared according to the protocol described in 2.5.3.2. The protein concentration in mitochondrial fractions was determined by Bradford assay. Based on their protein concentration, samples derived from cells cultivated with light derivates of amino acids were pooled in a 1:1 ratio with samples derived from cells cultivated with heavy derivates of amino acids. Pooled mitochondrial samples were centrifuged at 13.000 x g and washed twice in 100 µl PBS supplemented with a protease inhibitor cocktail (Sigma Aldrich). After washing, samples were resuspended in 50 µl PBS. Optionally, the outer mitochondrial membrane and surface proteins were extracted from pooled mitochondrial samples as described in 2.5.3.3 and 2.5.3.4, respectively. 20 µg of each sample was retained for western blot analysis before subsequent preparation for mass spectrometry analysis.

2.6.2 Sample preparation for mass spectrometry

The generic workflow of shotgun proteomics starts with the extraction of proteins from the biological sample. Proteins are degraded into peptides by site-specific endoproteases (*e.g.* trypsin and lys-C) cleaned, desalted and concentrated. To efficiently resolve and identify peptides contained in complex mixtures, a combination of ultrahigh-pressure liquid chromatography (UHPLC) and high-resolution mass spectrometry with very high sequencing speed have proven most successful. During the MS scan, mass to charge (m/z) ratio and relative intensities of co-eluting peptides are detected. In order to gain sequence information, peptides are subsequently collected and fragmented and m/z ratios and intensities of ionized fragments are collected (MS/MS). These MS/MS scans employ two stages of mass analysis in order to analyze the fragmentation of a specific ion in a complex mixture of ions. This information is matched to in-silico peptide and protein databases to assign the corresponding amino acid sequences to each peptide. Software tools, such as MaxQuant [157], enable automated mapping of peptides and matching to corresponding proteins [129].

Samples, prepared as described in 2.5.3, were subsequently denatured in 6 M Urea / 2 M thiourea (U/T) in 10 mM HEPES (pH 8.0) and sonicated for 10 min in an ultrasonication bath on ice. Lysates were centrifuged for 15 min (14,000 rcf/ RT) and supernatants were

transferred into a clean eppendorf tube. Protein concentration was determined by the Bradford assay (OD595). 100 µl reduction buffer was added to the sample and incubated for 30 min at RT. Alkylation was performed by addition of 55 mM iodoacetamide and incubation for 20 min at RT in the dark. Samples were subsequently digested with Lys C (1 µg LysC solution/50 µg protein solution) for at least 3h at RT. Samples were diluted 1:5 with 50 mM ammoniumbicarbonate in order to reduce the U/T concentration to ≤ 2 Urea / Thiourea (U/T). One µg trypsin solution per 50 µg protein was added and the sample was digested over night at RT. For storage, samples were shock frozen and stored at -80°C.
Mass spectrometry analysis was performed on a LTQ-Orbitrap, coupled to a nanoLC system.

2.6.3 Analysis and processing of quantitative mass spectrometry data

Raw files, generated by mass spectrometry analysis for each experiment, were processed using the open source program MaxQuant (version 1.1.1.35) [157]. Each raw file was defined as a separate experiment in the experimental design file to obtain peptide ratios for each peptide detected in each experimental condition. The derived peak list was searched with Andromeda [158] against the human International Protein Index protein sequence database (ipi.HUMAN.v3.68.fasta; 87,083 entries) supplemented with 262 frequently observed contaminants such as human keratins, bovine serum proteins, and proteases and concatenated with the reversed copies of all sequences. Parent masses and fragment ions were searched with initial mass tolerances of 7 ppm and 0.5 Da, respectively. False discovery rates (FDRs) at the peptide and protein levels were fixed at 1%, including automatic filtering on peptide length, mass error precision estimates, and peptide scores of all forward and reversed peptide identifications. Reported protein groups had to be identified by at least one “unique peptide” (a peptide assigned to a single protein group) in order to be accepted as positively detected. Quantification was performed calculating the light-to-heavy (L/H) peptide ratios, considering unique and razor peptides (peptides assigned to multiple protein groups) and a minimum of two ratio counts as a requirement. Unequal protein loading was corrected by normalization of peptide ratios. Assuming that the majority of proteins show no differential regulation, the median of their logarithms was equalized to zero [157].
The obtained data was further processed using the Perseus software 1.3.0.3 (Max Planck institute of biochemistry). L/H ratios were converted into log2 values. Ratios of reverse labeling experiments were inverted beforehand. Cutoffs for proteins deemed as differentially expressed were set to a L/H ratio larger than 1.5. For each data set, proteins with positive detection in both labeling conditions in at least one stimulation time point were considered as positive hits. The gene ontology database [159] was used for the annotation of proteins as mitochondrial, cytoplasmic or nuclear according to the cellular component categorization.

2.7 Bioluminescence resonance energy transfer assay

Protein-protein interactions in living cells were analyzed using bioluminescence energy transfer (BRET). To carry out BRET analyses, two proteins of interest are genetically fused to an energy donor protein (the luciferase RLuc) or to an energy acceptor (the fluorescent protein VENUS), respectively, constituting a BRET pair. If the proteins of interest interact with each other the BRET-tags come into close proximity and energy transfer can occur after oxidation of a luciferase substrate. The detection limit for positive BRET signals is below 100 Å. The resulting acceptor energy emission can be detected and, in proportion to the donor luminescence, results in the BRET ratio [160].

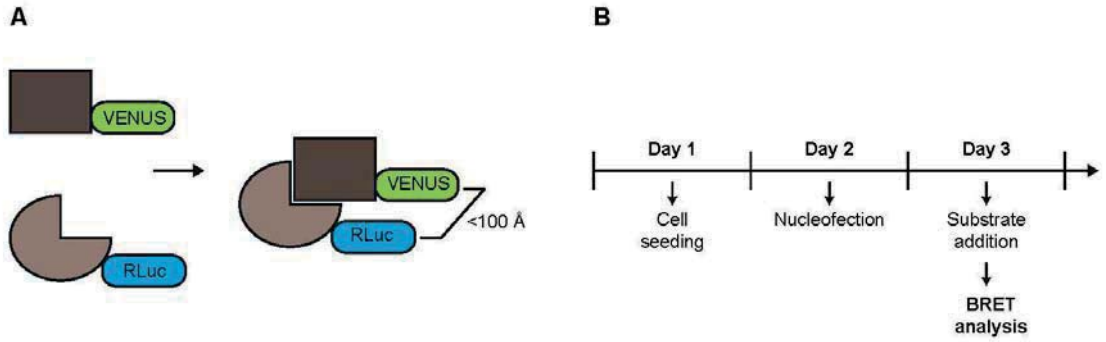

Figure 2-2 Bioluminescence resonance energy transfer assay (A) Overview depicting the interaction of two proteins of interest fused to Renilla luciferase (Rluc) as energy donor and the fluorophore VENUS as energy acceptor, respectively. Energy transfer results in luminescence (BRET signal) when the proteins come into close proximity (<100 Å), indicative for a positive PPI. (B) Time line indicating the basic protocol for BRET assays. Adapted from Gersting et al. [160].

Nucleofection of HEK293 cells was performed using the Cell Line Nucleofector® Kit (100 RCT) (Lonza, Cologne, Germany), applied in 96-cuvette nucleofection plates. For transfection, 1 µg of the BRET expression vectors (with suitable acceptor to donor plasmid concentrations for screening or saturations experiments as described below) was diluted in 10 µl electroporation buffer in 96-well sterile V-bottom plates. Cells were harvested by trypsinization, centrifuged at 600 x *g* for 5 min at 37°C and resuspended in prewarmed electroporation buffer to a concentration of 1.5 x 10^7 cells/ml. 16.6 µl of the cell suspension (2.5 x 10^5 cells) were added to the prepared BRET expression vectors and mixed carefully by pipetting up and down. 20 µl of the DNA-cell-solution mix was transferred to the 96-cuvette nucleofection plates and transfection was performed using the Nucleofector II Device in combination with the transfection program optimized for HEK293 cells (CM-130).

After nucleofection, 80 µl of pre-warmed DMEM without phenol red was added to each reaction and mixed thoroughly. A volume of 50 µl was transferred to 96 well plates with clear

bottom, prepared in advance with 150 µl DMEM per well. 24 h post transfection, 170 µl of the supernatant were aspirated and 70 µl of 30 µM Coelenterazine were added per well. The reaction mix was incubated for 2 min and signals were detected at 485 nm (hRLuc) and 535 nm (BRET signal) over 60 s with a total of 60 intervals. Two types of control experiments were performed in triplicates for every plate: a plasmid coding for a YFP–Rluc fusion protein served as a positive control. As a device-specific negative control, a construct expressing the Rluc-tagged protein of interest with a VENUS-containing construct without fusion partner was co-transfected. The BRET ratio measured was used as correction factor (cf) and subtracted from every BRET pair. BRET ratios were calculated based on the following equation:

$$R = \frac{I_A}{I_D} - cf$$

Figure 2-3 Equation for calculation of BRET ratios. *R* as BRET ratio, I_A as intensity of acceptor luminescence emission at 535 nm, I_D as intensity of donor luminescence emission at 485 nm, *cf* as correction factor (**$BRET_{control}$/ $RLuc_{control}$**)

In order to allow data evaluation, the positive control, the VENUS–Rluc fusion protein, should result in BRET ratios of around R=1.0. A positive interaction of two investigated protein pairs was assumed at $R > 0.1$. For screening experiments, transfection was performed in nucleofection plates in duplicates for each sample and a total plasmid concentration of 1 µg/well with a ratio of 3:1 of acceptor (VENUS) to donor (hRLuc) constructs was used. For saturation experiments, ratios of acceptor to donor vectors were increased sequentially. Specific interactions result in a hyperbolic curve of BRET signals with saturation at high concentrations of acceptor-labeled protein ($BRET_{max}$). By contrast, nonspecific interactions result in BRET signals that increase in a linear fashion with increasing concentrations of acceptor-labeled protein, due to random collision of donor and acceptor [161]. Saturation experiments can also be exploited to monitor relative binding affinities of interaction partners. A relative binding index can be determined measuring the acceptor to donor ratio at half maximal BRET ($BRET_{50}$) [160].

2.8 Determination of oxygen consumption rates

In order to measure the O_2 consumption rate of cells in cell culture a XF96 extracellular flux analyzer (Seahorse Bioscience) was used. This device measures the rate changes over time of dissolved O_2 and pH in medium immediately surrounding adherent cells. For this type of analysis 1205Lu cells were plated in XF96 culture microplates V3-Pet at $3x10^4$ cells per well

in 80µl XF assay medium (Seahorse Bioscience) and allowed to attach and equilibrate over night in an incubator. For stimulation per well, 0.1 µl Lipofectamine RNAiMax and 10-100 ng/ml poly (I:C) and 1 µg/ml 3pRNA were diluted in 10 µl Opti-MEM each and incubated for 5 min. After pooling, the reagents were further incubated for 20 min and then transferred to the 1205Lu cells-containing wells of a XF96 culture microplate. Stimulation was performed 1h or 16h prior to measurements.

Measurements of O_2 and pH were continuously taken over 4 min and the oxygen consumption rates were calculated from the slopes of the concentration changes in these parameters over time. The average of eight replicates was used for data analysis. Baseline rates were measured at six time points before addition of stressors by pneumatic injection into the micro chamber.

The following stressors were applied in the given order and concentrations:

Stressor	Concentration
Oligomycin	2µM
FCCP	5µM
Rotenon	2.5µM
Antimycin A	2.5µM

2.9 Statistics

All data are presented as mean +/- SEM and were analyzed by unpaired Student's t-test or by unpaired, one-way analysis of variance (ANOVA) with the Newman-Keuls multiple comparison test, where appropriate. In all analyses $P < 0.05$ was defined as significant. All statistic calculations were done with Prism GraphPad.

3 Results

3.1 Characterization of changes in the mitochondrial proteome upon stimulation of RIG-I-like receptor signaling

Antiviral signaling upon stimulation of RIG-I-like receptors is a complex and highly regulated process. Due to its location in the outer mitochondrial membrane studies focusing on the RLR adaptor MAVS hypothesized that the surfaces of mitochondria act as signaling platforms for antiviral immune responses. Identifying the components and their spatiotemporal changes of these mitochondrial signaling platforms might help to further understand antiviral responses. The aim of the first part of this study was therefore to analyze changes in the mitochondrial proteome upon stimulation of the RLR signaling cascade.

In order to do that we established cell fractionation protocols, that allowed the extraction of proteins from complete mitochondria, or specifically from the mitochondrial surface and the outer mitochondrial membrane, respectively, and analyzed the isolated protein samples via quantitative mass spectrometry. As the strategy to identify quantitative changes in sample composition upon RLR stimulation, we used SILAC (stable isotope labeling of amino acids in cell culture) a method that is described to very sensitively capture changes in two sets of protein samples. In order to achieve strong and synchronized stimulation pattern in our mitochondria samples, we decided to use high doses of poly (I:C), the synthetic ligand for MDA-5, rather than a virus infection model for stimulation. To capture transient changes in protein levels at early and later time points after activation of RLR-dependent signaling samples were collected at different time points after stimulation.

3.1.1 Identification of a suitable cell culture model

We aimed for a cell culture model matching the following criteria: 1.) Susceptibility to virus infection and RIG-I-like helicase stimulation 2.) Cultivation possible in medium suitable for SILAC analysis 3.) Fully functional antiviral responses 4.) Suitability for mitochondria purification and sub-fractionation.

Since SILAC relies on metabolic incorporation of labeling, primary cells are not compatible with SILAC [162]. Even though, immortalized cell lines are generally well

suited for SILAC, they can exhibit alterations in RLR-signaling cascade and IFN responses (*e.g.* HEK293 cells). After screening a series of human cell lines of different tissue origins we identified the human melanoma cell 1205Lu as the most suitable candidate for our purpose while the other cell lines failed one or more criteria. The 1205Lu cell line has been used in previous studies on RLR-mediated signaling [94] and was additionally found to be suitable for cultivation in SILAC medium and mitochondrial purification protocols in our experimental setup.

In these screening experiments, 1205Lu cells were tested for their susceptibility to viruses and sensitivity to RLR stimulation. 1205Lu cells were infected with 1 MOI recombinant VSV, expressing the viral P-protein fused to GFP for 8 h. Using fluorescent microscopy and as well as electron microscopy we found 1205LU cells to be readily infected by VSV (Figure 3-1E). 24h after stimulation with Sendai virus, VSV as well as poly (I:C) and 3pRNA we detected elevated levels of IP10 and IL6 in the supernatant of cells (Figure 3-1A and B) demonstrating an intact and working RIG-I-like helicase signaling pathway in these cells. In addition, we measured mRNA levels of the IFN-inducible genes RIG-I and PKR and observed induction of expression levels after stimulation compared to unstimulated cells (Figure 3-1C and D).

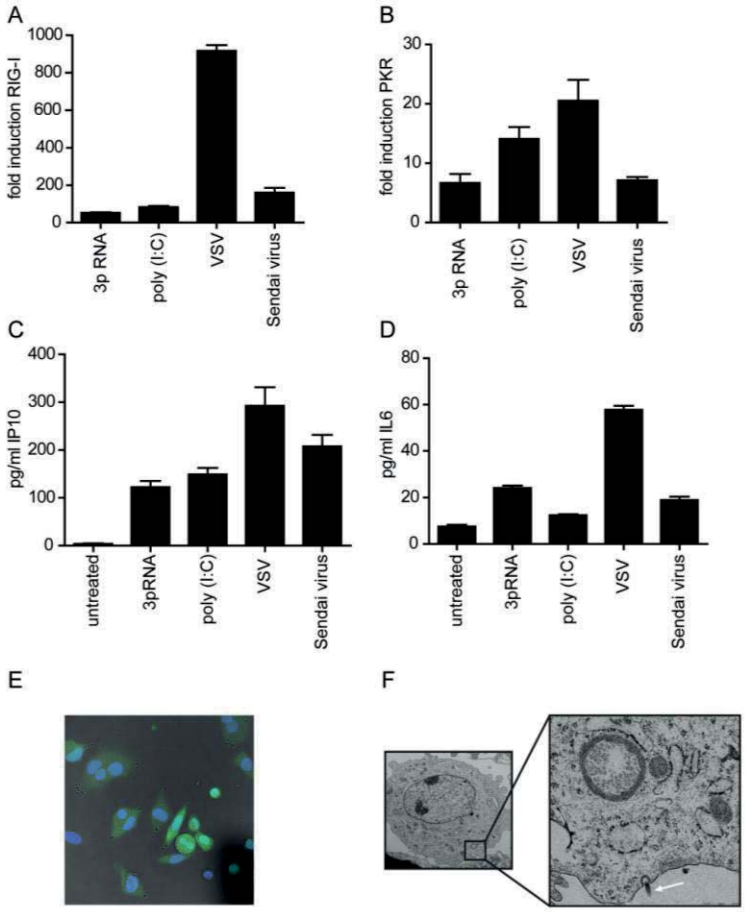

Figure 3-1 Characterization of the RLR signaling cascade in the 1205Lu cell line. 1205Lu cells were transfected with 1 µg/ml 3pRNA and poly (I:C) complexed with lipofectamine as well as infected with 5 MOI VSV and 40 U/ml Sendai Virus. 24 h post stimulation mRNA expression levels for (A) RIG-I and (B) PKR were analyzed by qRT-PCR relative to the housekeeping gene HPRT and are depicted as fold induction compared to expression levels of unstimulated cells. 24 h post stimulation protein levels for (C) IP-10 and (D) IL6 in the supernatant were analyzed by ELISA. Data are shown as mean ± SEM of n=3 (E) Confocal microscopy image of 1205Lu cells infected by recombinant VSV-GFP virus for 8h. Nuclei were stained by Hoechst (blue) (F) Electron microscopy analysis of a 1205Lu cell 1.5h post VSV infection (1600x and 25000x magnification, respectively); white arrow marks a virus particle entering the cell

The MAVS-mediated antiviral immune response is dependent on its localization to the outer mitochondrial membrane [49]. Mitochondria typically form a reticular network radiating from the nucleus and create an interconnected system, complexly coordinated by fission and fusion events. The distribution and morphology of mitochondria in 1205Lu cells was determined using confocal imaging and a mitochondria-specific staining (MitoTracker mxROS). Mitochondria were found to be evenly distributed throughout the cytoplasm of the cells, forming a network of tubular structures (Figure 3-2). MAVS could clearly be located to mitochondria, indicated via the co-staining with the mitochondrial stain. Taken together these results indicate a functional RLH signaling pathway in 1205Lu cells.

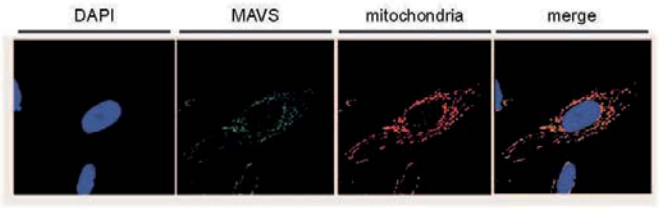

Figure 3-2 Confocal imaging of mitochondria and MAVS distribution in the 1205Lu cell line. Mitochondria were stained with MitoTracker (red), MAVS is visualized by α-MAVS antibody (green), DNA of the nucleus is shown in blue by DAPI staining

3.1.2 Establishing protocols for purification and subfractionation of mitochondria

3.1.2.1 Evaluation of protocols for purification of mitochondria

In order to sensitively capture alterations in the proteins associated with mitochondria upon stimulation of the RLR signaling pathway we aimed for sub-cellular fractionation of the cells to enrich mitochondria and decrease sample complexity. Since it is hypothesized that regulation processes take place mainly at the organelle's surface facing the cytoplasm, we established methods to isolate the outer mitochondrial membrane (OM) and to extract the surface proteins via proteolytic digestion. This was guided by the expectation that mitochondrial subfractionation will reduce the complexity of the sample significantly and therefore will allow a more sensitive detection of changes in proteome composition.

In general, isolation approaches for mitochondria require cell homogenization followed by subsequent steps of purification, which is commonly performed by differential centrifugation. However, the protocols differ dramatically with respect to initial homogenization and usually require adaptations to distinct cell types or tissues. In collaboration with Dr. Hans Zischka (Helmholtz Zentrum München), we optimized the initial rupture of the outer cell membrane through application of a new device and integrated this step into efficient and rapid protocols for purification and subfractionation of mitochondria. We had first screened several rupturing strategies, such as cell homogenization by glass potter, nitrogen cavitation and chemical treatments, for their capability to selectively break the plasma membrane, but not the mitochondrial membranes of our cell culture model. However these strategies did not lead reliably to sufficient yield and quality of isolated organelles for subsequent quantitative MS analysis. Finally, we applied a so-called Balch homogenizer [163], an accurately carved metal apparatus for high-precision cell breakage, as a device for the

homogenization of the samples. When combined with a high-precision pump system, this resulted in an exactly tunable, operator-independent cell homogenization unit that we termed the “pump-controlled cell rupture system” (PCC) (Figure 3-3). The PCC proofed to be generally applicable to the isolation of mitochondria from primary rat liver cells as well as a wide range of cell lines, such as our cell culture model, human melanoma (1205Lu) but also rat hepatoma (McA 7777), human hepatoma (HepG2), human cervical carcinoma (HeLa), and mouse embryonic fibroblasts (MEF). The device was found to be highly efficient for a gentle but efficient lysis of the sample, leaving nuclei and mitochondria intact [164].

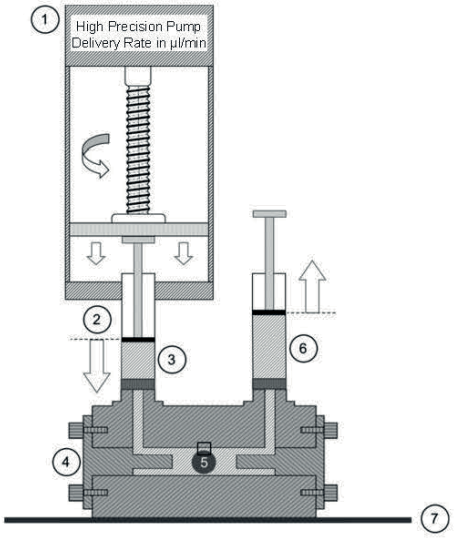

Figure 3-3 The pump-controlled cell rupture system (PCC). A high-precision pump (1) ensures, via gas-tight syringes (2), the continuous sample delivery (3) in a constant rate to the Balch homogenizer (4). Cell breakage occurs on passage through a defined clearance (square), which is adjusted by selecting tungsten carbide balls of different diameters (5). The cell homogenate is collected in a second syringe (6) and can be re-subjected to the homogenizer, which is thermally equilibrated by a cooling plate (7). Adapted from [164].

In order to further increase purity of the mitochondrial preparation, we combined the initial cell rupturing protocol with positive selection of mitochondria using the magnetic activated cell sorting (MACS) technology. The quality of mitochondrial samples, generated with this strategy, was assessed by western blot analysis. The results, shown in Figure 3-4A, demonstrate that in mitochondrial fractions isolated via MACS technology mitochondrial marker proteins (TOM40 and cytochrome C) were highly enriched while the cytoplasmic marker actin and nuclear marker protein histone H3 were decreased to levels near the limit of detection compared to complete cell lysates. Using MACS for mitochondria isolation resulted in a purer mitochondrial fraction than the use of a simple protocol of differential centrifugation and in a higher yield than the use of a gradient centrifugation protocol (Figure 3-4A and data not shown).

In order to selectively analyze proteins associated with the mitochondrial surface, a protocol for proteolytic cleavage and digestion of surface associated proteins by the endoprotease trypsin was established. Enzyme concentrations were titrated to achieve an optimal proteolytic digestion of surface proteins without affecting mitochondrial integrity. Effectiveness of the process was analyzed by western blotting (Figure 3-4B). We found 3 µg of trypsin per mg of protein sample to sufficiently digest cytosolic fractions of integral outer membrane proteins with alpha-helical transmembrane domains (*e.g.* MAVS). The abundance of proteins with a beta-barrel structure, such as VDAC, was strongly reduced after trypsin treatment. Proteins localized inside of the organelle, such as cytochrome C and COX IV, were unaffected by the digestion process. Based on these results 20µg of trypsin per mg protein sample were chosen for subsequent experiments.

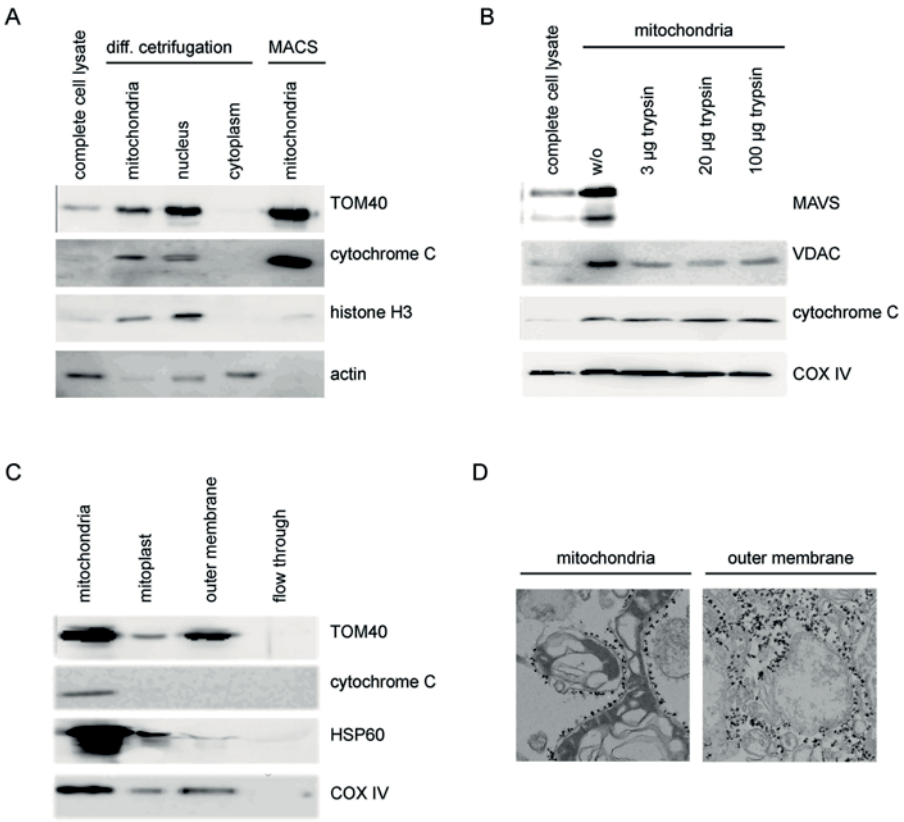

Figure 3-4 Evaluation of mitochondria isolation and subfractionation protocols.
(A) Comparison of mitochondria isolated via differential centrifugation to isolated by MACS technology by western blot (B) Evaluation of surface protein extraction by proteolytic digestion with increasing amounts of trypsin by western blot (C) Western blot analysis of outer mitochondrial membrane fractions in comparison to complete mitochondria extracted by MACS technology. Western blots are shown as representative results of three independent experiments. Equal amounts of protein (20 µg/lane) were loaded per fraction. (D) Electron microscopy image of complete mitochondria and the outer mitochondrial membrane fraction isolated by MACS technology.

We also established a MACS technology-based protocol for the purification of the outer mitochondrial membranes from 1205Lu cells. After purification, mitochondria were subjected to hypo- and hypertonic buffers to induce organelle swelling and rupture of the outer mitochondrial membrane. The outer membrane fraction was separated from the remaining organelle by mechanic shear forces and positively selected using the magnetic activated cell sorting (MACS) technology. Quality of the protocol was assessed by western blot of marker proteins specific for mitochondrial compartments. We found TOM40, a marker protein for the outer mitochondrial membrane to be present in samples of complete mitochondria as well as outer mitochondrial membrane. Proteins of the inter-membrane space (*i.e.* cytochrome C) and the mitochondrial matrix (*i.e.* Hsp60) decreased to a non-detectable level in the outer membrane fraction. Contamination with proteins from inner mitochondrial membranes (*i.e.* COXIV) was still present in the outer membrane fraction, however strongly decreased in compared to unfractionated mitochondria (Figure 3-4C).

In addition, we assessed the purity of mitochondrial and outer membrane samples by electron microscopy (Figure 3-4D). While complete mitochondria revealed an intact outer membrane, surrounding the inner membrane and a densely packed matrix, outer mitochondrial membrane preparation featured loosely distributed membranes without characteristic tubular morphology. However, the circular structures observed in these samples point towards contamination with inner mitochondrial membrane, still attached to the outer membranes, thereby further confirming the results of the western blot analysis.

3.1.2.2 Proteomic analysis of mitochondrial fractions

To further assess the quality of the mitochondrial preparations, the proteome of whole-cell lysates, complete mitochondria, mitochondrial outer membrane, and proteins cleaved of the mitochondrial surface extracted from 1205Lu cells with our protocols were analyzed by LC/MS. The identified protein groups were matched to the GO database [159] to assess their cellular localization (Figure 3-5AC). This showed an increase of mitochondrial annotated protein groups from 14% (whole cell lysates) by three-fold to 42% (complete mitochondria), by four-fold to 68% (mitochondrial outer membrane) as well as to 61% (mitochondrial surface). The ratio of cytosolic and nuclear annotated protein groups strongly decreased after mitochondria purification and sub-fractionation, further confirming the data obtained by western blot analysis.

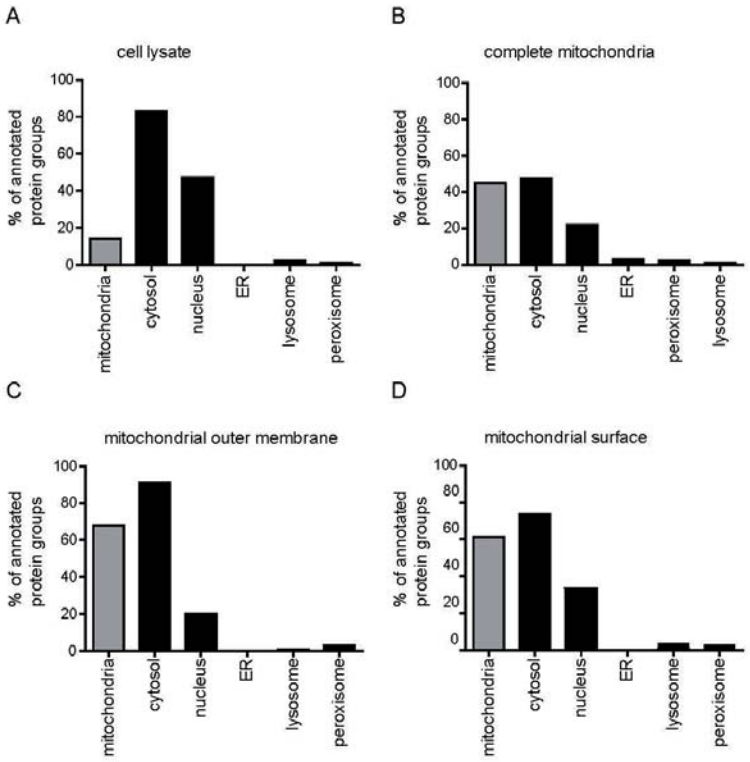

Figure 3-5 Analysis of the GO term enrichment of protein groups for cellular localization. Samples of cell lysate (A), complete mitochondria (B), mitochondrial outer membrane (C), and surface proteins (D) were analyzed by LC-MS. Results show percentage of protein groups with annotations for cellular localization in relation to total amount of protein groups detected.

3.1.3 SILAC: A tool for quantitative shotgun analysis of changes in the mitochondrial proteome upon RIG-I-like receptor signaling

3.1.3.1 Validation of the purification strategy

Stable isotope labeling by amino acids in cell culture (SILAC) allows high-accuracy quantitative proteomics. For SILAC, the entire proteome is labeled by metabolic incorporation of isotypically stable derivates of amino acids, giving rise to two or more distinct populations which can be exposed to differential physiological conditions. The labeling allows simultaneous analysis by mass spectrometry, giving rise to quantitative data. The method allows the combination of samples at a very early time point, reducing the risk of quantitative errors during subsequent processing up to the proteomic analysis. [127].

In order to achieve metabolic labeling, cells were cultivated in DMEM-SILAC medium supplemented with the heavy isotopes [$^{13}C_6$,$^{15}N_4$]-arginine and [$^{13}C_6$,$^{15}N_2$]- lysine and

their light counterparts [$^{12}C_6$,$^{14}N_4$]-arginine and [$^{12}C_6$,$^{14}N_2$]-lysine, respectively. To validate the metabolic interconversion of arginine and proline, we tested arginine concentrations of 48 µg/ml and 42 µg/ml. After an adaptation phase of six cell passages, we analyzed lysates of the heavy-labeled cell population by LC-MS to determine the proportion of labeled peptides as well as arginine-proline conversion rate. As a result, the cell population supplemented with 48 µg/ml arginine showed 93.4% amino acid incorporation for all peptides, with labeling efficiencies of 90.9% for arginine peptides and 93.6% for lysine peptides, respectively. In the cell population cultivated with 42 µg/ml arginine we observed 96.7% amino acid incorporation for all peptides, with labeling efficiencies of 96.4% for arginine peptides and 96.6% for lysine peptides, respectively (Figure 3-6A).

Isotope-coded arginine can be metabolically converted into the amino acid proline. This conversion results in multiple satellite peaks for all proline-containing tryptic peptides in the heavy state, which in turn affects the accuracy of quantitation. Conversion can be circumvented by titration of arginine in order to achieve concentrations in the media suitable for cell viability but without excess of the amino acid. We analyzed proline-containing peptides and did not observe arginine-proline conversions, irrespective of the arginine concentration (Figure 3-6B). On the base of these results, cells were cultivated in SILAC-DMEM supplemented with 42 µg/ml of arginine for subsequent experiments.

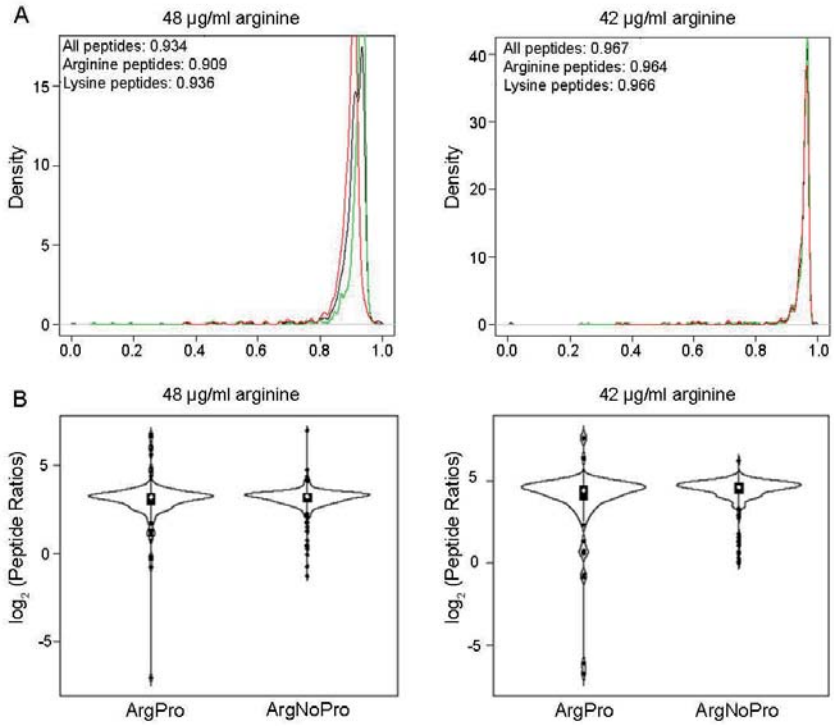

Figure 3-6 SILAC efficiency in labeled 1205Lu cells. (A) Overall incorporation rates evaluated by assessment of peptide ratios between labeled and unlabeled peptides. Ratios for all peptides are depicted in black, ratios for arginine peptides in red, ratios for lysine peptides in green. (Peptide counts - 48 µg/ml: n=1645; 42 µg/ml: n=950) (B) Violin plot depicting the amount and distribution of incorporation rates as log_2 ratios for arginine-containing and arginine/proline-containing peptides in cells cultivated in medium containing 48 µg/ml and 42 µg/ml arginine. The median of each data set is indicated by the black square.

3.1.3.2 Validation of the pooling strategy

A crucial parameter in the setup of SILAC experiments is an accurate pooling strategy for heavy and light samples. Mixing the samples early in the proteomics workflow makes the quantification independent of variations that may be introduced during sample preparation or LC-MS analysis, ensuring optimal accuracy. In the presented experimental setting, pooling of cells before homogenization would have been the earliest suitable time point. A major disadvantage of this strategy however is that virus infection might change the cell status and consequently susceptibility of the cells for homogenization and mitochondria purification. We therefore chose to pool our samples after purification of complete mitochondria based on protein contents of the samples and assessed the quality of this strategy by LC-MS analysis.

By pooling equal amounts of protein, we found the majority of all ratios of labeled and unlabeled peptides of the same sequence to be distributed around a 1:1 ratio in a Gaussian distribution (Figure 3-7A). As a control for the sensitivity of the method we

pooled mitochondria of heavy and light populations in 3:1 and 1:3 ratios (Figure 3-7B and Figure 3-7C). Even though we observed a Gaussian distribution, the disparate pooling of protein contents resulted in a 1.5-fold shift in the mean distribution of the ratios. The results indicated an accurate pooling strategy, sensitive enough to capture changes in SILAC ratios. Consequently, the pooling strategy was used for subsequent SILAC experiments.

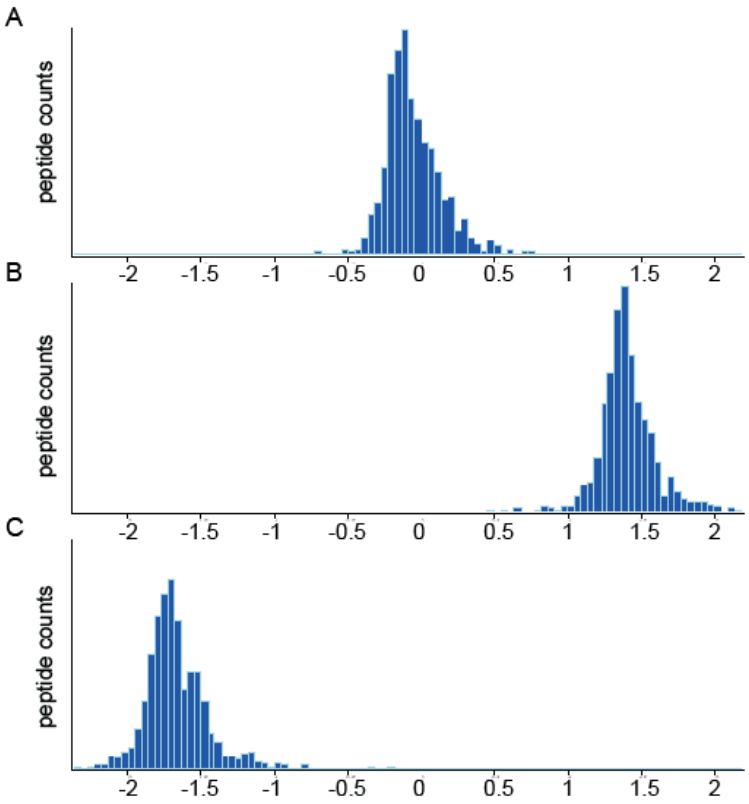

Figure 3-7 Validation of the pooling strategy. Mitochondria extracted from cell populations, cultivated with heavy and light isotopes, were mixed in ratios of (heavy:light) 1:1 (A), 3:1 (B) and 1:3 (C) based on protein content and analyzed by LC-MS. Depicted is the number of peptide counts plotted against the $\log_2$ values of the ratios of peptides with identical sequence containing either heavy or light arginines and lysines.

3.1.3.3 Quantification of changes in the mitochondrial proteome induced by agonists of RIG-I-like helicases via SILAC analysis

In order to assess proteomic changes induced by activation of RLR signaling we stimulated the populations labeled with heavy amino acids with transfected poly (I:C), while the second unlabeled/light population was transfected with non-stimulatory control RNA. To take the highly transient character of protein interactions into consideration, we performed stimulations for 6 h, 1.5 h and 0.5 h prior to mitochondria purification (Figure 3-8). Additionally, we repeated the experiment with crossed-over

treatment conditions (stimulating the unlabeled cells, while treating the cells labeled with heavy amino acids with the control RNA) to exclude the possibility of differences arising from SILAC labeling and experimental variations. Following stimulation, samples of complete mitochondria, mitochondrial surface and mitochondrial outer membranes were generated, resulting in three sample sets.

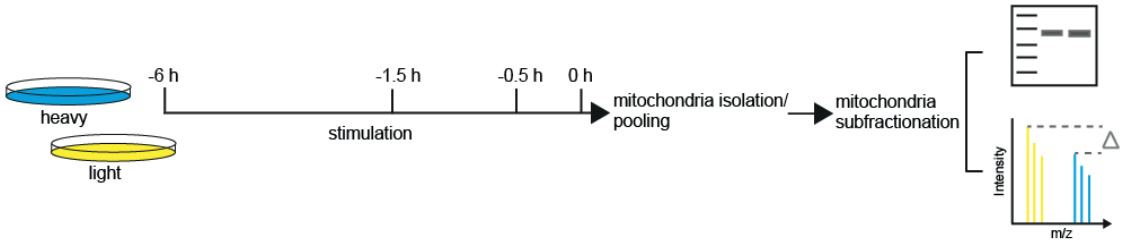

Figure 3-8 Overview of the experimental set-up of the SILAC experiments. Cells were conditioned with light and heavy isotopes of arginine and lysine, respectively, and stimulated with poly (I:C). 6h, 1.5h and 0.5h post-stimulation mitochondria were extracted and pooled according to protein concentrations. For further sub-fractionation, mitochondrial outer membrane was isolated or surface proteins were extracted by trypsin digestion. After partial proteolytic digestion by trypsin, samples were alkalized, reduced and proteolytically digested and then analysed by LC-MS.

Prior to LC-MS analysis we assessed the quality of the purification procedure by western blotting (Figure 3-9A). As a result of the proteolytic digestion, MAVS was not detectable in samples after trypsin treatment. However, COX IV as an inner mitochondrial marker was detectable in all analyzed samples (Figure 3-9B). TOM40 was also found to be enriched in all samples of purified outer mitochondrial membranes, compared to cytochrome C and Hsp60. However, the relative abundances of these marker proteins differed between preparations, indicating considerable sample variations most likely due to the multi-step purification procedure (Figure 3-9C).

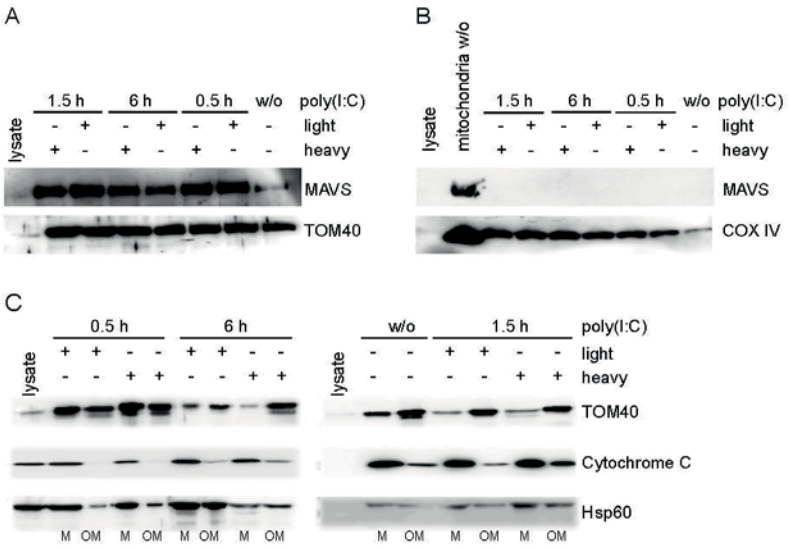

Figure 3-9 Quality assessment of SILAC samples by western blot prior to their analysis by mass spectrometry. The poly (I:C) stimulation pattern in each fraction is indicated by + (stimulated population) and - (unstimulated population). (A) 20 µg of every mitochondrial fraction was analyzed for the enrichment of the mitochondrial markers TOM40 and MAVS and compared to 20 µg of control cell lysates. (B) 20 µg of mitochondrial samples were analyzed after trypsin treatment for reduced abundance of outer membrane marker protein MAVS in comparison to unchanged levels of inner membrane marker protein COX IV (C) 10 µg of outer membrane samples (OM) were analyzed for shifted abundances marker proteins TOM40 (OM), cytochrome C (IMS) and Hsp60 (Matrix) compared to10 µg of mitochondrial fractions (M).

3.1.3.4 Analysis of the proteomic data sets

In collaboration with Dr. Felix Meißner our samples were analyzed in the laboratory of Prof. Matthias Mann by LC/MS on an orbitrap mass spectrometry device. The detected peptides were analyzed by MSQuant [165] and matched to corresponding protein groups. In a second step, contaminating hits, protein groups which could not be matched to true, human protein sequences, were subtracted from the dataset. In order to extract quantitative data indicative for up- or down-regulation of a protein, protein groups labeled by heavy and light amino acids were matched to calculate ratios based on intensities.

In each of the three data sets, we considered protein groups with positive detection in both labeling conditions in at least one stimulation time point. As a result of this analysis, we were able to identify 1947 protein groups in complete mitochondrial samples, 1943 protein groups in the mitochondrial surface samples and 1015 protein groups in samples of the outer mitochondrial membrane (Figure 3-10). By separate analysis of each stimulation time point, we found peptide ratios to cluster in a normal

distribution around a 1:1 ratio, indicating a correct labeling status of the samples. MAVS as a representative marker protein for the mitochondrial surface and RLR signaling cascade was quantified in all except one experimental condition. The protein was expected to be equally abundant in all labeling populations and can be used as a marker that the pooling strategy worked correctly. Indeed peptides derived from MAVS showed ratios of heavy-labeled and unlabeled peptides of around 1:1.

A

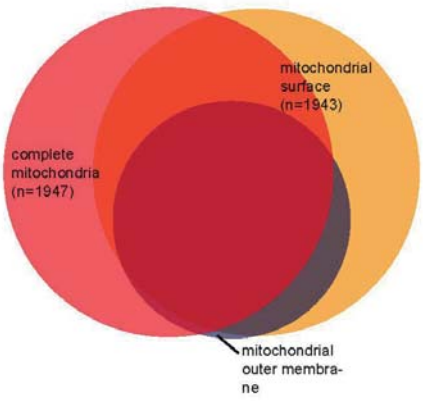

B

Marker protein	Complete mitochondria	Mitochondrial surface	Mitochondrial outer membrane
TOM40	+	+	+
MAVS	+	+	+
RIG-I	-	-	-
MDA5	-	-	-
LGP2	-	-	-
TRAF3	-	-	-
IRF3/IRF7	-	-	-
PCBP2	-	+	-
MFN2	+	-	-

Figure 3-10 Analysis of three SILAC datasets combined. (A) Venn diagram depicting the number of protein groups detected per SILAC experiment (all stimulation time points combined) and overlapping hits within measurements (B) Overview of marker proteins and their presence in each dataset with (+) indicating positive detection and (-) indicating lack of detection.

To identify mitochondria-associated candidate proteins that potentially play a role in the response to RLR-stimulation we screened the data sets for protein groups with at least 1.5 fold up- or down-regulation in both labeling conditions in a time point dependent manner. The analysis gave rise to 25 regulated protein groups for the complete mitochondrial proteome, of which 19 hits were down-regulated and 6 hits were up-regulated. For the mitochondrial surface proteome 32 regulated protein groups were detected with 23 down-regulations and 9 up-regulations, respectively, and in the outer mitochondrial membrane proteome 98 regulated hits were detected with 96 down-regulations and two up-regulations. A complete list of all regulated proteins identified with their respective ratios is indicated in 8.4.

Furthermore, the generated datasets were screened for known marker proteins of antiviral signaling (Figure 3-10B). We did not find any of the RLR receptors or any of the known downstream effector molecules besides MAVS in the datasets. However, we were able to detect PCBP2, a negative regulator of MAVS in samples of mitochondrial surface proteins [64]. It was found to be 1.9 fold up-regulated after 1.5 h and 2 fold

down-regulated again after 6h post-stimulation compared to the unstimulated condition. Additionally, protein kinase R (PKR) was present in datasets of complete mitochondria and mitochondrial surface. The protein was five-fold down-regulated in the proteome of complete mitochondria in 5 of 6 stimulated conditions and in 4 of 6 stimulated conditions for the mitochondrial surface proteome. PKR was the only hit to be reproducibly regulated over time and in more than two experimental settings.

3.1.3.5 Bioinformatic annotation of cellular compartments

In order to annotate the identified protein groups to their respective cellular compartment, the datasets were matched to the Gene Ontology database [159] and filtered for a mitochondrial, cytosolic and nuclear localization (Figure 3-11). As a result we found 30.2% mitochondrial annotations 28.5% nuclear and 77.1% cytoplasmic annotations in datasets of complete mitochondria (Figure 3-11A). Analysis of the dataset from mitochondrial surface revealed 24.5% mitochondrial, 38.8% nuclear and 75.1% cytoplasmic annotated hits (Figure 3-11B). For the dataset derived from mitochondrial outer membrane sample we observed 31.1% mitochondrial, 25.5% nuclear and 78.6% cytoplasmic annotations (Figure 3-11C).

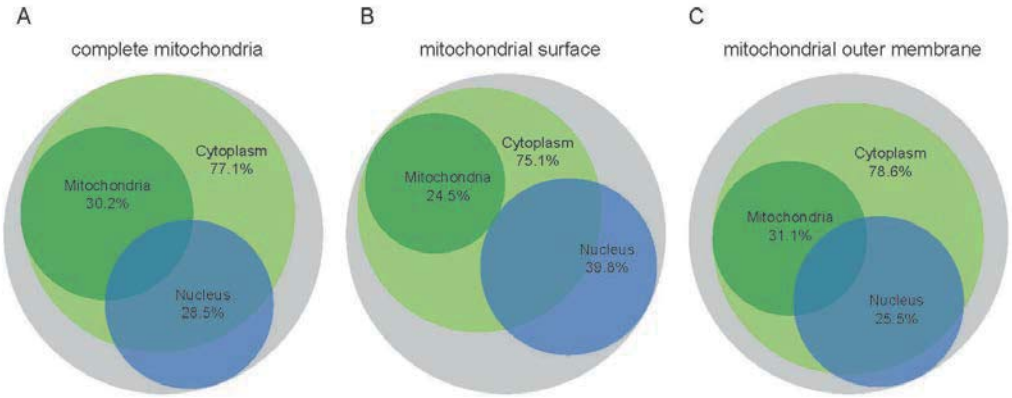

Figure 3-11 Analysis of protein groups per mitochondrial fraction in regard to annotations to cellular compartments. Protein groups were matched to the gene ontology database for cellular compartments (all stimulation time points combined). Depicted is the percentage and overlap of protein groups annotated to cytoplasm (light green), mitochondria (dark green) and nucleus (blue) relative to the overall number of detected protein groups (grey).

3.1.4 Functional validation of candidate proteins selected from the mass spectrometry data set

3.1.4.1 Selection of candidate proteins for further functional evaluation

We next attempted to validate the SILAC quantification results on a smaller subset of proteins. For further evaluation, we performed literature research on the regulated proteins and screened for potentially interesting implications in antiviral signaling. Based on this analysis we chose 12 of these proteins as candidates for further functional test. Nine of the candidates were found to be down-regulated two candidates were up-regulated at one or more time points during SILAC analysis. Interestingly, the candidate protein PCBP2 showed up-regulation as well as down-regulation in the data set of mitochondrial surface.

Protein name	Gene name	Regulation
heterogeneous nuclear ribonucleoprotein L	HNRNPL	
protein kinase R	EIF2AK2	
DEAD (Asp-Glu-Ala-Asp) box polypeptide 18	DDX18	
alpha-1-antichymotrypsin	SERPINA3	
apoptotic chromatin condensation inducer 1	ACIN1	
interleukin enhancer-binding factor 3	ILF3	
enhancer of mRNA-decapping protein 4	EDC4	
poly(rC)-binding protein 2	PCBP2	
superoxide dismutase 2	SOD2	
staphylococcal nuclease and tudor domain containing 1	SND1	
double-stranded RNA-binding protein 1	STAU1	
insulin-like growth factor-binding protein 2	IGFBP2	

Figure 3-12 Overview of candidate proteins picked for functional analysis. Based on literature research twelve proteins were selected for further evaluation. Down-regulations in the SILAC data sets are indicated in red, up-regulations in green, conflictive regulation patterns are shown in yellow.

3.1.4.2 Functional analysis of candidate proteins

Two diverging approaches were considered for further analysis of the chosen candidates: Firstly, a confirmation of SILAC results by western blotting as an independent experimental approach. Secondly, a functional characterization of the proteins in context of cellular antiviral responses.

Recapitulation of regulation levels of the proteins by western blotting posed the challenge of highly transient association and dissociation processes during antiviral signaling and different sensitivity levels of the two assays. The analysis of previously published literature revealed two candidate proteins, namely EIF2AK and PCBP2, with already described implications in antiviral signaling [64, 166]. Expansion of the literature analysis additionally showed potentially interesting characteristics for the ten remaining candidate proteins and possible direct or indirect impact on antiviral signaling. We consequently chose the functional characterization of candidates over western blot analysis for initial analysis.

In order to test the impact of our candidate proteins on RLR dependent signaling or the release of infectious particles, we chose to perform a small-scale loss-of-function assay of the respective candidate protein via siRNA knockdown. Since these knockdown assays are simple to control and do not require elaborated establishment of specific cell lines, we chose this method over a complete knock-out or over-expression assays.

We designed two siRNAs for each of the 12 candidates and tested their knockdown efficiencies in 1205Lu cells by qRT-PCR. 48 h after transfection, we observed reduced expression levels for all target mRNAs by 50-95% compared to expression levels of control cells (Figure 3-13A). Furthermore, a cell viability assay was performed to exclude the possibility of increased cell death due to abrogation of potentially essential mRNA levels. As a result, we did not see reduced viability compared to control transfected cells (Figure 3-13B). Taken together, the data suggests a positive knockdown efficiency for all designed siRNA without affecting cell viability, hence being suitable for further experiments.

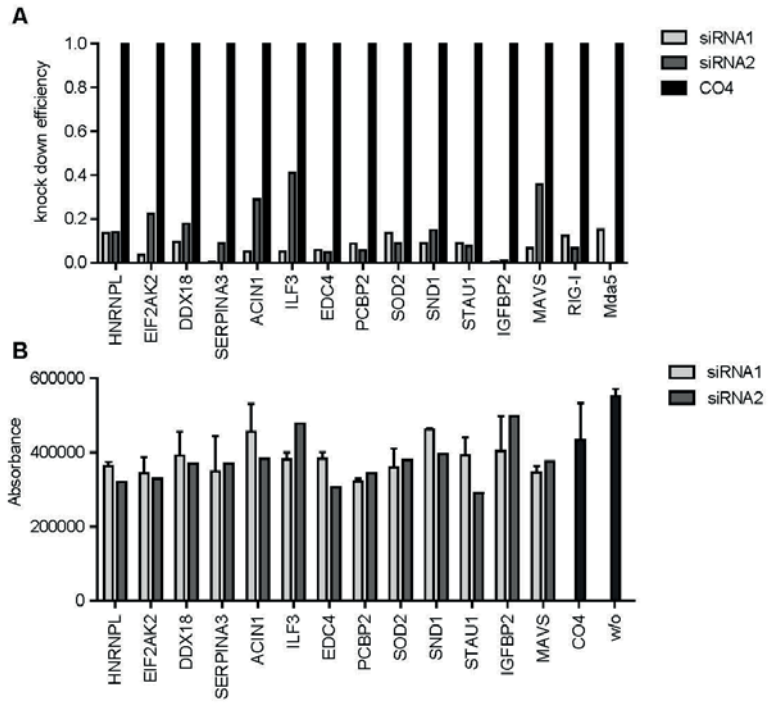

Figure 3-13 Evaluation of knockdown effects in 1205Lu cells. (A) Knockdown efficiency of siRNA targeting 12 candidate as well as components of the RLR signaling cascade were analyzed by qRT-PCR. Results are shown as fold regulation normalized to respective expression levels of mRNA from control transfected cells (B) Cell viability, detected by cell titer blue assay, after two transfections of siRNA. Absorbance was detected at 570 nm.

In order to test the implication of candidates for antiviral responses, we stimulated MAVS-dependent signaling by transfection of 1 µg/ml poly (I:C) 48 h after knockdown of candidate mRNAs. 6 h post-transfection, mRNA levels were analyzed for IFN-ß expression. Knockdown of MAVS and MDA5 as components of the RLR signaling cascade served as an internal control for the experimental setup. As expected, knockdown of these targets led to a significant decrease in IFN-ß expression levels. Interestingly, we observed significant increase of expression levels after knockdown of HNRNPL by four fold. Furthermore, stimulation after knockdown of DDX18 and SOD2 led to significant decrease of IFN-ß expression by two fold and 10 fold, respectively.

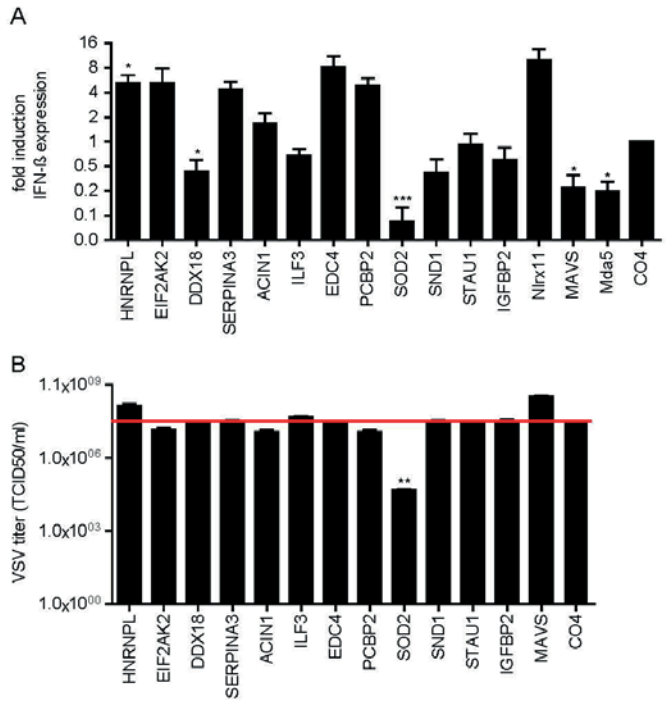

Figure 3-14 Validation of the impact of candidate proteins on antiviral signaling in loss-of-function experiments. (A) Changes of IFN-ß expression relative to HPRT as a reference on mRNA level were analyzed by rtPCR after knockdown of candidate mRNAs for 48 h and stimulation with 1µg/ml poly (I:C) for 6h, shown is the fold induction, normalized to the non-targeting control CO4. Depicted are results from four independent experiments ±SEM (***$P < 0.001$, $P < 0.05$, by unpaired *t*-test). (B) Cells were infected with VSV 10 fold dilutions 48 h after knockdown. Shown are representative results of two independent experiments with four replicates. ±SEM (**$P < 0.005$, by unpaired *t*-test).

In addition we aimed to investigate the role of candidates for virus replication/infection. We infected HEK293 cells with VSV 48 h after knockdown and analyzed the amount of infectious particles by median tissue culture infective dose (TCID50) assay (Figure 3-13). As expected, virus load increased from $3.2x10^7$ by 10 fold to $3.2x10^8$ in cells after MAVS knockdown compared to control cells. Strikingly, we observed a drastic decrease in virus titers by five fold in SOD2 knockdown cells to $5.6x10^4$. Virus infection is a process composed of several steps (attachment, membrane penetration, virus uncoating, transcription and translation as well as assembly and release) and SOD2 might also have an implication in any one of these steps. The drastically reduced susceptibility of the cell towards virus infection after depletion of SOD2 might thus be independent of the effect of SOD2 on antiviral signaling. On the other hand, it has previously been shown that expression of IFN type I is necessary to establish expression of viral genes [167]. The strong decrease of IFN-β in SOD2-depleted cells might possibly affect the virus replication cycle.

These results suggest SOD2 has a possible functional role in the context of antiviral signaling and virus infection. Further studies will have to investigate in more detail the role of SOD2 and the other candidates in antiviral immune responses.

3.2 The interplay between mitochondrial function and RIG-I-like receptor signaling

3.2.1 Respiration rate is decreased after stimulation of RIG-I-like receptor signaling

Mitochondria are an integral platform for antiviral signaling, apoptosis, ATP production as well as stress sensing and it has previously been shown that antiviral signaling is intimately linked to mitochondrial function [168]. In the following experiments we aimed to investigate if mitochondrial function is in return influenced by RLR and MAVS activation and specifically investigated if MAVS-dependent signaling alters the mitochondrial respiration rate.

In order to investigate the mitochondrial oxidative phosphorylation, we determined the oxygen consumption rate (OCR) using the label-free *Seahorse XF96* assay. OCRs were analyzed in cells stimulated with transfected poly (I:C) and 3pRNA, both synthetic activators of RLH and MAVS-dependent signaling, as well as untransfected poly (I:C) and LPS, ligands for TLR3 and TLR4, respectively. 1 h and 16 h were selected as time points for the analysis to capture effects directly after pathway activation and effects taking place in the IFN type I feedback loop (Figure 3-15).

1h after transfection of poly (I:C) or 3pRNA we found OCRs to be reduced by 10% compared to the OCR from control-transfected cells. This effect was increased over time, leading to a reduction of OCRs by 75% and 20% 16 h after RLH activation with poly (I:C) and 3pRNA respectively, in comparison to unstimulated control cells. Upon stimulation with untransfected poly (I:C), we did not observe significant changes of OCRs relative to unstimulated cells, regardless of the time points analyzed. Stimulation of cells with LPS led to a decrease of the cell's respiratory rate by 22% after 1 h compared to control. Strikingly however, this effect of LPS was abolished 16h post stimulation.

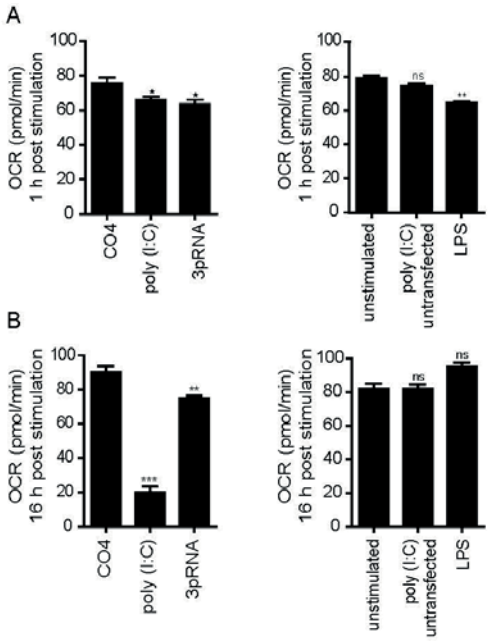

Figure 3-15 Analysis of basal OCR upon stimulation of innate immune signaling. 1205Lu cells were stimulated with transfected 100 ng/ml poly (I:C), 1 µg/ml 3pRNA and 100 ng/ml CO4 RNA, as well as 5 µg/ml untransfected poly (I:C) and 10 ng/ml LPS. Basal OCRs were assessed 1h (A) and 16h (B) post stimulation. Depicted are representative results from three independent experiments performed as sextuplicates, respectively. Data is given as mean ± SEM of n=6. (***p < 0.001, **p < 0.01, *p < 0.05, by unpaired t-test.

We next aimed to investigate if there was a dose-dependency of the effect observed for poly (I:C) transfection. For this reason we transfected cells with two different concentrations of poly (I:C) and assessed the OCR 1 h later. We found, that already 10-fold less concentrated poly (I:C) was sufficient to induce the same level of reduction of OCR in 1205Lu cells 1 h post transfection (Figure 3-16).

RLR activation is known to be able to induce apoptosis [94]. In order to exclude the possibility that changes in OCR are a result of differences in cell number due to cell death induction by poly (I:C) we measured protein concentration via bradford assay and looked for apoptosis and cell death using flow cytometry after annexin/PI staining in the cells that were assayed in the *Seahorse XF96 analyser*. According to these assays we observed no significant changes in protein mass or viability after stimulation (Figure 3-17).

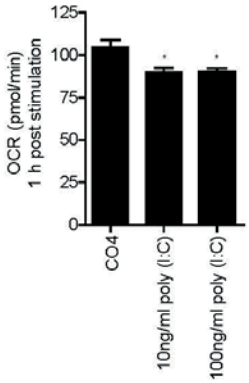

Figure 3-16 Analysis of OCR upon stimulation with different poly (I:C) concentrations. 1205Lu cells were transfected with 10 ng/ml, 100 ng/ml poly (I:C) and 100 ng/ml CO4 RNA. Basal OCRs were assessed 1 h post stimulation. Depicted are representative results from three independent experiments performed as sextuplicates, respectively. Data is given as mean ± SEM of n=6. (***$P < 0.001$, **$P < 0.01$, *$P < 0.05$, by unpaired *t*-test).

Malignant transformation of cells (*e.g.* during tumor development) is also often characterized by increased aerobic glycolysis, leading to decreased oxygen consumption despite the presence of oxygen in the environment. This metabolic shift is known as the Warburg effect [169]. However, under physiological conditions non-mitochondrial respiration represents only 10% of the oxygen consumption and oxidative phosphorylation is the main source for differentiated cells to generate ATP [170]. The process of oxydative phosphorylation relies on a tightly controlled interplay between the membrane bound electron transport chain complexes I-V. Deregulation of one of these complexes can ultimately lead to alterations in mitochondrial respiratory capacities.

To address the question if stimulation of innate immune signaling leads to alteration of distinct parameters in mitochondrial respiration we performed a mitochondrial bioenergetic profile on cells transfected with poly (I:C), control-transfected cells and unstimulated cells using the XF96 Seahorse analyzer. In order to assess the specific aspects of mitochondrial respiration namely basal respiration, O_2 used for ATP turnover, O_2 spend by proton leakage, maximum respiration capacity and non-mitochondrial respiration the cells were exposed to inhibitors of the electron transport chain at subsequent time points and the OCR was determined over a period of 2 h (Figure 3-18A). The ATP synthase inhibitor oligomycin was applied to give information on the amount of oxygen specifically utilized for the generation of ATP. Subsequent addition of FCCP, a protonophore disrupting the membrane potential of the inner mitochondrial membrane and leading to accelerated electron transportation without the

production of ATP, was used to investigate maximal oxidative capacity of mitochondria. Finally, antimycin A and rotenone (inhibitors of complex III and complex I, respectively) were added to block mitochondrial respiration per se, giving information on mitochondria-independent oxygen consumption

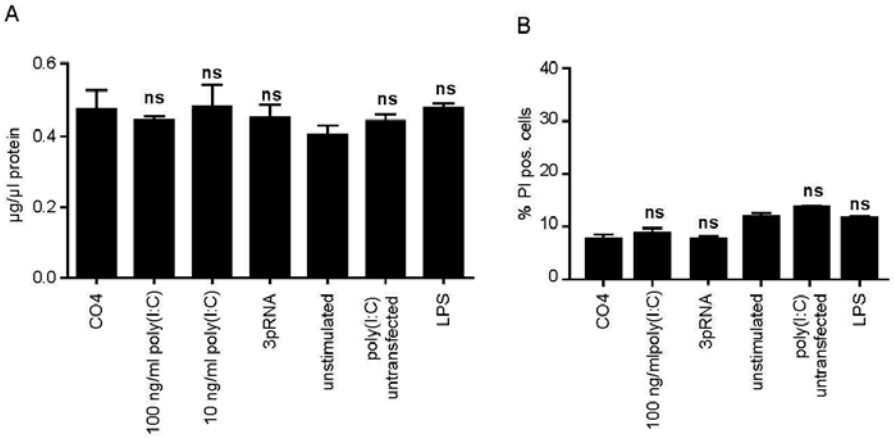

Figure 3-17 Assessment of viability upon stimulation of innate immune signaling.
(A) Assessment of protein concentration via bradford assay was performed after every OCR analysis. Each data point represents average of 8 values ± SEM. p-values for poly (I:C) and 3pRNA transfected groups were calculated relative to CO4 control groups, p-values for untransfected poly (I:C) and LPS stimulated groups were calculated relative to unstimulated group. Depicted are representative results from six independent experiments (ns, by unpaired *t*-test). (B) 1205Lu cells were stained for propidium-iodide as a reference for cell death 16h after transfection of 100 ng/ml poly (I:C), 1 µg/ml 3pRNA and 100 ng/ml CO4 RNA, as well as 5 µg/ml untransfected poly (I:C) and 10 ng/ml LPS. Shown are means of three independent experiments ± SEM, p-values for poly (I:C) and 3pRNA transfected groups were calculated relative to CO4 control groups, p-values for untransfected poly (I:C) and LPS stimulated groups were calculated relative to unstimulated group (ns, by unpaired *t*-test).

In cells that have sufficiently active glycolysis to support metabolism while mitochondrial function is manipulated, all of the major aspects of mitochondrial coupling and respiratory control can be measured in a single experiment [171]. The sequential addition of the ATP synthase inhibitor oligomycin, the protonophoric uncoupler FCCP, and the electron transport inhibitors such as rotenone and antimycin A allows determination of basal respiration, ATP turnover, proton leak, coupling efficiency, maximum respiration rate, apparent respiratory control ratio, spare respiratory capacity and non-mitochondrial respiration (Figure 3-18 A). Basal respiration rates, usually strongly controlled by ATP turnover and partly by substrate oxidation and proton leak [172], were assessed before the addition of stressors (Figure 3-18 B. condition a). The rate of oxygen consumption devoted to mitochondrial ATP synthesis was estimated from the decrease in respiration upon inhibition of the ATP synthase with oligomycin (Figure 3-18 B. condition c) and the respiration rate in the presence of oligomycin

(Figure 3-18 B, condition b) was taken as a direct measurement for proton leak across the mitochondrial membrane. Maximum respiration rates were assessed by addition of the uncoupler FCCP (Figure 3-18 B, condition d). The remaining oxygen consumption in the presence of rotenone and antimycin A allowed the determination of non-mitochondrial respiration (Figure 3-18 B, condition e) and was subtracted from all other rates.

As a result, we observed significant reduction of oxygen consumption devoted to ATP synthesis in poly (I:C)-stimulated cells compared to control cells, whereas oxygen consumption for maximal mitochondrial respiration and proton leak were unaltered (Figure 3-18 C). These results imply that the reduced oxygen consumption after poly (I:C)-dependent MAVS activation is caused by a specific down-regulation of mitochondria-mediated ATP synthesis.

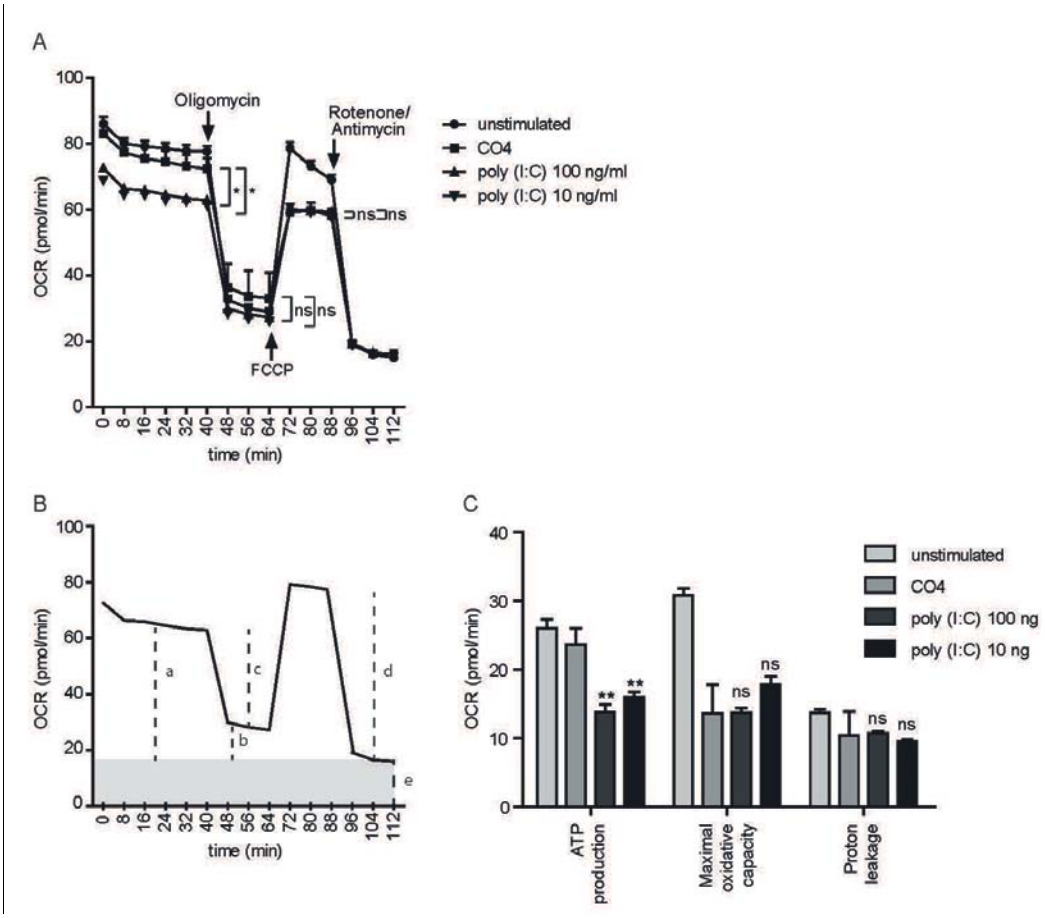

Figure 3-18 Oxygen consumption rate upon transfection with poly (I:C) in the presence of stressors of the mitochondrial respiratory chain. (A) OCRs were assessed in 1205Lu cells 1h after transfection of poly (I:C) (10 ng/ml and 100 ng/ml) and 100 ng/ml CO4 RNA. Oligomycin (1 µM), FCCP (10 µM), antimycin A (1 µM), and rotenone (1 µM) were injected at subsequent time points as indicated. Shown are the results of one experiment representative of two with 8 replicates presented as mean ± SEM, p-values were calculated relative to CO4 control group (* $p < 0.05$, by unpaired *t*-test). (B) Schematic of a representative respiratory control experiment, indicating basal OCR (a), proton leak (b), ATP turnover respiration (c), maximal respiration (d) and non-mitochondrial respiration (e). (C) Based on the data generated in (A), relative OCR level ± SEM devoted for ATP consumption, maximal respiration rate and proton leak were calculated. p-values

were calculated by unpaired *t*-test for poly (I:C)-transfected experimental conditions relative to CO4 control group and the CO4 group relative to the unstimulated condition.

3.2.2 No changes of components of the respiration chains upon stimulation

The regulation of mitochondrial respiration activity can be accomplished by several means. The simplest mechanism involves the feedback of substrates for an enzymatic reaction, such as ADP and P_i, for the ATP synthetic reaction. However, it has been shown in several systems, such as the heart, that large changes in mitochondrial synthetic rate are not associated with significant alterations in the substrates for ATP production or the net free energy in cytosolic ATP [173]. Altered respiratory rates can furthermore result from uncoupling of the respiratory chain and from altered expression levels of components of the ETC complexes [174-176]. The major mechanism for modulating mitochondrial respiration rates however involves covalent posttranslational modifications (PTMs) to alter the activity of single respiratory chain complexes [177-179]. Furthermore, PTMs have been shown to modulate the activity of mitochondrial respiratory chain complexes to allow metabolic homeostasis in the face of persistent and acute changes in energy demand [180].

To examine whether the reduced OCR upon stimulation of MAVS-dependent signaling might be caused by alterations in expression levels of ETC complexes, we performed western blotting with an OXPHOS antibody cocktail, recognizing subunit I-V of the ETC. 24 h after exposition to transfected poly (I:C) and 3pRNA, as well as untransfected poly (I:C), the relative expression of components of the ETC was not altered in comparison to control cell lysates (Figure 3-19A). However, the stimulation of poly (I:C) and 3pRNA led to increased protein levels of IP-10 in the supernatant of the cells, indicating a robust activation of RLR signaling after stimulation with poly (I:C) and 3pRNA.

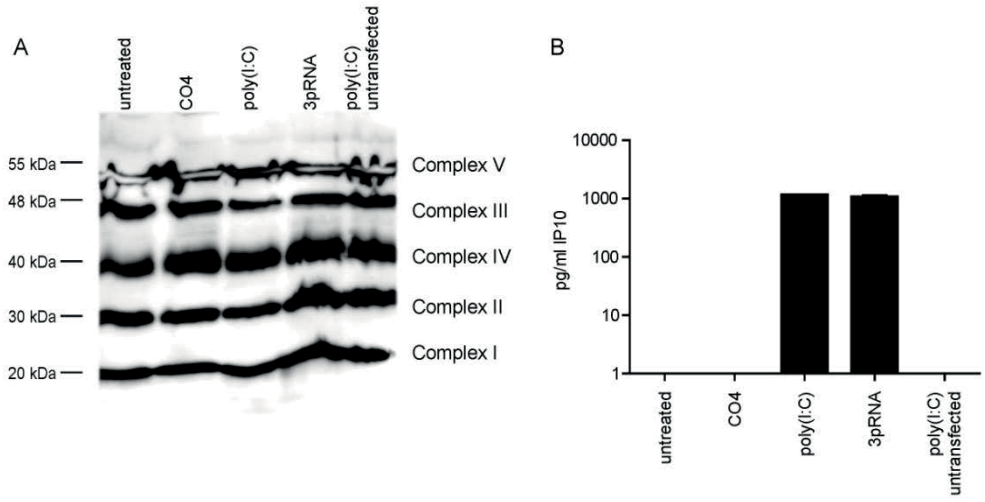

Figure 3-19 Western Blot analysis of OXPHOS complexes I-V in lysates after 24h stimulation with RLH ligands. (A) Expression profile of complex I-subunit NDUFB8, complex II-30kDa, complex III-Core protein 2, complex IV-subunit I and complex V-alpha subunit of 1205Lu cells transfected with 100 ng/ml poly (I:C), 1 µg/ml 3pRNA and 5 µg/ml poly (I:C) (untransfected) to cells untreated and cells transfected with CO4 were compared. (B) Supernatants of the cells were analyzed for IP10 levels by ELISA. Data are shown as mean ± SEM of n=3.

3.2.3 ROS levels are unaltered in response to RLR stimulation

Reactive oxygen species (ROS) have previously been shown to be implicated into modulation of MAVS-dependent signaling [150]. Given that alterations of the respiratory chain can cause elevated levels of ROS besides decreasing the OCR, we examined mitochondrial ROS levels in cells 6h and 48h post-transfection of poly (I:C) and 3pRNA. We used staining with MitoSox, a fluorescent dye activated by mitochondrial superoxide oxidation, followed by analysis with confocal microscopy and FACS to measure mitochondrial ROS production. As expected the MitoSox dye was specifically targeted to mitochondrial structures, as shown in confocal microscopy (Figure 3-20A). Compared to a positive control consisting of treatment with the complex III inhibitor antimycin A no relevant induction of mitochondrial ROS was seen 6 h and 48 h post stimulation with poly (I:C) and 3pRNA, (Figure 3-20B). Taken together, the data indicate that activation of MAVS-dependent signaling affects mitochondrial function leading to decreased respiratory O_2-consumption, without excess generation of mitochondrial ROS.

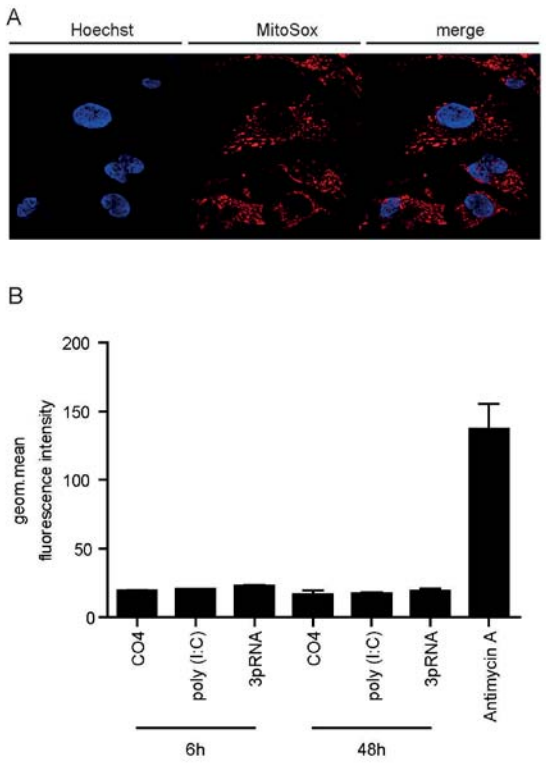

Figure 3-20 Analysis of mitochondrial ROS levels upon RLR stimulation. (A) Confocal microscopy analysis of 1205Lu cells stained with MitoRos. MitoROS stain is shown in red, nucleic DNA was stained by Hoechst, shown in blue. (B) FACS analysis of mitochondrial ROS levels by MitoSOX stain in 1205Lu cells stimulated with 100 ng/ml poly (I:C) and 1 µg/ml 3pRNA for 6 h and 48 h and 1205Lu cells treated with 100 µm antimycin A for 6 h. Data are shown as mean ± SEM of n=3.

3.3 MAVS signaling depends on peroxisomal integrity

MAVS was initially described as a strictly mitochondrial protein, but was recently also detected at peroxisomal membranes. Peroxisomal MAVS has been shown to be important for an adequate antiviral response, establishing a transient anti-viral state in cells independent of IFN type I [50]. In order to get clues for the molecular basis of MAVS-mediated signaling on peroxisomes and the translocation of MAVS to peroxisomes a BRET assay was used in collaboration with the Molecular Pediatrics laboratory of Prof. A. Muntau at the Dr. von Hauner Childrens' Hospital (LMU, Munich) to screen a library of peroxisomal proteins for interaction partners of MAVS. To study location-specific interactions of MAVS, we generated and implemented three differently targeted variants of MAVS into the screen with localization in both organelles (MAVSwt) or exclusively on mitochondria (MAVSmito) and peroxisomes (MAVSpex), respectively. The protein STING, previously described as interacting with MAVS [56], was additionally included in the screen.

BRET is a powerful tool for the evaluation of protein-protein-interactions (PPIs). The method provides enhanced sensitivity in living cells compared to other techniques, such as fluorescence resonance energy transfer (FRET) as it does not require an external excitation source, which often results in photo bleaching or auto-fluorescence.

3.3.1 Identification of interaction partners of MAVS in the peroxisomal proteome

3.3.1.1 Construction and validation of MAVS and Sting plasmids for BRET-assays

BRET relies on the fact that the energy derived from a luciferase reaction can be used to excite a fluorescent protein if the latter is in close proximity to the luciferase enzyme. In our setting BRET was used to test if luciferase-fused donor proteins interact with-acceptor proteins fused with the YFP-variant Venus. However, the fusion of a protein to the Venus fluorescent protein or luciferase can alter its location, function and the capacity for interaction with other proteins. Whether this happens can depend on the location of the fusionprotein at the C or N-terminus. To increase our chances of functional interactions, we therefore used N-terminal as well as C-terminal tags for both interaction partners in our screen. This resulted in eight possible combinations of the differently fused variants for every tested protein pair.

First, we cloned the cDNAs of STING and the MAVS variants into BRET vectors bearing the required tag combinations. To confirm different localization of the VENUS-tagged MAVS proteins after over-expression, we used confocal imaging and co-staining of mitochondria with a mitotracker dye. We could see an expected localization pattern for all N-terminally tagged proteins. STING-N-VENUS showed the expected partial overlap with mitochondrial stain [56]. MAVSwt-N-VENUS also showed overlap with mitochondrial stain. However, next to this tubular pattern, also dotted structures were visible with no co-localization to mitochondria, resembling the distribution previously described by Dixit and colleagues [50]. MAVSpex-N-VENUS showed a distribution compatible with the expected peroxisomal localization and MAVSmito-N-VENUS showed an exclusively mitochondrial localization. Due to interference of the fusion protein with the C-terminal transmembrane/localization sequence C-terminally tagged MAVS proteins were mislocalized to the cytoplasm. We therefore concluded that at least addition of N-terminal tags to MAVS variants and STING did not affect its localization and its capacity to interact with proteins in a physiological setting.

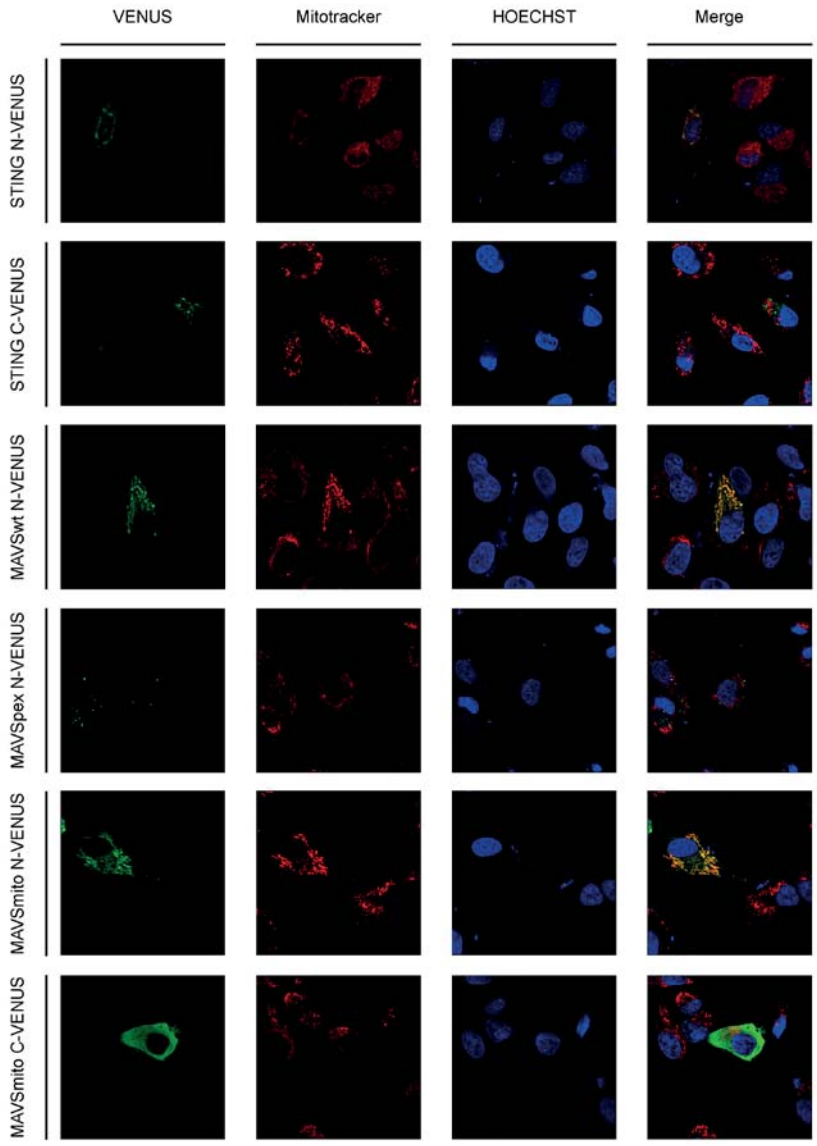

Figure 3-21 Life cell imaging to localize VENUS-fusion variants of MAVS targeted to mitochondria and peroxisomes respectively. Hela cells were transfected with VENUS tagged MAVS constructs 24h prior to analysis (green). Mitochondria were stained by MitotrackerRed (red). Nuclei were stained by Hoechst (blue).

To validate our BRET system we first tested the previously described interaction of MAVS and STING [56, 57] as binary interaction in our BRET set-up. A positive interaction between a protein pair was assumed if at least one out of eight tested tag combinations resulted in a BRET ratio above 0.1, which is a method-specific threshold. Co-transfection of both N-Luc-MAVS with N-Venus-STING and N-Luc-STING with N-Venus-MAVS resulted in BRET ratios above the method-specific threshold for positive PPI (Figure 3-22B). Co-transfection of variants with C-terminal fusion-tags did not result in positive BRET ratios, most likely due to mislocalization of the proteins.

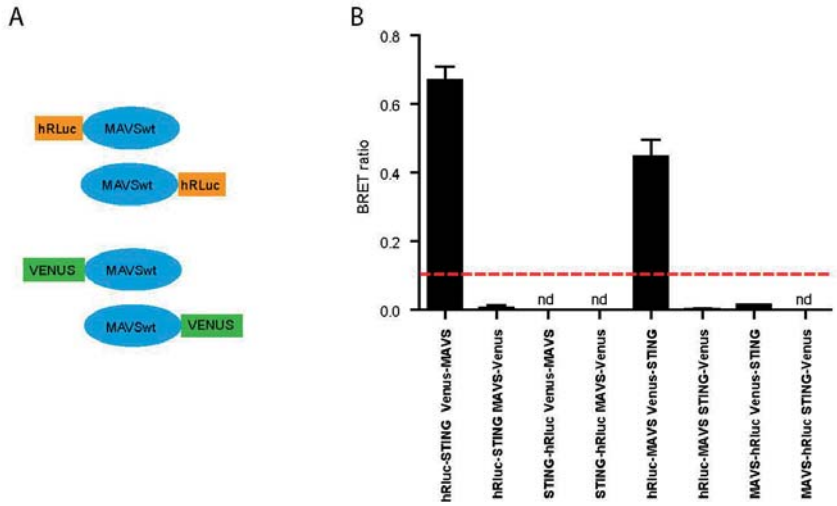

Figure 3-22 Determination of binary protein interactions of MAVSwt and STING by BRET
(A) Overview of N- and C-terminal fusion constructs for BRET donors (hRLuc) and acceptors (VENUS) using MAVSwt as an example. (B) MAVSwt and STING were co-expressed in HEK cells with varying hRLuc and VENUS fusion-tag combinations. BRET ratios above the threshold of 0.1 indicated by the dashed line are considered positive.

3.3.1.2 Screening for novel interaction partners

In order to screen for interaction partners within the peroxisomal proteome, a library of BRET vectors for 120 peroxisomal proteins was tested, established previously by the Molecular Pediatrics laboratory. We co-transfected all possible combination of the 120 constructs with combinations of our MAVS- as well as STING-constructs and determined their BRET ratios.

As a result, positive interactions between MAVSwt and seven proteins, MAVSmito and nine proteins as well as MAVSpex and nine proteins were detected. Additionally, STING was found to interact with two proteins of the peroxisomal proteome (Figure 3-23). Respective BRET ratios of the interaction partners are depicted in 8.5.

Based on gene ontology database analysis, we were able to assign several interaction partners to three functional entities, *i.e.* acyl-CoA hydrolysis, peroxisomal import and biogenesis as well as peroxisomal division. In conclusion, we were able to find 21 new interaction partners for MAVS in the peroxisomal proteome, suggesting links of MAVS to several peroxisomal functions. Additionally, two novel interaction partners for STING, acyl-CoA synthetase long-chain family member 6 (ACSL6) and D-aspartate oxidase (DDO) were identified.

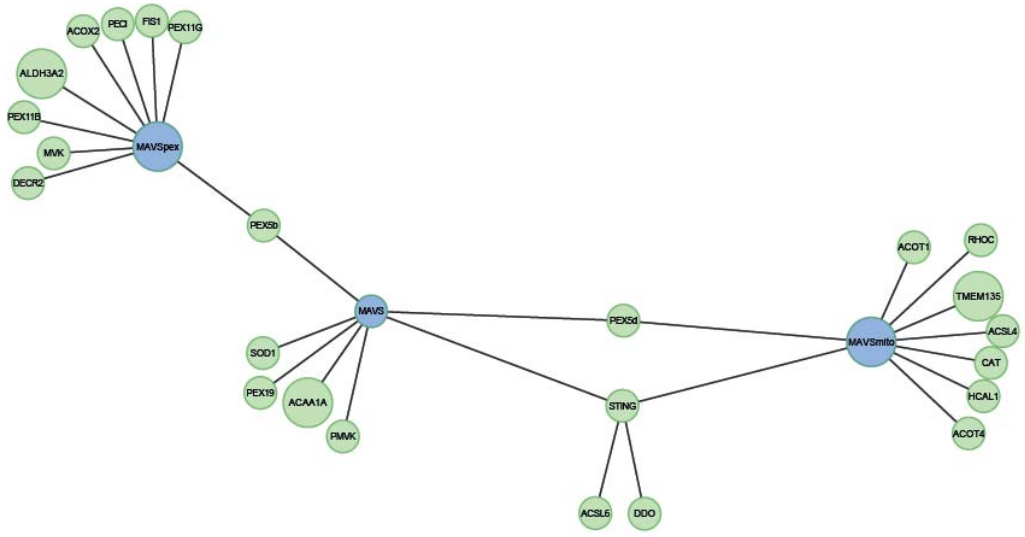

Figure 3-23 Network of positive binary protein interactions determined in a BRET-screening assay. Depicted are 24 positive PPIs detected for MAVSwt, MAVSpex, MAVSmito and STING. Each line connecting two nodes represents a positive interaction of the respective protein.

3.3.1.3 Validation of positive interactions by saturation experiments

In order to validate the results of the BRET-screen, we performed BRET saturation experiments. 11 of the previously obtained candidates were co-expressed with the MAVS variants in HEK293 cells at increasing acceptor to donor ratios. BRET ratios were measured, followed by nonlinear regression analysis. R^2 measurement for goodness of fit was performed and values of $R^2 > 0.8$ were considered as positive interactions.

Consistent with the results of the screening assay, a strong positive interaction of MAVSwt, MAVSmito and MAVSpex with STING was observed in these saturation experiments. In addition, we confirmed the interaction of Pex11G with MAVSwt and MAVSpex. Interestingly, the saturation profile of Pex11B, an isoform of Pex11G, did not give positive results for interaction with any MAVS constructs. Specific interactions were also confirmed for Pex19 and Fis1 with MAVSwt and MAVSpex and for SOD1 and ACOT1 with MAVSwt and MAVSpex, respectively. PMVK interacted with all MAVS variants, whereas positive interactions of MVK were only observed for MAVSpex. Positive interactions could not be confirmed for ACSL4 and ACSL6 (Figure 3-24A).

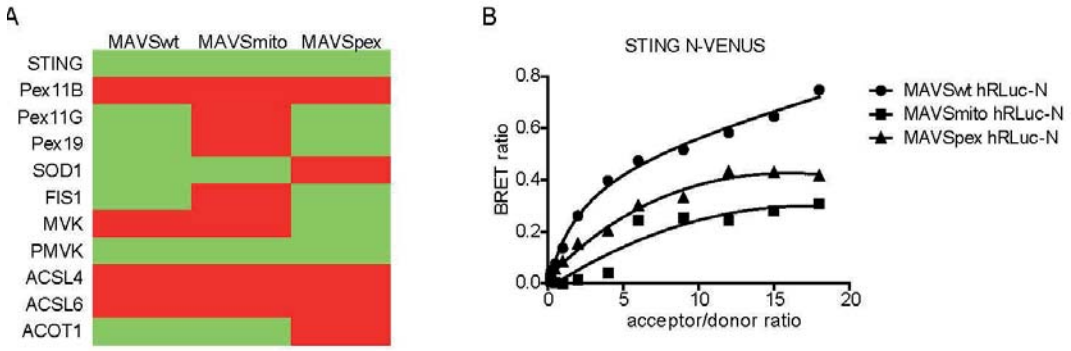

Figure 3-24 Characterization of protein interactions by saturation experiments. (A) Overview of binary interactions between MAVS localization variants and 11 candidates, tested by saturation experiments. Confirmed positive interactions based on R^2 calculations are depicted in green, negative interactions are shown in red (B) Saturation curves extracted from binary interactions of MAVSwt, MAVSmito and MAVSpex with STING.

Furthermore, we used saturation assays to analyze structural characteristics of the interaction between STING and MAVS localization variants (Figure 3-24B). After sequential increase in the ratio of VENUS-tagged MAVS over hRLuc-tagged STING, BRET ratio showed a hyperbolic behavior, characteristic for positive interactions. The BRET signal at which the saturation curve plateaus ($BRET_{max}$) is a function of the distance and orientation between the donor and acceptor within oligomeric

conformation, whereas the concentration of acceptor giving 50% of $BRET_{max}$ ($BRET_{50}$) is a reflection of the relative affinity between fusion proteins and $BRET_{50}$ values inversely correlate with the strength of affinity [161]. The interaction of STING-MAVSwt occurred with a $BRET_{max}$ value of (0.8997 SD±0.05076). Interestingly, this was almost two-fold higher compared to $BRET_{max}$ values calculated for STING-MAVSmito (0.5262 SD±0.1165) and STING-MAVSpex (0.5968 SD±0.04177), suggesting different structural conformations of the respective binding partners. Analysis of $BRET_{50}$ values revealed similar binding affinities for STING to form heterodimers with MAVSwt ($BRET_{50}$ 5.465, SD±0.8223) and MAVSpex ($BRET_{50}$ 6,339, SD±1,113) and a two-fold lower binding affinity for MAVSmito ($BRET_{50}$ 12.07, SD±5.215), indicating that STING appears to be far more likely to interact with MAVSwt and MAVSpex compared to MAVSmito.

In conclusion, we confirmed an already described interaction of MAVS and STING via BRET saturation experiments. However, a previously performed BRET-based study on MAVS revealed that the transmembrane domain of the protein has a strong influence on the capacity for homo-oligomerization of MAVS, reflected by varying $BRET_{max}$ values. Since MAVS localization variants are equipped with differing transmembrane domains and it is not known to this point, if homo-oligomerization influences the capacity of MAVS to interact with STING, it seems difficult to conclude whether differences in $BRET_{max}$ and $BRET_{50}$ are caused by variations in binding affinities due to the localization or by variations e.g. in the ability to form multimers due to the method used to design the localization variants.

3.3.2 Fibroblasts from patients with Zellweger syndrome show defects in RIG-I-like receptor signaling

A finding obtained from the previous experiments was the interaction of MAVS with a variety of peroxins. We therefore reasoned a possible impact of this protein family in MAVS-mediated antiviral signaling. Given, that MAVSwt and MAVSpex specifically interacted with PEX19, we aimed to test the impact of this protein on innate immune signaling in a natural loss-of-function mutant. We used PEX19-deficient fibroblasts, isolated from a patient with Zellweger syndrome and analyzed IFN-ß and ISG responses on mRNA level after stimulation with the synthetic ligands poly (I:C), dAdT, CpG DNA and IFN-ß for 24h compared to wild-type fibroblasts (Figure 3-25A). Strikingly, we found IFN-ß expression to be strongly reduced after poly (I:C) transfection in PEX19 deficient cells. Of note, we could exclude that this effect is due to an increased induction of cell death in PEX19-deficient cells bv poly (I:C). Transfection

of the synthetic DNA analog dAdT also resulted in diminished IFN type I responses in the absence of Pex19. Stimulation with the TLR9 ligand CpG DNA did not lead to activation of immune signaling in either of the two cell lines. This is most likely explained by the absence of functional TLR-9 in these fibroblast cell lines. Upon stimulation with IFN-ß, we could show elevated expression of the ISG RIG-I. However, this response was found to be equally strong in PEX19-deficient cells and wild-type cells, indicating that PEX19 deficient cells have no defect in the interferon-receptor mediated and JAK/STAT dependent antiviral signaling. These results implicate a direct or indirect role of PEX19 in the early antiviral signaling responses prior to the interferon receptor-mediated autocrine feed-back loop.

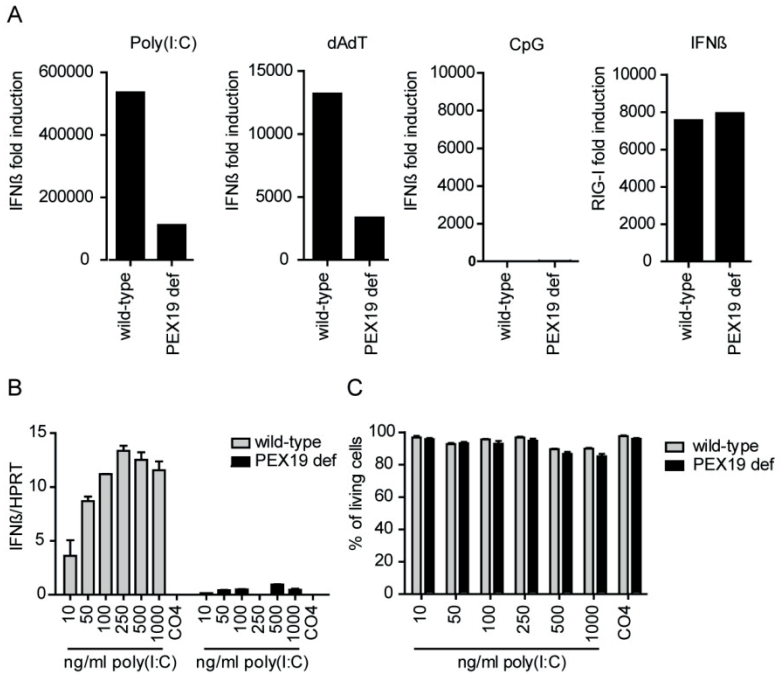

Figure 3-25 IFN type I responses of PEX19 deficient fibroblasts (A) PEX19 deficient fibroblasts and wild type fibroblasts were stimulated with 100 ng/ml poly (I:C), 1 µg/ml poly(dA:dT), 10 µg/ml CpG DNA and 1000 U/ml IFN-ß 24h prior to mRNA extraction. Expression levels of IFN-β and RIG-I were determined by qRT-PCR and are shown as fold induction levels in relation to mRNA levels of unstimulated cells. Representative data from three independent experiments are shown. (B) Wild-type fibroblasts and PEX19-deficient fibroblasts were transfected with increasing concentrations of poly (I:C). After 24 h IFN-ß RNA expression levels relative to HPRT were determined by qRT-PCR and (C) living cells were determined by flow cytometry after staining with propidium iodide. Cells negative for propidiume iodide are depicted as % of living cells. Data in B and C are shown as mean + SEM of n = 3.

To test whether the defect in immune signaling was induced directly by PEX19 or rather by the lack of functional peroxisomes, we compared antiviral signaling responses of three human fibroblasts cell lines from different patients with Zellweger

syndrome, carrying mutations in either the *PEX3*, *PEX19* or *PEX26* gene. Just like PEX19, Pex26 is a protein crucial for early peroxisomal biogenesis. Mutations in the corresponding genes lead to empty and non-functional organelles. The *PEX3* gene encodes for a peroxisomal membrane protein and its absence results in complete lack of peroxisomes. We characterized the *PEX3* mutation phenotype again and confirmed that fibroblast bearing the mutation expressed very low levels of PEX3 mRNA compared to wild type fibroblasts (Figure 3-26A). Additionally, the peroxisomal marker protein catalase showed a cytoplasmic distribution rather than a vesicular pattern (Figure 3-26B) further indicating the absence of peroxisomes in these cells.

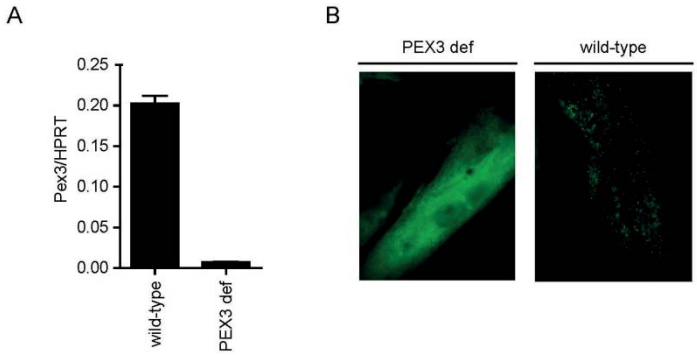

Figure 3-26 Characterization of the PEX3 mutation in human fibrobasts. (A) mRNA expression of PEX3 in PEX3-deficient fibroblasts and wild type fibroblasts was determined by qRT-PCR (B) Analysis of catalase distribution in PEX3-deficient fibroblasts and wild-type fibroblasts by immunofluorescence. Catalase expression is depicted in green.

We next tested the ability of poly (I:C) to induce an immune response in the three cell lines with mutations in PEX3, PEX19 and PEX26, respectively, and analyzed IFN-ß mRNA levels 24h post stimulation. As a result we observed a strong reduction of IFN-ß expression in all three cell lines with peroxisomal defects relative to wild type cells (Figure 3-27). These results suggest an important role of peroxisomal integrity for an adequate induction of MAVS-dependent IFN type I responses.

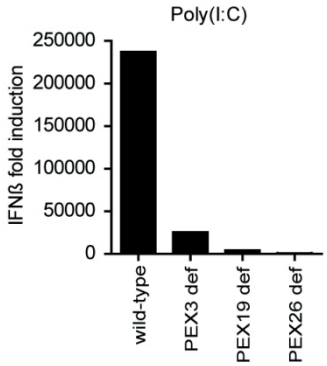

Figure 3-27 Differences in IFN responses in PEX-deficient fibroblasts. Wild-type fibroblasts and fibroblasts deficient for PEX3, PEX19 and PEX26, respectively, were stimulated with 100 ng/ml poly (I:C) 24h prior to mRNA extraction. Expression levels were determined by qRT-PCR and are shown as fold induction levels in relation to mRNA levels of unstimulated cells. Representative data from two independent experiments are shown.

4 Discussion

MAVS is localized in the outer mitochondrial membrane as well as in the membrane of peroxisomes and MAVS-mediated RIG-I-like receptor signaling not only induces antiviral and inflammatory pathways, but also triggers metabolic changes in activated cells and induces apoptosis. So far, the interplay of mitochondrial and peroxisomal organelle physiology and RIG-I-like receptor signaling processes are not fully elucidated. The aim of this work was to further analyze details of the interplay of MAVS-dependent antiviral signaling with both, mitochondria and peroxisomes. Taking different aspects of MAVS-mediated signaling into consideration, the study was divided in three parts and examined:

1) Changes in the proteome of mitochondria upon MAVS activation
2) The impact of MAVS-dependent signaling on mitochondrial respiration
3) Interaction partners of MAVS within the peroxisomal proteome and how the loss of functional peroxisomes impacts on antiviral signaling

In order to characterize changes in the mitochondrial proteome induced by RIG-I-like receptor-dependent signaling, we first established methods for efficient purification of mitochondria, for mitochondria subfractionation and for extraction of mitochondrial surface proteins in a cell culture model, the melanoma cell line 1205Lu. Using SILAC we performed quantitative proteomic analysis of three mitochondrial fractions: whole mitochondria, the isolated outer mitochondrial membrane and the proteins that can be cleaved of intact mitochondria by trypsin. In these fractions we found alterations in 155 proteins in response to stimulation with the synthetic RIG-I-like receptor ligand poly (I:C). Among these candidates, we picked 12 proteins for further evaluation of their role in antiviral signaling. Using siRNA, we performed a small-scale loss-of-function assay and found three proteins, i.e. SOD2, DDX18 and HNRNPL, to significantly alter MAVS-dependent signaling. Knock-down of HNRNPL resulted in enhanced, whereas knock-down of DDX18 and SOD2 led to decreased IFN-ß mRNA expression upon RIG-I-like receptor activation. Depletion of SOD2 additionally resulted in a decrease of the infection rate of vesicular stomatitis virus.

The mitochondrial respiration rate was assessed by determining the oxygen consumption rate (OCR) using the label-free *Seahorse XF96* assay. Transfection of poly (I:C) and 3pRNA resulted in a significant decrease of OCR after 1 h and 16 h

compared to control conditions. The decrease in OCR was thereby found to be linked to a decrease in O_2 consumption used for ATP generation but was not associated with changes in the capacity for maximal respiration, proton leakage and ROS production, MAVS-independent stimulation with untransfected poly (I:C) did not alter OCR levels and stimulation with LPS resulted in a significant decrease of OCRs after 1 h, but had no effect after 16 h. MAVS activation did not lead to increased apoptosis levels nor deregulation of respiratory chain components in our setting.

In order to identify molecular mechanisms underlying MAVS-mediated responses on peroxisomes, a large scale BRET-based screen was done to determine protein-protein interactions (PPIs) between MAVS and peroxisomal proteins. We found 25 novel putative interaction partners of MAVS in the peroxisomal proteome, of which we could confirm eight in independent saturation experiments. Three fibroblast cell lines from patients with Zellweger syndrome, carrying mutations in the genes of PEX3, PEX19 and PEX27, respectively, were used as a model system to study MAVS signaling in the absence of functional peroxisomes. All cell lines displayed a highly reduced capacity to induce IFN-ß expression in response to poly (I:C) stimulation compared to wild-type fibroblasts. The PEX19-deficient cell line additionally showed reduced IFN-ß responses upon dAdT stimulation. Stimulation with recombinant IFN-ß resulted in the induction of comparable RIG-I expression levels in wild-type and PEX19-deficient fibroblasts.

4.1 Characterization of changes in the mitochondrial proteome upon stimulation of RIG-I-like receptor signaling

MAVS-mediated signaling is a highly dynamic and transient process, which relies on protein-protein interactions and post-translational modifications of effector proteins which initiate immune and inflammatory responses. Previous studies revealed that MAVS activation is accompanied and influenced by changes in many mitochondrial functions and that mitochondrial localization of MAVS is crucial for the ability to induce antiviral responses via RLRs. These studies were performed using classical biochemical approaches with the focus on one particular protein at a time, rather than the whole mitochondrial proteome. In our study, we aimed for a comprehensive and unbiased analysis of the complete mitochondrial proteome in context of antiviral signaling through RLR activation, which had so far not been performed yet. Due to cellular heterogeneity and plasticity, the elucidation of the subcellular distribution of proteins under different conditions is a major challenge in cell biology [181]. However,

mitochondrial proteomic profiles have been generated previously in context of diseases using several animal models [182, 183].

For identification of stimulation-induced changes in the mitochondrial proteome, we chose quantitative high-resolution proteomics in combination with subcellular fractionation in an untargeted and unbiased manner using SILAC as the basis for quantification. In order to perform cellular fractionation, we established a simple and rapid method for the isolation of functionally active and structurally intact mitochondria from small tissue samples and cultured cells in collaboration with Dr. Hans Zischka [164]. In order to reduce complexity and to enrich for lower abundance components while depleting the most abundant ones, we combined the mitochondria isolation protocol with an additional MACS-based purification step and established methods to enrich for the outer mitochondrial membrane (OM) and proteins associated with or part of the mitochondrial surface via proteolytic digestion.

4.2 SILAC- based quantitative proteomic analysis

Up to now, a variety of quantitative proteomic approaches have been published to study whole cells in context of immune signaling [184]. A label-free quantitative proteomics analysis compared three conventional dendritic cell subsets of the mouse in context of innate immune signaling and revealed expression changes of over 5000 proteins. Furthermore, Luber et al. could show that components of PRR signaling pathways were differentially expressed and highlighted a not yet appreciated difference in RLR-mediated antiviral response between cDC subsets [185]. Label-free quantitative proteomics was also applied to investigate difference in surface markers between macrophage and DCs and between DCs subsets [186, 187]. Furthermore, a combination of 2-dimensional gel electrophoresis and ICAT-based quantitative analysis was performed to analyze cellular response to severe acute respiratory syndrome-associated coronavirus (SARS-CoV) infection in the Vero E6 cell line [188]. These approaches focused on changes of protein expression levels within complete cells. However, signaling cascades are usually activated and regulated by transient binding of effector molecules rather than immediate changes of expression patterns. With proteomic analyses on subcellular fractions it is possible to capture these spatiotemporal changes. To date, only few approaches have been taken to analyze protein translocation between cellular compartments in context of immune signaling. In this context, an iTRAQ-based quantitative proteomic approach was used to analyze the macrophage nuclear proteome and secretome after influenza A virus infection. This

study allowed the identification of several novel host factors contributing to innate immune responses during influenza A virus infection [189]. Furthermore, SILAC analyses have been performed quantifying changes within the nucleolar proteome of cells infected with influenza A virus [138], corona infectious bronchitis virus[190, 191] and human respiratory syncytial virus [192].

By combining mitochondria purification and subfractionation strategies with SILAC-based shotgun proteomics, the major achievement of this study is the first comprehensive quantitative analysis of mitochondria in context of RLR signaling. To date, only very few study combined SILAC as a proteomic quantification strategy with mitochondria purification to gain information on proteomic changes in response to cellular stimulation patterns. A recent report by Chen et al. performed SILAC of mitochondria after glucotoxicity in a cell culture model for β-cells [193]. Two studies have been performed in context of Parkinson's disease. Jinghua et al. investigated mitochondrial dysfunction induced by rotenone in Parkinson's disease [194]. Chan et al. analyzed parkin-induced proteasomal degradation of components of the mitochondrial proteome [195]. Wu et al. relied on 2D-electrophoresis to analyze changes in the mitochondrial proteome of A549 cells infected by swine influenza virus [196].

Our approach identified an average of 1.700 proteins per analysis and a total of more than 5000 protein groups in three independent experiments. For comparison, the study of Chen et al., which also included three independent analyses on complete mitochondria and resulted in the detection of only 1,000 protein groups [193]. The report by Jin et al. showed similar detection levels with 1722 identified proteins [194] whereas Chan et al. were able to detect 2979 proteins, indicating a higher sensitivity [195]. In contrast, a 2D-electrophoresis-based study on purified mitochondria detected only approximately 500-700 proteins per experimental condition. These results show that SILAC in principle leads to a drastically increased sensitivity of detection levels per se.

Besides a high sensitivity of detection however, it is as well crucial to maximize specificity levels by highly pure mitochondrial fractions. Different mitochondria purification strategies in combination with differing cell culture models can be an explanation for substantial variation in the detection level for proteins between studies. Mitochondria were purified by nycodenz [193], sucrose [194] and percoll gradient [195], whereas we pursued a MACS-based purification protocol. It is consequently possible that we extracted higher amounts of proteins per se due to different purification strategies. A second explanation could be a higher sensitivity in the LC-MS/MS

analysis in our study. Detection levels highly depend on e.g. the initial chromatography quality, ionization efficiency, and measurement times and can thus cause major variations [154, 197-199]. In addition, different quantification strategies were applied. High sensitivity of the measurements additionally enhances the detection level for proteins of low-abundance. Even though we can consider our detection method as sensitive, we were not able to detect proteins involved in antiviral signaling which have been reported to transfer to the mitochondrial surface upon stimulation of MAVS, *e.g.* MDA-5 or TRAF2 and TRAF3 [19, 24, 27, 46]. Taking into consideration that these translocation processes are transient, we integrated a time course into the experimental approach, thereby increasing the possibility to detect these effector molecules of antiviral signaling. The lack of detection might be due to the fact that mitochondria are highly complex organelles bearing up to 4000 proteins [69] and only a certain percentage of mitochondria per cell might get involved in the RLH signaling cascade. Binding of single proteins to only some organelles might consequently be below the detection threshold, even after mitochondrial fractionation. In addition, it is possible to lose transiently attached proteins during the purification process. The mapping of all detected proteins for their cellular compartment localization at least according to the gene ontology database revealed an enrichment of mitochondrial proteins from 20% in complete cell lysates to 50-60% in mitochondrial fractions. However, the results also indicated an average of 70% cytoplasmic and 30% nuclear proteins. Several reasons are likely to be responsible for this distribution. Firstly, up to now databases do not represent the full mitochondrial proteome yet. Secondly, even though mitochondria purification protocols have been optimized to limit the amount of proteins of other cellular compartments, it is not possible to exclude these potentially contaminating factors to 100 %. Additionally, the high sensitivity of LC-MS analysis also lowers the threshold of detection level for non-mitochondrial proteins. The SILAC-based studies of Jin et al. and Chan et al. reported 50 % [194] and approximately 35 % [195] mitochondrial-associated proteins after cell fractionation, indicating similar enrichment levels. However, Chen et al. reported only 7.5 % of the proteins to be associated with other cellular compartments [194]. While the sucrose gradient ultracentrifugation technique used for organelle isolation in their report is recognized to yield in high purity of mitochondria [200], their annotation strategy was based on a different protein data base, potentially causing differences in the calculation [194]. Low levels of contaminating proteins might be advantageous in order to decrease sample complexity and increase the detection of low-abundance proteins. However, it has to be taken into consideration that the decrease of proteins from other compartments might also reduce the possibility to detect proteins transiently translocated to the

mitochondria after stimulation. Optimally, the purification strategy should be harsh enough to diminish the contamination level of all non-associated proteins while retaining transiently associated proteins from the cytoplasm.

We considered a candidate to be regulated if 1.5-fold higher or lower intensity compared to the unstimulated condition were detected. Additionally, each experimental condition was performed twice with identical stimulation protocol but reversed SILAC conditions. We thereby provide evidence that the expression and/or subcellular localization of 155 host proteins is affected at the early phases of MAVS-dependent signaling. The cut-off level of 1.5 fold is in accordance with other studies, in which ratios of 1.3–2.5-fold have been used as cut-offs for both statistical and biological significance [131, 132, 135, 138, 139, 162, 190, 191, 193-195, 201].

However, quantification strategies are only one factor affecting the quality of measurements. Mitochondria are the most complex organelles of eukaryotic cells [38] and abundance and morphology of the organelles are highly tissue and cell type specific. Large-scale proteomic analyses have provided information on differing abundances of mitochondria between tissues, indicating that heart tissue contains more than twice the mitochondrial mass than tissue from brain regions [202]. In addition, studies have shown that morphologies, such as length and cristae composition differ substantially in mitochondria isolated from varying tissues [52]. These reports are in line with our observation on highly diverse mitochondrial ultrastructure between isolated mitochondria from primary hepatocytes and cell culture models, such as *e.g.* 1205Lu, HEK293 and HeLa [22]. Given such widely varying morphologies it is reasonable to expect that the protein composition of these organelles may vary significantly between tissues and cell types. One study revealed substantial differences in proteomic composition of mitochondria isolated from rat liver, skeletal and heart tissue [203]. Several additional proteomic studies on rat mitochondria showed only half of mitochondrial proteins to be core components found in all tissues, whereas the remaining half are distributed in a tissue-specific manner [202]. It is thus difficult to compare results from quantitative proteomic analyses on different cell types or tissues, even if they were generated utilizing similar experimental approaches.

Several strategies can be considered to further optimize the presented experimental approach. Even though SILAC can be applied in animals such as mice, it is usually limited to cell culture models, since labeling of complete animals is time and cost consuming [204, 205]. However, SILAC has recently been expanded to tissue analysis by using a mix of five SILAC labeled cell lines as internal standards for tissue proteome quantification (Super-SILAC) [136, 201]. This strategy would allow the integration of

animal models into the study, which would in turn be suited for different mitochondria isolation protocols. Super-SILAC in combination with mitochondria purification has recently been applied to distinguish differences between mitochondria isolated from synaptic and non-synaptic mice brains [206].

Secondly, application of different targeting strategies could be integrated into the study. Although mitochondria have been extensively characterized by MS proteomics, most previous studies have used mitochondrial purification, which is potentially associated with sample loss and contamination. An alternative approach was taken by Rhee et al. in 2013 [207]. The authors established a method for proteomic mapping of mitochondrial matrix and inner membrane proteins in living cells via an ascorbate peroxidase enzymatic tag (APEX), directed to the mitochondrial matrix. Upon addition of biotin-phenol and H_2O_2, APEX oxidizes phenol which in turn covalently reacts with electron-rich amino acids such as Tyr, Trp, His, and Cys, resulting in biotinylation of the corresponding proteins. The endogenous proteins were purified using streptavidin beads, digested to peptides, and identified by tandem MS. As an additional control, the authors used stable isotope labeling of experimental and control samples to distinguish between biotinylated proteins and nonspecific binders. Using this approach they were able to detect already described matrix proteins without detecting proteins from other mitochondrial compartments like the outer membrane. In addition, they could assign new proteins to the mitochondrial matrix [207]. By directing APEX specifically to the mitochondrial outer membrane, this strategy might also be considered as an approach independent of mitochondria purification.

In conclusion, the achievement of this study is a comprehensive survey of mitochondrial proteins and the quantification of regulated protein abundances in context of RLR-dependent signaling. While previous experimental approaches have mostly tested one hypothesis at a time, this study gives an example how the field of proteomics offers great potential for the global identification and characterization of mitochondrial proteins involved in innate immune signaling in a nonbiased manner. The study however also illustrates sensitivity limits of the current protocol and shows that further improvements of the method are required to consistently resolve the postulated mitochondria-associated signaling complexes by mass spectrometry.

4.2.1 Functional analysis of candidates

The most straightforward approach to investigate the function of a gene is to characterize the phenotypic changes associated with its inactivation or loss. As loss-of-function assays for the functional characterization in context of RLR-signaling and virus

infection, we chose the transient depletion of the respective candidate mRNAs by siRNA.

As type I IFNs are known to be directly induced by MAVS-signaling [35, 49, 62, 95] we evaluated the effect of knocking-down our candidates on IFN–β mRNA expression levels and included the determination of VSV titer after VSV infection as a more global screening assay of antiviral activity.

The biological importance of HNRNPL, DDX18 and SOD2 for MAVS signaling or viral infection is unknown. As the only candidate, knockdown of HNRNPL led to a significant increase of IFN-ß mRNA expression after poly (I:C) stimulation and consequently suggests an inhibitory role on RLR signaling. Previous studies on HNRNPL show a stable association with nuclear hnRNP, a complex involved in pre-mRNA processing, mRNA translocation from the nucleus to the cytoplasm, and translation [208, 209]. HNRNPL and other HNRP proteins have been identified in the cytoplasm in addition to their nuclear localization, being involved in the transportation of mRNA. HNRNPL has never been described with a mitochondrial localization. However HNRNPK, also a member of the HNRNP family, was reported to bind mitochondria-associated satellite RNA within mitochondria [210].

HNRNPL has been shown to bind to the internal ribosome entry site (IRES) of the hepatitis C virus (HCV) genomic RNA and binding of the protein correlated with the translational efficiencies of the corresponding mRNAs [211]. Interaction of HCV RNA was additionally described for HNRNPK [212]. In a second study the interaction of HNRNPL with the N-terminal region of Norwalk virus (NV) RNA was shown and the authors described a potential role in viral translation or replication processes [213]. No direct link to innate immune signaling cascades has been reported yet. However, one study provided evidence for interaction of HNRNPL and PCBP2 (also known as HNRNP E2) [209], another previously described regulator of RLR signaling [64]. Antiviral functions were however reported for HNRNPA2/B1, also a member of the HNRNP family. The protein interacts with the influenza A virus protein NS1 and inhibits viral replication. Knockdown of HNRNPA2/B1 was shown to promote transport of NS1 mRNA from the nucleus to the cytoplasm in infected cells [214]. A similar implication in antiviral signaling might be possible for HNRNPL. Due to its implication for packaging of mRNA [215], it seems possible that HNRNPL binds to cytoplasmic, potentially immuno-stimulatory RNA and shields it from detection by MDA5.

Knockdown of DDX18 led to a significant decrease of IFN-β production upon RLR activation, while it had no effect on virus replication. According to literature, DDX18 is a nucleolar protein specifically up-regulated in highly proliferating cells like embryonic

stem cells [216] with a putative role in cell cycle regulation and/or apoptosis control due to interaction with c-myc [217]. Interestingly, DDX18 also belongs to the same family of dead box helicases like RLRs, pointing towards RNA binding capacity. However, DDX18 was never described as a protein implicated in immune signaling responses. Since knock-down of DDX18 did not lead to changes in the viability of the cells, the effect on IFN-ß expression is likely to be independent from its putative implication in apoptosis and cell proliferation. The decreased expression of IFN-ß after knockdown of the protein and poly (I:C) stimulation indicates a potentially beneficial role for RLR signaling. Due to a possible implication in RNA binding, it could be speculated, that DDX18 binds to immuno-stimulatory RNA in the cytoplasm and enhances RLR-mediated antiviral signaling responses.

SOD2 was found to have a strong impact on IFN-ß mRNA expression as well as on viral replication. The enzyme is described as a mitochondrial matrix protein that efficiently converts superoxide to the less reactive hydrogen peroxide (H_2O_2) [218]. Loss of SOD2 activity can result in numerous pathological phenotypes in metabolically active tissues, particularly within the central nervous system [219]. In several previous studies a link between SOD2 and virus infection has already been reported. Even though SOD2 is not inducible by type I IFNs, the non-structural protein 1 (NS1) of human respiratory syncytial virus was found to suppress the induction of SOD2 expression in response to infection [220]. Furthermore, down-regulation of the protein led to inhibited HBV replication, accompanied by ROS generation and mitochondrial dysfunction [221] and HIV-1 Tat was also able to attenuate basal SOD2 expression [222]. Rakkola et al. were able to show the up-regulation of SOD2 after toll-like receptor activation in a proteomic screening approach of human macrophages [223]. Additionally, SOD2 has been found to be transported from mitochondria to the cytoplasm in apoptotic neuronal cells in the context of chronic prion infection. This mislocalization led to proteasomal degradation of the enzyme [224]. ROS signaling has been shown to play an important role in MAVS dependent signaling [91, 93, 150, 225, 226] and increase of intracellular ROS concentrations have been reported to enhance RLR signaling [93]. SOD2 transforms superoxide into the long-lived ROS H_2O_2 and, based on previous reports, it can be speculated that depletion of SOD2 leads to locally increased superoxide but decreased H_2O_2 levels [227-229]. It might consequently be speculated that mitochondrial H_2O_2 is required or beneficial for RLR signaling. However, if the inhibitory effect of SOD2 knock-down on IFN-ß expression in our experimental setup is linked to ROS production remains to be determined.

Additionally, knock-down of SOD2 resulted in decreased VSV infection rates. Virus infection is a process composed of several steps (attachment, membrane penetration,

virus uncoating, transcription and translation as well as assembly and release) and SOD2 might also have an implication in one of these steps. The drastically reduced susceptibility of the cell towards virus infection after depletion of SOD2 might thus be independent of the effect of SOD2 on antiviral signaling.

Taken together, we were able to observe an effect on RLR signaling for three candidates and on virus infection for one out of 12 candidate proteins. However, further studies are necessary to dissect the underlying mechanisms for these observations.

Ultimately, changes in abundance detected in the initial LC-MS analysis can have multiple explanations that need to be taken into consideration. It might be possible for the abundance of a protein to change on a cellular level (*e.g.* due to increase or decrease in degradation of the protein or transcriptional regulation). On the other hand, the abundance might not be altered on a cellular level, but instead the localization of the respective protein *e.g.* through shuttling of a protein to or from the mitochondrion. In this regard it will be interesting in future studies to analysze changes in the expression levels of the candidate proteins on RNA as well as protein levels after poly (I:C) stimulation in whole cell lysates. Another reason for altered intensities during LC-MS analysis can be changes in post-translational modification (PTM) patterns, such as phosphorylation. Protein phosphorylation is one of the most prevalent intracellular protein modifications and thus of pivotal importance in signaling pathways. Interestingly, phosphopeptides have been reported to potentially have lower ionization and detection efficiencies during MS analysis as compared with their unmodified counterparts [230]. Changes in peptide intensities in MS measurements that are misinterpreted as changes in protein abundance can in some cases be caused by changes of phosphorylation patterns of proteins instead. It might therefore be useful in the future to analyze phosphorylation patterns of the respective candidate proteins in context of RLR signaling and to perform LC-MS analysis again on the mitochondrial phosphoproteome.

4.3 Decrease of mitochondrial respiration rate after stimulation of RIG-I-like receptor signaling

In this study we have shown that transfection of poly (I:C) and 3pRNA leads to a significant decrease in basal oxygen consumption rate. Since protein levels, as a mean for cell concentration, and cell viability were unaltered after stimulation, these results suggest reduced mitochondrial respiration after activation of RLR signaling. While previous publications already described a strong contribution of mitochondrial integrity and morphology to MAVS-mediated signaling [49, 59, 86, 88, 89, 91, 93, 150, 225], we were now able to show that RLR signaling in turn also affects mitochondrial function.

A possible reason for the decreased oxygen consumption through mitochondrial respiration might be a reduced capability of mitochondria for oxidative phosphorylation in these cells. On the other hand it is possible that antiviral signaling changes the reduction of ATP production through oxidative phosphorylation in favor for energy generation through glycolysis.

Oxidative phosphorylation is characterized by a highly regulated interplay between the complexes of the electron transport chain (ETC). The ETC is the main producer of ROS in non-phagocytic cells [231] and several reports describe a positive impact of increased ROS levels on MAVS signaling [91, 93, 150, 225, 226]. Deregulation of the respiratory chain would likely result in impaired electron transfer from complex I and complex III, leading to the formation of ROS [77]. However, we did not observe significant increase of mitochondrial ROS levels upon stimulation of RLR signaling in our study, indicating that the interplay of components of the ETC might not be deregulated as a reason for the seen decreased mitochondrial respiration. In accordance with this hypothesis, we did not find deregulated protein expression levels of components of the respiratory chain. It seems to be likely that the decrease of mitochondrial oxygen consumption is not caused by the deregulation of the oxidative phosphorylation components.

Taking into consideration that the mitochondrial membrane potential ($\Delta\Psi_m$) is defined by the electrochemical gradient that forms along the mitochondrial membrane and is maintained by calcium uptake, $\Delta\Psi_m$ is also coupled to mitochondrial respiration [232] and reduced membrane potential might thus be a reason for lower respiration rates. Prior work by Koshiba et al. has shown that RLR signaling is strongly dependent on an intact $\Delta\Psi_m$, as depolarization or hyperpolarization of the inner mitochondrial membrane results in decreased antiviral responses. This effect was described to be at the level of MAVS and MAVS-dependent, since the signaling steps down-stream of MAVS, such

as phosphorylation of transcription factor IRF3 was not affected by dissipation of $\Delta\Psi_m$ [86]. Another study by Lei et al. has shown that MAVS activation on the other side results in compromised $\Delta\Psi_m$. However, the authors argue that this reduction is caused by the onset of MAVS-induced apoptosis [233]. This link is in contrast to our finding, that reduced respiration was a very early event independent of reduced cell viability. Altered respiratory rates could also be due to post-translational modifications (PTMs) of components of the ETC, such as oxidation of cysteines, [174]. However, no reports on altered PTM profiles of components of ETC are published in context of RLR signaling and this aspect thus needs further investigation.

Another explanation for reduced mitochondrial respiration might be that ATP production through oxidative phosphorylation is reduced after RLR activation in favor for energy generation through glycolysis. In favor of this hypothesis, a recent study by Pantel et al. showed, that dendritic cells (DCs) exhibited strongly reduced basal OCRs after activation of the innate immune system in mice with uncomplexed poly (I:C) in comparison to DCs of control mice [234]. Additionally, they were able to show a drastically reduced maximal mitochondrial respiration rate in their study. Analysis of extracellular acidification rates as an indicator for lactate production and glycolysis indicated a metabolic switch from oxidative phosphorylation to glycolysis after stimulation with poly (I:C). Using IFN type I receptor and HIF1α knockout-cells, respectively, they could furthermore show, that this effect is IFN-dependent and coordinated by the transcription factor HIF1α. The authors suggested that innate immune stimulation via poly (I:C) led to activation of DCs together with a metabolic switch from oxidative phosphorylation to glycolysis [234]. In accordance with these results another study also reported reduced (maximal) mitochondrial respiration in a HepG2 cell culture model upon stimulation of TLR3 with poly (I:C) [235].

While uncomplexed poly (I:C) is internalized by endocytosis and recognized by TLR3 [236], transfected poly (I:C) in the cytosplasm of the cell activates the innate immune system via MDA-5 [237]. In our experimental setup, we were able to see a strong decrease of basal OCRs in cells after poly (I:C) transfection, correlating with a strong induction of the IFN-stimulated gene IP10. But in contrast to the previous reports, stimulation with uncomplexed poly (I:C) did not affect mitochondrial respiration at any time point. However together with the fact that stimulation of 1205Lu cells with uncomplexed poly (I:C) did not result in increased expression of the IFN-stimulated IP10, these results suggest that the cells do not express TLR3 and therefore do not induce interferon upon stimulation with uncomplexed poly (I:C). Taken together, our

data might be in favor for a metabolic switch in cells upon MAVS activation, leading to reduced oxidative phosphorylation in favor for ATP generation through glycolysis.

Interestingly, we observed significantly reduced respiration rates upon LPS stimulation for 1 h, which was reversed 16 h post stimulation. A possible explanation might be that LPS is a potent inducer of nitric oxide (NO). NO can modulate mitochondrial respiration and oxygen consumption through reversible binding and inhibition at complex IV, leading to the accumulation of NADH [238]. Transient induction of NO within the cell might therefore lead to alteration in basal levels of mitochondrial respiration.

MAVS-dependent signaling is activated in vivo after viral infection. Interestingly, several reports in the last decades have also associated virus infection with dysfunction in mitochondrial respiration and increased glucose demand. For example the mitochondrial respiratory capacity was found to be decreased in neuronal cells infected with Sindbis virus. Additionally, this modulation in mitochondrial respiration was followed by a significant increase in both the uptake and utilization of glucose molecules through the glycolytic pathway [239]. By using cell lines inducibly expressing different HCV constructs, a second study showed that HCV protein expression led to severe impairment of mitochondrial oxidative phosphorylation and to a switch to non-oxidative glucose metabolism. In addition, they were able to show that HIF1α was also involved in this process [240]. Glucose uptake was furthermore found to be stimulated in cells infected with VSV and SFV [241], as well as influenza virus [242], representing viruses that are also able to induce MAVS-dependent signaling. Taken together, the results from these studies suggest that virus infection might manipulate the cellular state to match increased energy needs for expression of viral proteins. Our results however indicate that activation of MAVS-dependent signaling itself might already induce modulations in mitochondrial respiration. Activation of signal transduction and increased gene expression leads to a rapid demand in cellular energy production. Transient metabolic reprogramming of the cell might consequently not only be advantageous for the virus to ensure efficient replication, it might also be a suitable mechanism for the infected cell to adjust to increased expression of antiviral molecules. This switch might be similar to the Warburg effect described for cancer cells [169].

Taken together, the findings indicate an impact of RLR signaling on mitochondrial respiration which is not due to alterations in the respiratory chain. The novel contribution of the presented work is to reveal the impact of MAVS signaling on mitochondrial respiration, which has not been shown previously.

Further studies however are needed to evaluate how immune signaling via MAVS leads to the metabolic switch.

4.4 MAVS signaling depends on peroxisomal integrity

4.4.1 MAVS specifically interacts with a set of peroxisomal proteins

Several studies have proposed that peroxisomes are involved in viral infection based on the fact that viral proteins were targeted to peroxisomes, such as the Nef protein [124, 125] and the nonstructural influenza virus A protein 1 (NS1) [126]. Another report provided evidence for a direct link to innate immune responses by showing that the pestivirus protein N^{pro} targets peroxisomes as well as mitochondria in order to bind and inactivate IRF3 [243]. A recent report by Dixit et al. has shown a role of peroxisomes in the host responses to viral infection due to the localization of the antiviral adaptor protein MAVS on the peroxisomal membrane [50]. Even though many studies on MAVS-dependent signaling via mitochondria have been conducted, up to now no further reports on the molecular basis of MAVS signaling on peroxisomes have been published. Our study now represents a comprehensive analysis of interaction partners of MAVS in the peroxisomal proteome.

Just like mitochondria, peroxisomes are dynamic organelles which multiply by fission processes. Peroxisomal fission is partly mediated by DRP1 and FIS1, both representing GTPases also involved in mitochondrial fission [101, 108, 109]. RLR signaling via mitochondria has been shown to be strongly influenced by mitochondrial dynamics, since MAVS activation is enhanced by mitochondrial elongation through the mitochondrial fusion proteins MFN1 and OPA1, whereas mitochondrial fragmentation via DRP1 and FIS1 reduced MAVS-signaling [88, 90]. In addition, two studies provided evidence for direct interactions of MAVS with components of the fission and fusion machinery. MFN2 was found to interact with the C-terminus of MAVS, providing a mechanism of negative regulation of MAVS signaling [59]. A second study analyzed physical interactions of MAVS with MFN1/MFN2, FIS1, OPA1 and DRP1. The authors uniquely found positive interactions between MAVS and MFN1 and proposed MAVS to be a negative regulator for the protein, inhibiting MFN1-mediated mitochondrial elongation [90]. In contrast to the second report, we observed interactions of MAVSwt and MAVSpex with FIS1. We could furthermore confirm interactions of PEX11G with MAVSwt and MAVSpex as another component of the peroxisomal fission and fusion machinery. However, if the positive interaction profiles of these proteins are of functional relevance for peroxisomal morphology needs to be further analyzed. Supporting the model that peroxisomal dynamics are involved in RLR signaling, Dixit et al. showed in their initial report on peroxisomal targeting of MAVS, an elongation of peroxisomes in more than 90% of MAVSpex-expressing cells infected with reovirus T3D [50].

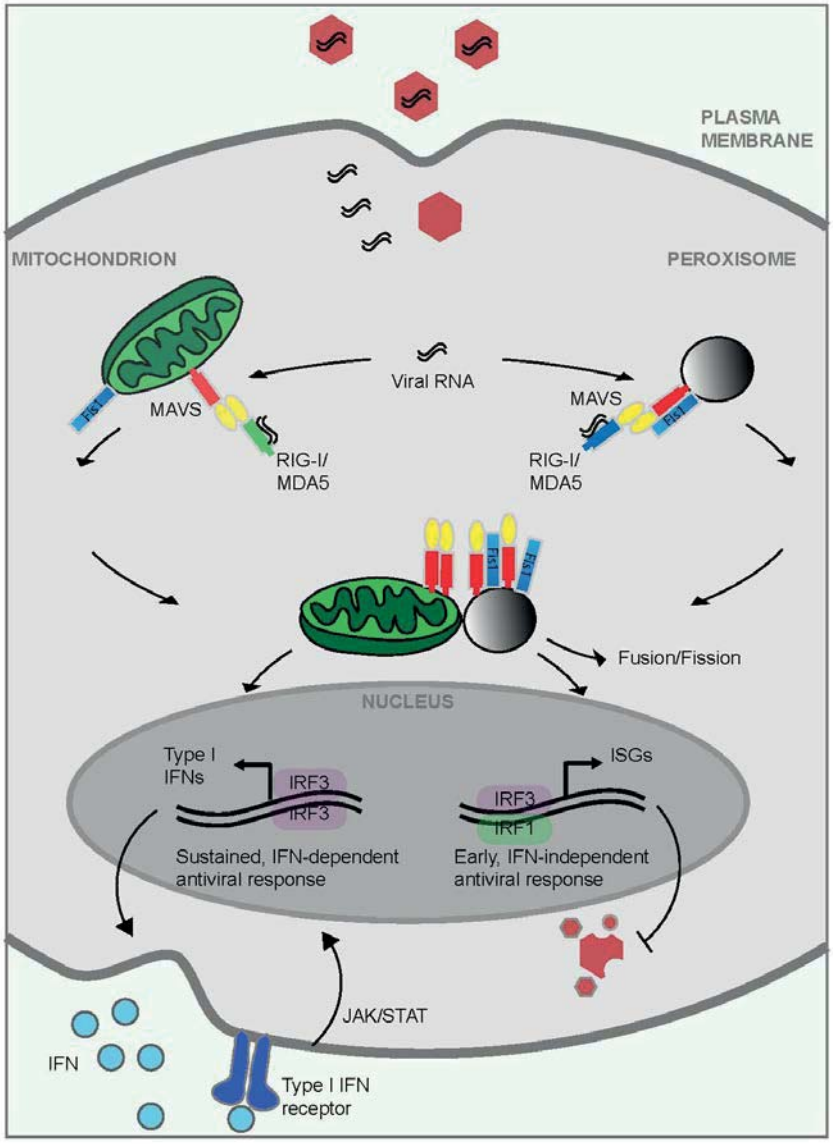

Figure 4-1 Illustrations of RLR signaling via mitochondria and peroxisomes. Upon activation of RIG-I/MDA5 by viral RNA, the receptors undergo conformational changes and bind to MAVS both on mitochondria and peroxisomes. Mitochondrial MAVS initiates antiviral signaling via activation of the transcription factor IRF3, leading to a sustained antiviral response with expression of type I IFNs and subsequent induction of ISGs via JAK/STAT signaling. Peroxisomal MAVS induces ISGs in an IFN-independent manner, induced by activation of IRF3/IRF1 heterodimers. Activation of peroxisomal MAVS results in an early and transient antiviral response, supplementing the mitochondrial antiviral response. Additionally, it might contribute to morphological changes through fusion and fission via interaction with FIS1.

Several reports characterized the peroxisomal membrane targeting sequence (mPTS) directing proteins to the peroxisomal membrane as a region bearing one or more transmembrane domains in conjunction with a short sequence, with either a cluster of basic residues or a mixture of basic and hydrophobic amino acids [244-248]. The import of peroxisomal membrane proteins is dependent on the cytosolic shuttling

protein PEX19 [249, 250]. A recent study showed PEX19 to bind to a sequence of 11 amino acids within the mPTS, which is characterized by conserved hydrophobic and positively charged amino acids [121]. The results of our screening approach gave the first hint for a positive interaction of MAVS with PEX19. After performing saturation experiments, we could reconfirm the interaction of MAVSpex and MAVSwt with PEX19. However, we were not able to detect a PEX19 binding motive in the wild-type MAVS sequence. We were not able to find this motive in FIS1 either, another protein with described localization for peroxisomes and mitochondria [108, 251]. Previous reports solely describe PEX19 as a cytosolic chaperone and import factor for peroxisomal membrane proteins [121, 122, 250, 252, 253]. The reconfirmed interaction of MAVSpex and MAVSwt with PEX19 gives now raise to a mechanistic model on how MAVS is integrated into the peroxisomal membrane. It further supports the initial finding of Dixit et al., that MAVS is specifically targeted to peroxisomes and does not get their via membrane fusion with other cellular organelles [50].

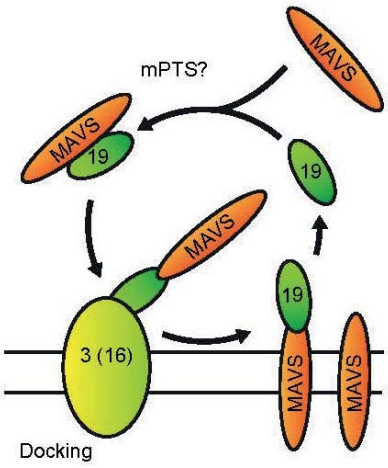

Figure 4-2 Hypothesized import mechanism for MAVS into peroxisomal membranes. Based on the results of our study, we hypothesize that MAVS is integrated into the peroxisomal membrane in a PEX19-dependent mechanism. MAVS binds to cytosolic PEX19 and might be integrated into the peroxisomal membrane in a PEX3/PEX16-dependent process. After membrane integration, PEX19 might be released again from the protein to restart the shuttling process. However, a mPTS motive in MAVS with a binding site for PEX19 has not been determined yet.

The third functional group of MAVS interacting peroxisomal proteins we detected in the initial screening approach were proteins involved in acylCoA hydrolysis. However, we could not confirm the interactions in subsequent saturation experiments. Since initial interactions were exclusively found between these proteins and the mitochondrial localization variant of MAVS, it might be possible that positive BRET signals were due to localization artifacts.

In order to genetically separate the putative mitochondrial and peroxisomal functions of the protein Dixit et al. replaced the previously defined C-terminal localization motif [49] downstream of amino acid (aa) 500 with domains that instead direct the protein to a single compartment. Using the 26 aa long localization motif of the peroxin PEX13 [252], a protein called peroxisomal protein (MAVSpex) was created. By fusion of the 98 aa long localization sequence of FIS1 [108] to the truncated C-terminus of the protein, a mitochondrial construct (MAVSmito) was generated. We took advantage of the already characterized fusion proteins and the constructs used in this study were based on the sequences used by Dixit et al. [50]. Previous studies have shown however, that interaction with several effector molecules occurs downstream of the MAVS amino acid 500 [63, 64, 254, 255]. Consequently, it has to be taken into consideration that interactions of proteins with the localization variants of MAVS might not occur at endogenous regions of MAVS, but might also take place at the C-terminal targeting sequences of PEX13 and FIS1, respectively. Additionally, fusion of these targeting sequences might also lead to different conformational characteristics of the protein, potentially altering interaction profiles. However, all proteins showing interactions with either MAVSpex or MAVSmito additionally showed a positive interaction profile with MAVSwt in saturation experiments, indicating that at least these tested interactions are mediated by MAVS-specific interactions. Another aspects for consideration is that the C-terminal targeting sequence of FIS1, which was used to locate MAVS to the peroxisome, is described to be necessary for both peroxisomal as well as mitochondrial targeting [101, 108, 251]. This is in contrast to the observation of Dixt et al., who see a purely peroxisomal localization of the MAVSpex fusion construct.

In conclusion, we were able to find 21 putative interaction partners for MAVS in the peroxisomal proteome by a BRET-based screening approach and were able to confirm 8 interactions in independent BRET saturation experiments. Our results give rise to a model how MAVS is integrated into the peroxisomal membrane and links MAVS to peroxisomal dynamics. In further studies it will be of high interest to evaluate how these interaction dynamics change in the context of acute antiviral responses.

4.4.2 Fibroblasts from patients with Zellweger syndrome show defects in RIG-I-like receptor signaling

Using fibroblasts from Zellweger syndrome patients as a system to study antiviral signaling in the absence of functional peroxisomes, we found impaired RLR signaling in these cells. For interpreting these results however, it has to be taken into consideration that peroxisomes are required for biochemical processes that are also connected to mitochondria [256]. Cells with peroxisomal impairment might consequently also display

defects in mitochondrial function and overall cell status. Given that PEX19-deficient fibroblasts are able to induce RIG-I expression comparable to wild-type cells upon stimulation with recombinant IFN-ß, these cells are nevertheless capable of normal signaling downstream of the IFN type I receptor and the induction of interferon inducible genes though the JAK/STAT pathway. However, the impact of PEX-deficiency on mitochondrial function is needed to be tested in more detail before the reduced IFN-β induction upon RLR stimulation can be really attributed to the missing peroxisomes and the peroxisomal branch of the RLR signaling.

The report of Dixit at al. implied that localization of MAVS on both peroxisomes and mitochondria is necessary to induce complete antiviral immunity. Furthermore, they proposed that full ISG and IFN expression requires signaling from both organelles, indicating that crosstalk exists between peroxisomes and mitochondria to allow the two pathways to be properly integrated [50]. In another recent study it was found that peroxisomes and mitochondria interact with one another at the MAM in hepatocytes upon viral infection. These contact sites have been proposed to form an innate immune signaling synapse, which coordinates the signaling functions of MAVS on peroxisomes and mitochondria [151].

Up to now, no studies have been performed on innate immune signaling in context of Zellweger syndrome and it is not known whether patients are more prone to viral infections. Descriptions of viral infection in context of Zellweger syndrome are missing in the literature. However, this might also be due to the very low life expectancy of these patients [115]. Furthermore, it remains unclear if RLR signaling is the only innate immune pathway that exploits peroxisomes as a signaling platform, or if other receptors signal via these organelles. Interestingly in this context, we could show that PEX19-deficient cells expressed less IFN upon stimulation with dAdT compared to wild-type cells. Cytosolic dAdT can induce IFN via two distinct pathways. Firstly, the AT-rich DNA strand can be transcribed into double-stranded RNA (dsRNA) by RNA polymerase III containing a 5'-triphosphate moiety. Activation of RIG-I by this dsRNA induces production of IFN in a MAVS-dependent pathway [34]. On the other hand, dAdT binds to and activates cyclic GMP-AMP (cGAMP) synthase (cGAS), which produces the second messenger cGAMP. cGAMP is recognized by the adaptor protein STING. Sting activation leads to the induction of a MAVS-independent signaling cascade and expression of IFN [257-260]. The possibility that peroxisomes are additionally involved in STING-dependent immune signaling can consequently not be excluded. Stimulation experiments with the second messenger cGAMP will be useful in the future to clarify this question.

In summary, using a cell culture model system deficient of functional peroxisomes we could show by that intact organelles are crucial for the induction of comprehensive MAVS-dependent signaling. Together with the finding of the BRET-based screening approach for interaction partners within the peroxisomal proteome, we hypothesize, that MAVS is integrated into the peroxisomal membrane in a *PEX19*-dependent mechanism in order to mediate antiviral signaling on these organelles.

5 Summary

Up to now, diseases caused by viral infections remain a challenging global health issue. Innate immunity is the first line of defense against viral infections. A hallmark of antiviral innate immune responses is the production of type I IFN and pro-inflammatory cytokines. These molecules not only rapidly contain viral infection by inhibiting viral replication and assembly but also play a crucial role in activating the adaptive immune system to eradicate the virus. The RIG-I-like receptors (RLRs) are essential for the detection of cytoplasmic viral RNA of many human pathogenic viruses, such as hepatitis C virus, influenza A virus, noro virus or dengue virus. The adaptor protein MAVS coordinates the signals from activated RLRs and is crucial for the initiation of the antiviral signaling cascade. Due to its location in the outer mitochondrial membrane as well as in the membrane of peroxisomes studies focusing on MAVS hypothesized that the surfaces of mitochondria and peroxisomes act as signaling platforms for antiviral immune responses and postulated an intricate bi-directional interplay between mitochondrial and peroxisomal organelle-function and antiviral signaling. In the literature, many details of the interplay between organelle function and MAVS mediated signaling have already been elucidated. [50, 59, 88, 90, 91, 150, 151, 225]. However, many aspects of the interplay between mitochondria, peroxisomes and antiviral signaling are still unknown or a matter of debate. The presented dissertation therefore focused on the identification of new players and aspects in the interplay of RLR signaling and mitochondria and peroxisomes.

In a quantitative shotgun proteomic approach, we identified 155 proteins, whose abundance changes in mitochondrial fractions in response to RLR stimulation. Using a small-scale loss-of-function analysis on 12 of these proteins, we found three candidates, i.e. SOD2, DDX18 and HNRNPL, that significantly altered MAVS-dependent IFN responses. Depletion of SOD2 additionally resulted in reduced virus titers after infection with vesicular stomatitis virus.

Secondly, we showed that mitochondrial respiration was significantly reduced after activation of MAVS signaling. The decrease was associated with a reduced O_2 consumption rate used for ATP production and not associated with an increase in mitochondrial ROS production. These results suggest that RLR signaling induces a metabolic switch in cells away from oxidative phosphorylation towards increased glycolysis.

An in-vivo BRET-based screening for protein-protein interactions resulted in the identification of 25 putative binding partners of MAVS in the peroxisomal proteome and

eight of these interactions could be confirmed in independent experiments leading to a model of Pex19-dependent integration of MAVS into the peroxisomal membrane.

Using three cell lines isolated from Zellweger syndrome patients with defects in Pex19, Pex3 and Pex27, we studied MAVS–mediated signaling in the absence of functional peroxisomes. The cells of all three patients showed drastically impaired IFN type I responses upon RLR activation, indicating that intact peroxisomes are crucial for the induction of comprehensive MAVS-dependent signaling.

In conclusion, this study identifies new proteins and aspects relevant for mitochondria and peroxisomes as signaling platforms in MAVS-mediated antiviral signaling. Furthermore it provides the first evidence for the influence of RLR signaling on the metabolic status of the cell. A better understanding of the function and activity of the signaling cascade might eventually lead to the development of novel therapeutic approaches for the management of viral diseases.

6 Zusammenfassung

Bis heute stellen virale Erkrankungen weltweit eine gravierende Herausforderung für die Gesundheit dar. Das angeborene Immunsystem und das durch dieses induzierte Typ-I Interferon sowie pro-inflammatorische Zytokine stellen hierbei den primären Verteidigungsmechanismus gegen virale Infektionen dar. Induktion dieser antiviralen Moleküle hat nicht nur die Inhibition der Virusreplikation und Virusassemblierung zur Folge, sie bewirkt im Folgenden auch die Aktivierung des adaptiven Immunsystems. Die Familie der RIG-I-like Rezeptoren (RLRs) ist hierbei von essentieller Bedeutung für die Detektion von zytoplasmatischer RNA einer Vielzahl humanpathogener Viren, unter anderem des Hepatitis C Virus, Influenza A Virus, Noro Virus und Dengue Virus. Nach Aktivierung der RLRs wird eine antivirale Signalkaskade durch das Adapterprotein MAVS weitergeleitet. MAVS konnte auf der äußeren mitochondrialen Membran sowie der peroxisomalen Membran lokalisiert werden. Durch frühere Studien manifestierte sich die Hypothese, dass die Oberflächen von Mitochondrien und Peroxisomen Signalplattformen für antivirales Signaling darstellen und in zahlreichen Arbeiten konnten bereits Hinweise für ein komplexes, wechselseitiges Zusammenspiel antiviraler Immunantworten mit der jeweiligen Organellfunktion gefunden werden [50, 59, 88, 90, 91, 150, 151, 225]. Nichts desto trotz sind viele Aspekte der Beziehung von Mitochondrien, Peroxisomen und antiviraler Signalvermittlung bisher unbekannt oder nicht vollständig aufgeklärt. Aus diesem Grund fokussiert die vorliegende Dissertation auf die weitere Charakterisierung des Zusammenspiel der RLR Signalkaskade mit Mitochondrien und Peroxisomen.

In einer quantitativen massenspektrometrischen Proteomanalyse wurden 155 Proteine identifiziert, die nach Stimulierung von RLRs Veränderungen ihrer Häufigkeit in mitochondrialen Fraktionen zeigten. In einer weiterführenden *loss-of-function* Analyse mittels siRNA von zwölf der identifizierten Proteine zeigten drei Kandidaten (SOD2, DDX18 und HNRNPL) signifikante, MAVS abhängige Veränderungen in der IFN Expression. Der *knock-down* von SOD2 resultierte zusätzlich in vermindertem Virustiter nach Infektion mit vesikulärem Stomatitis Virus. Wir konnten somit Proteine mit Einfluss auf MAVS-abhängige antivirale Signalkaskaden neu identifizieren.

Des Weiteren zeigten wir eine signifikante Reduktion der mitochondrialen Atmung nach Aktivierung der MAVS-Signalkaskade. Dieser Effekt konnte auf verminderten Sauerstoffverbrauch in Zusammenhang mit ATP Produktion zurückgeführt werden und war nicht mit erhöhter Produktion von mitochondrialen ROS assoziiert. Diese Ergebnisse deuten darauf hin, dass es durch Aktivierung von RLRs zu einer

Umstellung des zellulären Metabolismus von oxidativer Phosphorylierung zu Gunsten der Glykolyse kommt.

Eine BRET-basierte *in-vivo* Analyse von Protein-Protein Interaktionen führte zur Identifizierung von 25 Interaktionspartnern von MAVS innerhalb des peroxisomalen Proteoms. Acht dieser Verbindungen konnten in unabhängigen Experimenten bestätigt werden und die Ergebnisse führten zu der Entwicklung der Hypothese, dass MAVS in einem PEX19-abhängigen Prozess in die peroxisomale Membran integriert wird.

Mittels drei Zelllinien von Patienten mit Zellweger Syndrom mit Mutationen in PEX19, PEX3 oder PEX27 analysierten wir MAVS-abhängiges Signaling in Abwesenheit von funktionellen Peroxisomen. Die Zellen aller Patienten zeigten drastisch verminderte Typ I Interferon Antworten nach RLR Stimulierung. Dies lässt vermuten, dass intakte Peroxisomen eine essentielle Voraussetzung für die vollständige Aktivierung der MAVS-abhängigen Signalkaskade darstellen.

Zusammenfassend wurden in der vorliegenden Arbeit neuartige Proteine identifiziert, die relevant für Mitochondrien und Peroxisomen als Signalplattformen in der MAVS-abhängigen Signalkette sind. Des Weiteren konnte gezeigt werden, dass die RLR Signalkaskade den zellulären Metabolismus beeinflusst. Das neugewonnene Verständnis bezüglich Funktion und Aktivität dieser Signalkaskade könnte zur Entwicklung von neuen Therapieansätzen für Virusinfektionen genutzt werden.

7 References

1. Akira, S., S. Uematsu, and O. Takeuchi, *Pathogen recognition and innate immunity.* Cell, 2006. 124(4): p. 783-801.
2. Tang, D., et al., *PAMPs and DAMPs: signal 0s that spur autophagy and immunity.* Immunol Rev, 2012. 249(1): p. 158-75.
3. Newton, K. and V.M. Dixit, *Signaling in innate immunity and inflammation.* Cold Spring Harb Perspect Biol, 2012. 4(3).
4. Janeway, C.A., Jr., *Approaching the asymptote? Evolution and revolution in immunology.* Cold Spring Harb Symp Quant Biol, 1989. 54 Pt 1: p. 1-13.
5. Takeuchi, O. and S. Akira, *Pattern recognition receptors and inflammation.* Cell. 140(6): p. 805-20.
6. Petrilli, V., et al., *The inflammasome: a danger sensing complex triggering innate immunity.* Curr Opin Immunol, 2007. 19(6): p. 615-22.
7. Joffre, O., et al., *Inflammatory signals in dendritic cell activation and the induction of adaptive immunity.* Immunol Rev, 2009. 227(1): p. 234-47.
8. Banchereau, J. and R.M. Steinman, *Dendritic cells and the control of immunity.* Nature, 1998. 392(6673): p. 245-52.
9. Mattei, F., G. Schiavoni, and D.F. Tough, *Regulation of immune cell homeostasis by type I interferons.* Cytokine Growth Factor Rev, 2010. 21(4): p. 227-36.
10. Biron, C.A., et al., *Natural killer cells in antiviral defense: function and regulation by innate cytokines.* Annu Rev Immunol, 1999. 17: p. 189-220.
11. Le Bon, A., et al., *Type i interferons potently enhance humoral immunity and can promote isotype switching by stimulating dendritic cells in vivo.* Immunity, 2001. 14(4): p. 461-70.
12. Komai-Koma, M., et al., *TLR2 is expressed on activated T cells as a costimulatory receptor.* Proc Natl Acad Sci U S A, 2004. 101(9): p. 3029-34.
13. Caron, G., et al., *Direct stimulation of human T cells via TLR5 and TLR7/8: flagellin and R-848 up-regulate proliferation and IFN-gamma production by memory CD4+ T cells.* J Immunol, 2005. 175(3): p. 1551-7.

14. Kumar, H., T. Kawai, and S. Akira, *Pathogen recognition by the innate immune system.* Int Rev Immunol, 2010. 30(1): p. 16-34.

15. Xiao, T.S. and K.A. Fitzgerald, *The cGAS-STING pathway for DNA sensing.* Mol Cell. 51(2): p. 135-9.

16. Diebold, S.S., et al., *Innate antiviral responses by means of TLR7-mediated recognition of single-stranded RNA.* Science, 2004. 303(5663): p. 1529-31.

17. Beignon, A.S., et al., *Endocytosis of HIV-1 activates plasmacytoid dendritic cells via Toll-like receptor-viral RNA interactions.* J Clin Invest, 2005. 115(11): p. 3265-75.

18. Jurk, M., et al., *Human TLR7 or TLR8 independently confer responsiveness to the antiviral compound R-848.* Nat Immunol, 2002. 3(6): p. 499.

19. Kato, H., et al., *Differential roles of MDA5 and RIG-I helicases in the recognition of RNA viruses.* Nature, 2006. 441(7089): p. 101-5.

20. Plumet, S., et al., *Cytosolic 5'-triphosphate ended viral leader transcript of measles virus as activator of the RIG I-mediated interferon response.* PLoS One, 2007. 2(3): p. e279.

21. Saito, T., et al., *Innate immunity induced by composition-dependent RIG-I recognition of hepatitis C virus RNA.* Nature, 2008. 454(7203): p. 523-7.

22. McCartney, S.A., et al., *MDA-5 recognition of a murine norovirus.* PLoS Pathog, 2008. 4(7): p. e1000108.

23. Gitlin, L., et al., *Essential role of mda-5 in type I IFN responses to polyriboinosinic:polyribocytidylic acid and encephalomyocarditis picornavirus.* Proc Natl Acad Sci U S A, 2006. 103(22): p. 8459-64.

24. Loo, Y.M., et al., *Distinct RIG-I and MDA5 signaling by RNA viruses in innate immunity.* J Virol, 2008. 82(1): p. 335-45.

25. Kanneganti, T.D., et al., *Critical role for Cryopyrin/Nalp3 in activation of caspase-1 in response to viral infection and double-stranded RNA.* J Biol Chem, 2006. 281(48): p. 36560-8.

26. Sabbah, A., et al., *Activation of innate immune antiviral responses by Nod2.* Nat Immunol, 2009. 10(10): p. 1073-80.

27. Fujita, T., et al., *Triggering antiviral response by RIG-I-related RNA helicases.* Biochimie, 2007. 89(6-7): p. 754-60.

28. Andrejeva, J., et al., *The V proteins of paramyxoviruses bind the IFN-inducible RNA helicase, mda-5, and inhibit its activation of the IFN-beta promoter.* Proc Natl Acad Sci U S A, 2004. 101(49): p. 17264-9.

29. Renner, E.D., et al., *No indication for a defect in toll-like receptor signaling in patients with hyper-IgE syndrome.* Journal of clinical immunology, 2005. 25: p. 321-8.

30. Yoneyama, M., et al., *The RNA helicase RIG-I has an essential function in double-stranded RNA-induced innate antiviral responses.* Nat Immunol, 2004. 5(7): p. 730-7.

31. Hornung, V., et al., *5'-Triphosphate RNA is the ligand for RIG-I.* Science, 2006. 314(5801): p. 994-7.

32. Schmidt, A., et al., *5'-triphosphate RNA requires base-paired structures to activate antiviral signaling via RIG-I.* Proceedings of the National Academy of Sciences of the United States of America, 2009. 106: p. 12067-72.

33. Sumpter, R., Jr., et al., *Regulating intracellular antiviral defense and permissiveness to hepatitis C virus RNA replication through a cellular RNA helicase, RIG-I.* J Virol, 2005. 79(5): p. 2689-99.

34. Ablasser, A., et al., *RIG-I-dependent sensing of poly(dA:dT) through the induction of an RNA polymerase III-transcribed RNA intermediate.* Nat Immunol, 2009. 10(10): p. 1065-72.

35. Chiu, Y.H., J.B. Macmillan, and Z.J. Chen, *RNA polymerase III detects cytosolic DNA and induces type I interferons through the RIG-I pathway.* Cell, 2009. 138(3): p. 576-91.

36. Pichlmair, A., et al., *Activation of MDA5 requires higher-order RNA structures generated during virus infection.* J Virol, 2009. 83(20): p. 10761-9.

37. Roth-Cross, J.K., S.J. Bender, and S.R. Weiss, *Murine coronavirus mouse hepatitis virus is recognized by MDA5 and induces type I interferon in brain macrophages/microglia.* J Virol, 2008. 82(20): p. 9829-38.

38. Bruns, A.M., et al., *ATP Hydrolysis Enhances RNA Recognition and Antiviral Signal Transduction by the Innate Immune Sensor, Laboratory of Genetics and Physiology 2 (LGP2).* J Biol Chem, 2012.

39. Koyama, S., et al., *Differential role of TLR- and RLR-signaling in the immune responses to influenza A virus infection and vaccination.* J Immunol, 2007. 179(7): p. 4711-20.

40. Palm, N.W. and R. Medzhitov, *Pattern recognition receptors and control of adaptive immunity.* Immunol Rev, 2009. 227(1): p. 221-33.

41. Chakravarthy, K.V., et al., *Gold nanorod delivery of an ssRNA immune activator inhibits pandemic H1N1 influenza viral replication.* Proc Natl Acad Sci U S A, 2010. 107(22): p. 10172-7.

42. Ranjan, P., et al., *5'PPP-RNA induced RIG-I activation inhibits drug-resistant avian H5N1 as well as 1918 and 2009 pandemic influenza virus replication.* Virol J, 2010. 7: p. 102.

43. Poeck, H., et al., *5'-Triphosphate-siRNA: turning gene silencing and Rig-I activation against melanoma.* Nature medicine, 2008. 14: p. 1256-63.

44. Ellermeier, J., et al., *Therapeutic efficacy of bifunctional siRNA combining TGF-beta1 silencing with RIG-I activation in pancreatic cancer.* Cancer Res, 2013. 73(6): p. 1709-20.

45. Meng, G., et al., *Multifunctional antitumor molecule 5'-triphosphate siRNA combining glutaminase silencing and RIG-I activation.* Int J Cancer, 2014. 134(8): p. 1958-71.

46. Kawai, T., et al., *IPS-1, an adaptor triggering RIG-I- and Mda5-mediated type I interferon induction.* Nature immunology, 2005. 6: p. 981-8.

47. Xu, L.-G., et al., *VISA is an adapter protein required for virus-triggered IFN-beta signaling.* Molecular cell, 2005. 19: p. 727-40.

48. Meylan, E., et al., *Cardif is an adaptor protein in the RIG-I antiviral pathway and is targeted by hepatitis C virus.* Nature, 2005. 437: p. 1167-72.

49. Seth, R.B., et al., *Identification and characterization of MAVS, a mitochondrial antiviral signaling protein that activates NF-kappaB and IRF 3.* Cell, 2005. 122(5): p. 669-82.

50. Dixit, E., et al., *Peroxisomes Are Signaling Platforms for Antiviral Innate Immunity.* Cell, 2010. 141: p. 668-681.

51. Tang, E.D. and C.Y. Wang, *MAVS self-association mediates antiviral innate immune signaling.* J Virol, 2009. 83(8): p. 3420-8.

52. Nasr, P., et al., *Influence of cytosolic and mitochondrial Ca2+, ATP, mitochondrial membrane potential, and calpain activity on the mechanism of neuron death induced by 3-nitropropionic acid.* Neurochem Int, 2003. 43(2): p. 89-99.

53. Lad, S.P., et al., *Identification of MAVS splicing variants that interfere with RIGI/MAVS pathway signaling.* Mol Immunol, 2008. 45(8): p. 2277-87.

54. Matsuda, A., et al., *Large-scale identification and characterization of human genes that activate NF-kappaB and MAPK signaling pathways.* Oncogene, 2003. 22(21): p. 3307-18.

55. Hou, F., et al., *MAVS forms functional prion-like aggregates to activate and propagate antiviral innate immune response.* Cell, 2011. 146(3): p. 448-61.

56. Ishikawa, H. and G.N. Barber, *STING is an endoplasmic reticulum adaptor that facilitates innate immune signalling.* Nature, 2008. 455(7213): p. 674-8.

57. Zhong, B., et al., *The adaptor protein MITA links virus-sensing receptors to IRF3 transcription factor activation.* Immunity, 2008. 29(4): p. 538-50.

58. Moore, C.B., et al., *NLRX1 is a regulator of mitochondrial antiviral immunity.* Nature, 2008. 451(7178): p. 573-7.

59. Yasukawa, K., et al., *Mitofusin 2 inhibits mitochondrial antiviral signaling.* Sci Signal, 2009. 2(84): p. ra47.

60. Liu, X.Y., et al., *Tom70 mediates activation of interferon regulatory factor 3 on mitochondria.* Cell Res, 2010. 20(9): p. 994-1011.

61. Xu, L., et al., *Inhibition of RIG-I and MDA5-dependent antiviral response by gC1qR at mitochondria.* Proc Natl Acad Sci U S A, 2009. 106(5): p. 1530-5.

62. Liu, X.Y., et al., *IFN-induced TPR protein IFIT3 potentiates antiviral signaling by bridging MAVS and TBK1.* J Immunol, 2011. 187(5): p. 2559-68.

63. Jia, Y., et al., *Negative regulation of MAVS-mediated innate immune response by PSMA7.* J Immunol, 2009. 183(7): p. 4241-8.

64. You, F., et al., *PCBP2 mediates degradation of the adaptor MAVS via the HECT ubiquitin ligase AIP4.* Nat Immunol, 2009. 10(12): p. 1300-8.

65. Castanier, C., et al., *MAVS ubiquitination by the E3 ligase TRIM25 and degradation by the proteasome is involved in type I interferon production after activation of the antiviral RIG-I-like receptors.* BMC Biol, 2012. 10: p. 44.

66. Wang, Y., X. Tong, and X. Ye, *Ndfip1 negatively regulates RIG-I-dependent immune signaling by enhancing E3 ligase Smurf1-mediated MAVS degradation.* J Immunol. 189(11): p. 5304-13.

67. Song, T., et al., *c-Abl tyrosine kinase interacts with MAVS and regulates innate immune response.* FEBS Lett, 2010. 584(1): p. 33-8.

68. Gorgas, K., et al., *The fine structure of human digital arterio-venous anastomoses (Hoyer-Grosser's organs).* Anat Embryol (Berl), 1977. 150(3): p. 269-89.

69. Scorrano, L., *Keeping mitochondria in shape: a matter of life and death.* Eur J Clin Invest, 2013. 43(8): p. 886-93.

70. Giles, R.E., et al., *Maternal inheritance of human mitochondrial DNA.* Proc Natl Acad Sci U S A, 1980. 77(11): p. 6715-9.

71. Shoubridge, E.A., *The ABCs of mitochondrial transcription.* Nat Genet, 2002. 31(3): p. 227-8.

72. Campello, S. and L. Scorrano, *Mitochondrial shape changes: orchestrating cell pathophysiology.* EMBO Rep, 2010. 11(9): p. 678-84.

73. Marchi, S., S. Patergnani, and P. Pinton, *The endoplasmic reticulum-mitochondria connection: One touch, multiple functions.* Biochim Biophys Acta, 2014. 1837(4): p. 461-469.

74. Hardie, D.G., et al., *Management of cellular energy by the AMP-activated protein kinase system.* FEBS Lett, 2003. 546(1): p. 113-20.

75. Chan, D.C., *Mitochondria: dynamic organelles in disease, aging, and development.* Cell, 2006. 125(7): p. 1241-52.

76. Olanow, C.W. and W.G. Tatton, *Etiology and pathogenesis of Parkinson's disease.* Annu Rev Neurosci, 1999. 22: p. 123-44.

77. Mazat, J.P., et al., *Mitochondrial energetic metabolism-some general principles.* IUBMB Life, 2013. 65(3): p. 171-9.

78. Mailloux, R.J., X. Jin, and W.G. Willmore, *Redox regulation of mitochondrial function with emphasis on cysteine oxidation reactions.* Redox Biol, 2014. 2: p. 123-139.

79. Berridge, M.J., M.D. Bootman, and P. Lipp, *Calcium--a life and death signal.* Nature, 1998. 395(6703): p. 645-8.

80. Kroemer, G., L. Galluzzi, and C. Brenner, *Mitochondrial membrane permeabilization in cell death.* Physiol Rev, 2007. 87(1): p. 99-163.

81. Wei, M.C., et al., *Proapoptotic BAX and BAK: a requisite gateway to mitochondrial dysfunction and death.* Science, 2001. 292(5517): p. 727-30.

82. Kroemer, G. and J.C. Reed, *Mitochondrial control of cell death.* Nat Med, 2000. 6(5): p. 513-9.

83. Luo, X., et al., *Bid, a Bcl2 interacting protein, mediates cytochrome c release from mitochondria in response to activation of cell surface death receptors.* Cell, 1998. 94(4): p. 481-90.

84. Jost, P.J., et al., *XIAP discriminates between type I and type II FAS-induced apoptosis.* Nature, 2009. 460(7258): p. 1035-9.

85. Taylor, R.C., S.P. Cullen, and S.J. Martin, *Apoptosis: controlled demolition at the cellular level.* Nat Rev Mol Cell Biol, 2008. 9(3): p. 231-41.

86. Koshiba, T., et al., *Mitochondrial membrane potential is required for MAVS-mediated antiviral signaling.* Science signaling, 2011. 4: p. ra7.

87. Koshiba, T., N. Bashiruddin, and S. Kawabata, *Mitochondria and antiviral innate immunity.* International journal of biochemistry and molecular biology, 2011. 2: p. 257-62.

88. Onoguchi, K., et al., *Virus-infection or 5'ppp-RNA activates antiviral signal through redistribution of IPS-1 mediated by MFN1.* PLoS Pathog, 2010. 6(7): p. e1001012.

89. Honda, S. and S. Hirose, *Stage-specific enhanced expression of mitochondrial fusion and fission factors during spermatogenesis in rat testis.* Biochem Biophys Res Commun, 2003. 311(2): p. 424-32.

90. Castanier, C., et al., *Mitochondrial dynamics regulate the RIG-I-like receptor antiviral pathway.* EMBO reports, 2010. 11: p. 133-8.

91. Soucy-Faulkner, A., et al., *Requirement of NOX2 and reactive oxygen species for efficient RIG-I-mediated antiviral response through regulation of MAVS expression.* PLoS Pathog, 2010. 6(6): p. e1000930.

92. Arsenijevic, D., et al., *Disruption of the uncoupling protein-2 gene in mice reveals a role in immunity and reactive oxygen species production.* Nat Genet, 2000. 26(4): p. 435-9.

93. Tal, M.C., et al., *Absence of autophagy results in reactive oxygen species-dependent amplification of RLR signaling.* Proc Natl Acad Sci U S A, 2009. 106(8): p. 2770-5.

94. Besch, R., et al., *Proapoptotic signaling induced by RIG-I and MDA-5 results in type I interferon-independent apoptosis in human melanoma cells.* J Clin Invest, 2009. 119(8): p. 2399-411.

95. Li, X.D., et al., *Hepatitis C virus protease NS3/4A cleaves mitochondrial antiviral signaling protein off the mitochondria to evade innate immunity.* Proc Natl Acad Sci U S A, 2005. 102(49): p. 17717-22.

96. Grabenbauer, M., et al., *Three-dimensional ultrastructural analysis of peroxisomes in HepG2 cells. Absence of peroxisomal reticulum but evidence of close spatial association with the endoplasmic reticulum.* Cell Biochem Biophys, 2000. 32 Spring: p. 37-49.

97. Hoivik, D.J., et al., *Fibrates induce hepatic peroxisome and mitochondrial proliferation without overt evidence of cellular proliferation and oxidative stress in cynomolgus monkeys.* Carcinogenesis, 2004. 25(9): p. 1757-69.

98. van der Zand, A., et al., *Biochemically distinct vesicles from the endoplasmic reticulum fuse to form peroxisomes.* Cell, 2012. 149(2): p. 397-409.

99. Hettema, E.H. and A.M. Motley, *How peroxisomes multiply.* J Cell Sci, 2009. 122(Pt 14): p. 2331-6.

100. Koch, A., et al., *Peroxisome elongation and constriction but not fission can occur independently of dynamin-like protein 1.* J Cell Sci, 2004. 117(Pt 17): p. 3995-4006.

101. Kobayashi, S., A. Tanaka, and Y. Fujiki, *Fis1, DLP1, and Pex11p coordinately regulate peroxisome morphogenesis.* Exp Cell Res, 2007. 313(8): p. 1675-86.

102. Gandre-Babbe, S. and A.M. van der Bliek, *The novel tail-anchored membrane protein Mff controls mitochondrial and peroxisomal fission in mammalian cells.* Mol Biol Cell, 2008. 19(6): p. 2402-12.

103. Hashimoto, T., *Peroxisomal beta-oxidation enzymes.* Neurochem Res, 1999. 24(4): p. 551-63.

104. Mannaerts, G.P., P.P. Van Veldhoven, and M. Casteels, *Peroxisomal lipid degradation via beta- and alpha-oxidation in mammals.* Cell Biochem Biophys, 2000. 32 Spring: p. 73-87.

105. Reddy, J.K. and G.P. Mannaerts, *Peroxisomal lipid metabolism.* Annu Rev Nutr, 1994. 14: p. 343-70.

106. Smith, J.J. and J.D. Aitchison, *Peroxisomes take shape.* Nat Rev Mol Cell Biol, 2013. 14(12): p. 803-17.

107. Nagan, N. and R.A. Zoeller, *Plasmalogens: biosynthesis and functions.* Prog Lipid Res, 2001. 40(3): p. 199-229.

108. Koch, A., et al., *A role for Fis1 in both mitochondrial and peroxisomal fission in mammalian cells.* Mol Biol Cell, 2005. 16(11): p. 5077-86.

109. Koch, A., et al., *Dynamin-like protein 1 is involved in peroxisomal fission.* J Biol Chem, 2003. 278(10): p. 8597-605.

110. Scott, I., I.A. Sparkes, and D.C. Logan, *The missing link: inter-organellar connections in mitochondria and peroxisomes?* Trends Plant Sci, 2007. 12(9): p. 380-1; author reply 381-3.

111. Neuspiel, M., et al., *Cargo-selected transport from the mitochondria to peroxisomes is mediated by vesicular carriers.* Curr Biol, 2008. 18(2): p. 102-8.

112. Wriessnegger, T., et al., *Lipid composition of peroxisomes from the yeast Pichia pastoris grown on different carbon sources.* Biochim Biophys Acta, 2007. 1771(4): p. 455-61.

113. Waterham, H.R. and M.S. Ebberink, *Genetics and molecular basis of human peroxisome biogenesis disorders.* Biochim Biophys Acta, 2012. 1822(9): p. 1430-41.

114. Wardinsky, T.D., et al., *Rhizomelic chondrodysplasia punctata and survival beyond one year: a review of the literature and five case reports.* Clin Genet, 1990. 38(2): p. 84-93.

115. Weller, S., S.J. Gould, and D. Valle, *Peroxisome biogenesis disorders.* Annu Rev Genomics Hum Genet, 2003. 4: p. 165-211.

116. Poll-The, B.T., et al., *Infantile Refsum disease: an inherited peroxisomal disorder. Comparison with Zellweger syndrome and neonatal adrenoleukodystrophy.* Eur J Pediatr, 1987. 146(5): p. 477-83.

117. Elgersma, Y., et al., *Analysis of the carboxyl-terminal peroxisomal targeting signal 1 in a homologous context in Saccharomyces cerevisiae.* J Biol Chem, 1996. 271(42): p. 26375-82.

118. Swinkels, B.W., et al., *A novel, cleavable peroxisomal targeting signal at the amino-terminus of the rat 3-ketoacyl-CoA thiolase.* EMBO J, 1991. 10(11): p. 3255-62.

119. Braverman, N., et al., *An isoform of pex5p, the human PTS1 receptor, is required for the import of PTS2 proteins into peroxisomes.* Hum Mol Genet, 1998. 7(8): p. 1195-205.

120. Dammai, V. and S. Subramani, *The human peroxisomal targeting signal receptor, Pex5p, is translocated into the peroxisomal matrix and recycled to the cytosol.* Cell, 2001. 105(2): p. 187-96.

121. Rottensteiner, H., et al., *Peroxisomal membrane proteins contain common Pex19p-binding sites that are an integral part of their targeting signals.* Mol Biol Cell, 2004. 15(7): p. 3406-17.

122. Fujiki, Y., et al., *Import of peroxisomal membrane proteins: the interplay of Pex3p- and Pex19p-mediated interactions.* Biochim Biophys Acta, 2006. 1763(12): p. 1639-46.

123. Ahmed, M., et al., *Ability of the matrix protein of vesicular stomatitis virus to suppress beta interferon gene expression is genetically correlated with the inhibition of host RNA and protein synthesis.* J Virol, 2003. 77(8): p. 4646-57.

124. Cohen, G.B., et al., *The human thioesterase II protein binds to a site on HIV-1 Nef critical for CD4 down-regulation.* J Biol Chem, 2000. 275(30): p. 23097-105.

125. Watanabe, H., et al., *A novel acyl-CoA thioesterase enhances its enzymatic activity by direct binding with HIV Nef.* Biochem Biophys Res Commun, 1997. 238(1): p. 234-9.

126. Wolff, T., R.E. O'Neill, and P. Palese, *Interaction cloning of NS1-I, a human protein that binds to the nonstructural NS1 proteins of influenza A and B viruses.* J Virol, 1996. 70(8): p. 5363-72.

127. Meissner, F. and M. Mann, *Quantitative shotgun proteomics: considerations for a high-quality workflow in immunology.* Nat Immunol, 2014. 15(2): p. 112-7.

128. Ong, S.E. and M. Mann, *Stable isotope labeling by amino acids in cell culture for quantitative proteomics.* Methods Mol Biol, 2007. 359: p. 37-52.

129. Aebersold, R. and M. Mann, *Mass spectrometry-based proteomics.* Nature, 2003. 422: p. 198-207.

130. Ong, S.-E., *Stable Isotope Labeling by Amino Acids in Cell Culture, SILAC, as a Simple and Accurate Approach to Expression Proteomics.* Molecular & Cellular Proteomics, 2002. 1: p. 376-386.

131. Munday, D.C., et al., *Using SILAC and quantitative proteomics to investigate the interactions between viral and host proteomes.* Proteomics, 2012. 12(4-5): p. 666-72.

132. Morikawa, K., et al., *Quantitative proteomics identifies the membrane-associated peroxidase GPx8 as a cellular substrate of the hepatitis C virus NS3-4A protease.* Hepatology, 2014. 59(2): p. 423-33.

133. Xie, N., et al., *Comprehensive proteomic analysis of host cell lipid rafts modified by HBV infection.* J Proteomics, 2012. 75(3): p. 725-39.

134. Dhungana, S., et al., *Quantitative proteomics analysis of macrophage rafts reveals compartmentalized activation of the proteasome and of proteasome-mediated ERK activation in response to lipopolysaccharide.* Mol Cell Proteomics, 2009. 8(1): p. 201-13.

135. Shui, W., et al., *Quantitative proteomic profiling of host-pathogen interactions: the macrophage response to Mycobacterium tuberculosis lipids.* J Proteome Res, 2009. 8(1): p. 282-9.

136. Geiger, T., et al., *Super-SILAC mix for quantitative proteomics of human tumor tissue.* Nat Methods, 2010. 7(5): p. 383-5.

137. Shaw, P.G., et al., *Integrated proteomic and metabolic analysis of breast cancer progression.* PLoS One, 2013. 8(9): p. e76220.

138. Emmott, E., et al., *Quantitative proteomics using SILAC coupled to LC-MS/MS reveals changes in the nucleolar proteome in influenza A virus-infected cells.* J Proteome Res, 2010. 9(10): p. 5335-45.

139. Stoehr, G., et al., *A SILAC-based approach identifies substrates of caspase-dependent cleavage upon TRAIL-induced apoptosis.* Mol Cell Proteomics, 2013. 12(5): p. 1436-50.

140. Sobczyk, G.J., J. Wang, and C.J. Weijer, *SILAC-based proteomic quantification of chemoattractant-induced cytoskeleton dynamics on a second to minute timescale.* Nat Commun, 2014. 5: p. 3319.

141. Andersen, J.S., et al., *Nucleolar proteome dynamics.* Nature, 2005. 433(7021): p. 77-83.

142. Boisvert, F.M., et al., *A quantitative proteomics analysis of subcellular proteome localization and changes induced by DNA damage.* Mol Cell Proteomics, 2010. 9(3): p. 457-70.

143. Boisvert, F.M. and A.I. Lamond, *p53-Dependent subcellular proteome localization following DNA damage.* Proteomics, 2010. 10(22): p. 4087-97.

144. Wu, P. and L. Brand, *Resonance energy transfer: methods and applications.* Anal Biochem, 1994. 218(1): p. 1-13.

145. Pfleger, K.D. and K.A. Eidne, *Illuminating insights into protein-protein interactions using bioluminescence resonance energy transfer (BRET).* Nat Methods, 2006. 3(3): p. 165-74.

146. Ayoub, M.A. and K.D. Pfleger, *Recent advances in bioluminescence resonance energy transfer technologies to study GPCR heteromerization.* Curr Opin Pharmacol, 2010. 10(1): p. 44-52.

147. Xu, Y., D.W. Piston, and C.H. Johnson, *A bioluminescence resonance energy transfer (BRET) system: application to interacting circadian clock proteins.* Proc Natl Acad Sci U S A, 1999. 96(1): p. 151-6.

148. Ayoub, M.A., et al., *Monitoring of ligand-independent dimerization and ligand-induced conformational changes of melatonin receptors in living cells by bioluminescence resonance energy transfer.* J Biol Chem, 2002. 277(24): p. 21522-8.

149. Angers, S., et al., *Detection of beta 2-adrenergic receptor dimerization in living cells using bioluminescence resonance energy transfer (BRET).* Proc Natl Acad Sci U S A, 2000. 97(7): p. 3684-9.

150. Zhao, Y., et al., *COX5B regulates MAVS-mediated antiviral signaling through interaction with ATG5 and repressing ROS production.* PLoS Pathog, 2012. 8(12): p. e1003086.

151. Horner, S.M., et al., *Mitochondrial-associated endoplasmic reticulum membranes (MAM) form innate immune synapses and are targeted by hepatitis C virus.* Proc Natl Acad Sci U S A, 2011. 108(35): p. 14590-5.

152. Juhasz, I., et al., *Growth and invasion of human melanomas in human skin grafted to immunodeficient mice.* Am J Pathol, 1993. 143(2): p. 528-37.

153. Muntau, A.C., et al., *The human PEX3 gene encoding a peroxisomal assembly protein: genomic organization, positional mapping, and mutation analysis in candidate phenotypes.* Biochem Biophys Res Commun, 2000. 268(3): p. 704-10.

154. Liang, X., et al., *Single step BP/LR combined Gateway reactions.* Biotechniques, 2013. 55(5): p. 265-8.

155. Lindenbach, B.D., *Measuring HCV infectivity produced in cell culture and in vivo.* Methods Mol Biol, 2009. 510: p. 329-36.

156. Rieger, A.M., et al., *Modified annexin V/propidium iodide apoptosis assay for accurate assessment of cell death.* J Vis Exp, 2011(50).

157. Cox, J. and M. Mann, *MaxQuant enables high peptide identification rates, individualized p.p.b.-range mass accuracies and proteome-wide protein quantification.* Nature biotechnology, 2008. 26: p. 1367-72.

158. Cox, J., et al., *Andromeda: a peptide search engine integrated into the MaxQuant environment.* J Proteome Res, 2011. 10(4): p. 1794-805.

159. Ashburner, M., et al., *Gene ontology: tool for the unification of biology. The Gene Ontology Consortium.* Nat Genet, 2000. 25(1): p. 25-9.

160. Gersting, S.W., A.S. Lotz-Havla, and A.C. Muntau, *Bioluminescence resonance energy transfer: an emerging tool for the detection of protein-protein interaction in living cells.* Methods Mol Biol, 2012. 815: p. 253-63.

161. Mercier, J.F., et al., *Quantitative assessment of beta 1- and beta 2-adrenergic receptor homo- and heterodimerization by bioluminescence resonance energy transfer.* J Biol Chem, 2002. 277(47): p. 44925-31.

162. Mann, M., *Functional and quantitative proteomics using SILAC.* Nat Rev Mol Cell Biol, 2006. 7(12): p. 952-8.

163. Balch, W.E. and J.E. Rothman, *Characterization of protein transport between successive compartments of the Golgi apparatus: asymmetric properties of donor and acceptor activities in a cell-free system.* Arch Biochem Biophys, 1985. 240(1): p. 413-25.

164. Schmitt, S., et al., *A semi-automated method for isolating functionally intact mitochondria from cultured cells and tissue biopsies.* Anal Biochem, 2013. 443(1): p. 66-74.

165. Mortensen, P., et al., *MSQuant, an open source platform for mass spectrometry-based quantitative proteomics.* J Proteome Res, 2010. 9(1): p. 393-403.

166. Pindel, A. and A. Sadler, *The role of protein kinase R in the interferon response.* J Interferon Cytokine Res, 2011. 31(1): p. 59-70.

167. Tian, Y., W.L. Chen, and J.H. Ou, *Effects of interferon-alpha/beta on HBV replication determined by viral load.* PLoS Pathog, 2011. 7(7): p. e1002159.

168. Tal, M.C. and A. Iwasaki, *Mitoxosome: a mitochondrial platform for cross-talk between cellular stress and antiviral signaling.* Immunological reviews, 2011. 243: p. 215-34.

169. Warburg, O., *On the origin of cancer cells.* Science, 1956. 123(3191): p. 309-14.

170. Rolfe, D.F. and G.C. Brown, *Cellular energy utilization and molecular origin of standard metabolic rate in mammals.* Physiol Rev, 1997. 77(3): p. 731-58.

171. Brand, M.D. and D.G. Nicholls, *Assessing mitochondrial dysfunction in cells.* Biochem J, 2011. 435(2): p. 297-312.

172. Ainscow, E.K. and M.D. Brand, *Top-down control analysis of ATP turnover, glycolysis and oxidative phosphorylation in rat hepatocytes.* Eur J Biochem, 1999. 263(3): p. 671-85.

173. Balaban, R.S., *Maintenance of the metabolic homeostasis of the heart: developing a systems analysis approach.* Ann N Y Acad Sci, 2006. 1080: p. 140-53.

174. Wang, S.B., et al., *Redox regulation of mitochondrial ATP synthase.* Trends Cardiovasc Med, 2013. 23(1): p. 14-8.

175. Huttemann, M., et al., *Regulation of mitochondrial oxidative phosphorylation through cell signaling.* Biochim Biophys Acta, 2007. 1773(12): p. 1701-20.

176. Pelicano, H., et al., *Mitochondrial respiration defects in cancer cells cause activation of Akt survival pathway through a redox-mediated mechanism.* J Cell Biol, 2006. 175(6): p. 913-23.

177. Pasdois, P., et al., *Contribution of the phosphorylable complex I in the growth phase-dependent respiration of C6 glioma cells in vitro.* J Bioenerg Biomembr, 2003. 35(5): p. 439-50.

178. Bender, E. and B. Kadenbach, *The allosteric ATP-inhibition of cytochrome c oxidase activity is reversibly switched on by cAMP-dependent phosphorylation.* FEBS Lett, 2000. 466(1): p. 130-4.

179. Territo, P.R., et al., *Ca(2+) activation of heart mitochondrial oxidative phosphorylation: role of the F(0)/F(1)-ATPase.* Am J Physiol Cell Physiol, 2000. 278(2): p. C423-35.

180. Phillips, D., et al., *Regulation of oxidative phosphorylation complex activity: effects of tissue-specific metabolic stress within an allometric series and acute*

changes in workload. Am J Physiol Regul Integr Comp Physiol, 2012. 302(9): p. R1034-48.

181. Drissi, R., M.L. Dubois, and F.M. Boisvert, *Proteomics methods for subcellular proteome analysis.* FEBS J, 2013. 280(22): p. 5626-34.

182. Kim, N., et al., *Potential biomarkers for ischemic heart damage identified in mitochondrial proteins by comparative proteomics.* Proteomics, 2006. 6(4): p. 1237-49.

183. Basso, M., et al., *Proteome analysis of human substantia nigra in Parkinson's disease.* Proteomics, 2004. 4(12): p. 3943-52.

184. Lee, M.N., et al., *Identification of regulators of the innate immune response to cytosolic DNA and retroviral infection by an integrative approach.* Nat Immunol, 2013. 14(2): p. 179-85.

185. Luber, C.A., et al., *Quantitative proteomics reveals subset-specific viral recognition in dendritic cells.* Immunity, 2010. 32(2): p. 279-89.

186. Segura, T., et al., *Usefulness of multimodal MR imaging in the differential diagnosis of HaNDL and acute ischemic stroke.* BMC Neurol, 2010. 10: p. 120.

187. Becker, L., et al., *Unique proteomic signatures distinguish macrophages and dendritic cells.* PLoS One, 2012. 7(3): p. e33297.

188. Jiang, X.S., et al., *Quantitative analysis of severe acute respiratory syndrome (SARS)-associated coronavirus-infected cells using proteomic approaches: implications for cellular responses to virus infection.* Mol Cell Proteomics, 2005. 4(7): p. 902-13.

189. Lietzen, N., et al., *Quantitative subcellular proteome and secretome profiling of influenza A virus-infected human primary macrophages.* PLoS Pathog, 2011. 7(5): p. e1001340.

190. Emmott, E., et al., *Elucidation of the avian nucleolar proteome by quantitative proteomics using SILAC and changes in cells infected with the coronavirus infectious bronchitis virus.* Proteomics, 2010. 10(19): p. 3558-62.

191. Emmott, E., et al., *Quantitative proteomics using stable isotope labeling with amino acids in cell culture reveals changes in the cytoplasmic, nuclear, and nucleolar proteomes in Vero cells infected with the coronavirus infectious bronchitis virus.* Mol Cell Proteomics, 2010. 9(9): p. 1920-36.

192. Munday, D.C., et al., *Quantitative proteomic analysis of A549 cells infected with human respiratory syncytial virus.* Mol Cell Proteomics, 2010. 9(11): p. 2438-59.

193. Chen, X., et al., *Chronic high glucose induced INS-1beta cell mitochondrial dysfunction: a comparative mitochondrial proteome with SILAC.* Proteomics, 2013. 13(20): p. 3030-9.

194. Jin, J., et al., *Identification of novel proteins affected by rotenone in mitochondria of dopaminergic cells.* BMC Neurosci, 2007. 8: p. 67.

195. Chan, N.C., et al., *Broad activation of the ubiquitin-proteasome system by Parkin is critical for mitophagy.* Hum Mol Genet, 2011. 20(9): p. 1726-37.

196. Wu, X., et al., *Mitochondrial proteomic analysis of human host cells infected with H3N2 swine influenza virus.* J Proteomics, 2013. 91: p. 136-50.

197. Li, M., et al., *Increase of the LC-MS/MS sensitivity and detection limits using on-line sample preparation with large volume plasma injection.* J Chromatogr B Analyt Technol Biomed Life Sci, 2005. 825(2): p. 152-60.

198. Bi, H., et al., *Mixed-mechanism ionization to enhance sensitivity in atmospheric pressure ionization LC/MS.* J Pharm Biomed Anal, 2000. 22(5): p. 861-7.

199. Choi, B.K., D.M. Hercules, and A.I. Gusev, *Effect of liquid chromatography separation of complex matrices on liquid chromatography-tandem mass spectrometry signal suppression.* J Chromatogr A, 2001. 907(1-2): p. 337-42.

200. Wieckowski, M.R., et al., *Isolation of mitochondria-associated membranes and mitochondria from animal tissues and cells.* Nature protocols, 2009. 4: p. 1582-90.

201. Deeb, S.J., et al., *Super-SILAC allows classification of diffuse large B-cell lymphoma subtypes by their protein expression profiles.* Mol Cell Proteomics, 2012. 11(5): p. 77-89.

202. Calvo, S.E. and V.K. Mootha, *The mitochondrial proteome and human disease.* Annu Rev Genomics Hum Genet, 2010. 11: p. 25-44.

203. Forner, F., et al., *Quantitative proteomic comparison of rat mitochondria from muscle, heart, and liver.* Mol Cell Proteomics, 2006. 5(4): p. 608-19.

204. Kruger, M., et al., *SILAC mouse for quantitative proteomics uncovers kindlin-3 as an essential factor for red blood cell function.* Cell, 2008. 134(2): p. 353-64.

205. Zanivan, S., M. Krueger, and M. Mann, *In vivo quantitative proteomics: the SILAC mouse.* Methods Mol Biol, 2012. 757: p. 435-50.

206. Stauch, K.L., P.R. Purnell, and H.S. Fox, *Quantiative Proteomics of Synaptic and Non-Synaptic Mitochondria: Insights for Synaptic Mitochondrial Vulnerability.* J Proteome Res, 2014.

207. Rhee, H.W., et al., *Proteomic mapping of mitochondria in living cells via spatially restricted enzymatic tagging.* Science, 2013. 339(6125): p. 1328-31.

208. Dreyfuss, G., Y.D. Choi, and S.A. Adam, *The ribonucleoprotein structures along the pathway of mRNA formation.* Endocr Res, 1989. 15(4): p. 441-74.

209. Kim, J.H., et al., *Protein-protein interaction among hnRNPs shuttling between nucleus and cytoplasm.* J Mol Biol, 2000. 298(3): p. 395-405.

210. Klimek-Tomczak, K., et al., *Mitochondria-associated satellite I RNA binds to hnRNP K protein.* Acta Biochim Pol, 2006. 53(1): p. 169-78.

211. Hahm, B., et al., *Heterogeneous nuclear ribonucleoprotein L interacts with the 3' border of the internal ribosomal entry site of hepatitis C virus.* J Virol, 1998. 72(11): p. 8782-8.

212. Fan, B., et al., *A human proteome microarray identifies that the heterogeneous nuclear ribonucleoprotein K (hnRNP K) recognizes the 5' terminal sequence of the hepatitis C virus RNA.* Mol Cell Proteomics, 2014. 13(1): p. 84-92.

213. Gutierrez-Escolano, A.L., et al., *Interaction of cellular proteins with the 5' end of Norwalk virus genomic RNA.* J Virol, 2000. 74(18): p. 8558-62.

214. Wang, Y., J. Zhou, and Y. Du, *hnRNP A2/B1 interacts with influenza A viral protein NS1 and inhibits virus replication potentially through suppressing NS1 RNA/protein levels and NS1 mRNA nuclear export.* Virology, 2014. 449: p. 53-61.

215. Soderberg, M., F. Raffalli-Mathieu, and M.A. Lang, *Inflammation modulates the interaction of heterogeneous nuclear ribonucleoprotein (hnRNP) I/polypyrimidine tract binding protein and hnRNP L with the 3'untranslated region of the murine inducible nitric-oxide synthase mRNA.* Mol Pharmacol, 2002. 62(2): p. 423-31.

216. Zuo, C., et al., *Enriching protein-protein and functional interaction networks in human embryonic stem cells.* Int J Mol Med, 2009. 23(6): p. 811-9.

217. Fang, C.M., C. Shi, and Y.H. Xu, *Deregulated c-myc expression in quiescent CHO cells induces target gene transcription and subsequent apoptotic phenotype.* Cell Res, 1999. 9(4): p. 305-14.

218. Zelko, I.N., T.J. Mariani, and R.J. Folz, *Superoxide dismutase multigene family: a comparison of the CuZn-SOD (SOD1), Mn-SOD (SOD2), and EC-SOD (SOD3) gene structures, evolution, and expression.* Free Radic Biol Med, 2002. 33(3): p. 337-49.

219. Flynn, J.M. and S. Melov, *SOD2 in mitochondrial dysfunction and neurodegeneration.* Free Radic Biol Med, 2013. 62: p. 4-12.

220. Hastie, M.L., et al., *The human respiratory syncytial virus nonstructural protein 1 regulates type I and type II interferon pathways.* Mol Cell Proteomics, 2012. 11(5): p. 108-27.

221. Yao, D., et al., *Betulinic acid-mediated inhibitory effect on hepatitis B virus by suppression of manganese superoxide dismutase expression.* FEBS J, 2009. 276(9): p. 2599-614.

222. Marecki, J.C., et al., *HIV-1 Tat regulates the SOD2 basal promoter by altering Sp1/Sp3 binding activity.* Free Radic Biol Med, 2004. 37(6): p. 869-80.

223. Rakkola, R., S. Matikainen, and T.A. Nyman, *Proteome analysis of human macrophages reveals the upregulation of manganese-containing superoxide dismutase after toll-like receptor activation.* Proteomics, 2007. 7(3): p. 378-84.

224. Sinclair, L., et al., *Cytosolic caspases mediate mislocalised SOD2 depletion in an in vitro model of chronic prion infection.* Dis Model Mech, 2013. 6(4): p. 952-63.

225. Jamaluddin, M., et al., *Respiratory syncytial virus infection induces a reactive oxygen species-MSK1-phospho-Ser-276 RelA pathway required for cytokine expression.* J Virol, 2009. 83(20): p. 10605-15.

226. Gonzalez-Dosal, R., et al., *HSV infection induces production of ROS, which potentiate signaling from pattern recognition receptors: role for S-glutathionylation of TRAF3 and 6.* PLoS Pathog, 2011. 7(9): p. e1002250.

227. Scott, J.L., et al., *Superoxide dismutase downregulation in osteoarthritis progression and end-stage disease.* Ann Rheum Dis, 2010. 69(8): p. 1502-10.

228. Liu, C., D. Ogando, and J.A. Bonanno, *SOD2 contributes to anti-oxidative capacity in rabbit corneal endothelial cells.* Mol Vis, 2011. 17: p. 2473-81.

229. Kokoszka, J.E., et al., *Increased mitochondrial oxidative stress in the Sod2 (+/-) mouse results in the age-related decline of mitochondrial function culminating in increased apoptosis.* Proc Natl Acad Sci U S A, 2001. 98(5): p. 2278-83.

230. Steen, H., et al., *Phosphorylation analysis by mass spectrometry: myths, facts, and the consequences for qualitative and quantitative measurements.* Mol Cell Proteomics, 2006. 5(1): p. 172-81.

231. Balaban, R.S., S. Nemoto, and T. Finkel, *Mitochondria, oxidants, and aging.* Cell, 2005. 120(4): p. 483-95.

232. Zamzami, N., D. Metivier, and G. Kroemer, *Quantitation of mitochondrial transmembrane potential in cells and in isolated mitochondria.* Methods Enzymol, 2000. 322: p. 208-13.

233. Lei, Y., et al., *MAVS-mediated apoptosis and its inhibition by viral proteins.* PLoS One, 2009. 4(5): p. e5466.

234. Pantel, A., et al., *Direct type I IFN but not MDA5/TLR3 activation of dendritic cells is required for maturation and metabolic shift to glycolysis after poly IC stimulation.* PLoS Biol, 2014. 12(1): p. e1001759.

235. Djafarzadeh, S., et al., *Toll-like receptor-3-induced mitochondrial dysfunction in cultured human hepatocytes.* Mitochondrion, 2011. 11(1): p. 83-8.

236. Matsumoto, M. and T. Seya, *TLR3: interferon induction by double-stranded RNA including poly(I:C).* Adv Drug Deliv Rev, 2008. 60(7): p. 805-12.

237. Kato, H., et al., *Length-dependent recognition of double-stranded ribonucleic acids by retinoic acid-inducible gene-I and melanoma differentiation-associated gene 5.* J Exp Med, 2008. 205(7): p. 1601-10.

238. Shiva, S., *Mitochondria as metabolizers and targets of nitrite.* Nitric Oxide, 2010. 22(2): p. 64-74.

239. Silva da Costa, L., et al., *Mitochondrial bioenergetic alterations in mouse neuroblastoma cells infected with Sindbis virus: implications to viral replication and neuronal death.* PLoS One, 2012. 7(4): p. e33871.

240. Ripoli, M., et al., *Hepatitis C virus-linked mitochondrial dysfunction promotes hypoxia-inducible factor 1 alpha-mediated glycolytic adaptation.* J Virol, 2010. 84(1): p. 647-60.

241. Ritter, J.B., et al., *Metabolic effects of influenza virus infection in cultured animal cells: Intra- and extracellular metabolite profiling.* BMC Syst Biol, 2010. 4: p. 61.

242. Gray, M.A., et al., *Effect of vesicular stomatitis virus and Semliki Forest Virus on uptake of nutrients and intracellular cation concentration.* J Gen Virol, 1983. 64 (Pt 7): p. 1449-56.

243. Jefferson, M., et al., *The pestivirus N terminal protease N(pro) redistributes to mitochondria and peroxisomes suggesting new sites for regulation of IRF3 by N(pro.).* PLoS One, 2014. 9(2): p. e88838.

244. Dyer, J.M., J.A. McNew, and J.M. Goodman, *The sorting sequence of the peroxisomal integral membrane protein PMP47 is contained within a short hydrophilic loop.* J Cell Biol, 1996. 133(2): p. 269-80.

245. Baerends, R.J., et al., *A stretch of positively charged amino acids at the N terminus of Hansenula polymorpha Pex3p is involved in incorporation of the protein into the peroxisomal membrane.* J Biol Chem, 2000. 275(14): p. 9986-95.

246. Pause, B., et al., *Targeting of the 22 kDa integral peroxisomal membrane protein.* FEBS Lett, 2000. 471(1): p. 23-8.

247. Honsho, M. and Y. Fujiki, *Topogenesis of peroxisomal membrane protein requires a short, positively charged intervening-loop sequence and flanking hydrophobic segments. study using human membrane protein PMP34.* J Biol Chem, 2001. 276(12): p. 9375-82.

248. Honsho, M., T. Hiroshige, and Y. Fujiki, *The membrane biogenesis peroxin Pex16p. Topogenesis and functional roles in peroxisomal membrane assembly.* J Biol Chem, 2002. 277(46): p. 44513-24.

249. Brosius, U., T. Dehmel, and J. Gartner, *Two different targeting signals direct human peroxisomal membrane protein 22 to peroxisomes.* J Biol Chem, 2002. 277(1): p. 774-84.

250. Jones, J.M., J.C. Morrell, and S.J. Gould, *PEX19 is a predominantly cytosolic chaperone and import receptor for class 1 peroxisomal membrane proteins.* J Cell Biol, 2004. 164(1): p. 57-67.

251. Koch, J. and C. Brocard, *PEX11 proteins attract Mff and human Fis1 to coordinate peroxisomal fission.* J Cell Sci, 2012. 125(Pt 16): p. 3813-26.

252. Fransen, M., et al., *Human pex19p binds peroxisomal integral membrane proteins at regions distinct from their sorting sequences.* Mol Cell Biol, 2001. 21(13): p. 4413-24.

253. Matsuzono, Y., et al., *Human PEX19: cDNA cloning by functional complementation, mutation analysis in a patient with Zellweger syndrome, and potential role in peroxisomal membrane assembly.* Proc Natl Acad Sci U S A, 1999. 96(5): p. 2116-21.

254. Arimoto, K., et al., *Negative regulation of the RIG-I signaling by the ubiquitin ligase RNF125.* Proc Natl Acad Sci U S A, 2007. 104(18): p. 7500-5.

255. Wang, Y.Y., et al., *WDR5 is essential for assembly of the VISA-associated signaling complex and virus-triggered IRF3 and NF-kappaB activation.* Proc Natl Acad Sci U S A, 2010. 107(2): p. 815-20.

256. Wanders, R.J., *Peroxisomes, lipid metabolism, and peroxisomal disorders.* Mol Genet Metab, 2004. 83(1-2): p. 16-27.

257. Civril, F., et al., *Structural mechanism of cytosolic DNA sensing by cGAS.* Nature, 2013. 498(7454): p. 332-7.

258. Ablasser, A., et al., *cGAS produces a 2'-5'-linked cyclic dinucleotide second messenger that activates STING.* Nature, 2013. 498(7454): p. 380-4.

259. Sun, L., et al., *Cyclic GMP-AMP synthase is a cytosolic DNA sensor that activates the type I interferon pathway.* Science, 2013. 339(6121): p. 786-91.

260. Wu, J., et al., *Cyclic GMP-AMP is an endogenous second messenger in innate immune signaling by cytosolic DNA.* Science, 2013. 339(6121): p. 826-30.

261. Yuan, B., et al., *siRNA Selection Server: an automated siRNA oligonucleotide prediction server.* Nucleic Acids Res, 2004. 32(Web Server issue): p. W130-4.

8 Appendices

8.1 List of PCR primers

All primers were obtained from Metabion (Planegg, Germany).

Target Gene	Primer	Sequence (5'→ 3')
HPRT	forward	tgaccttgatttattttgcatacc
	reverse	cgagcaagacgttcagtcct
IFN-ß	forward	cgacactgttcgtgttgtca
	reverse	gaggcacaacaggagagcaa
MAVS	forward	tgtctgccagcacagtcc
	reverse	gagctgctggggtctcct
RIG-I	forward	tggaccctacctacatcctga
	reverse	ggcccttgttgtttttctca
MDA5	forward	aggcaccatgggaagtgat
	reverse	ggtaaggcctgagctggag
NLRX1	forward	gcctggtactgggcatca
	reverse	gcccaaacactcgtggaa
EIF2AK	forward	tttggacaaagcttccaacc
	reverse	cggtatgtattaagttcctccatga
HNRNPL	forward	agcggctcaagactgacaa
	reverse	gtgcgggtcatcgtagttct
DDX18	forward	gcctcccttcgttgatctg
	reverse	ctttcttggttttctggtagcc
SERPINA3	forward	actccagacagacggctttg
	reverse	attctctccattctcaactctgc
ACIN1	forward	cctgctgcctcctgacttt
	reverse	ttcagaaattgaggagctttttc
ILF3	forward	tgacatcccctgttgtcaga
	reverse	tctgcctgtccagaacgtc
EDC4	forward	aagagcctggccttccac
	reverse	cacctcatcatcatggtcactt

PCBP2	forward	tgccatctttaaggctttcg
	reverse	ttggtcatggagctgttgat
SOD2	forward	aagtaccaggaggcgttgg
	reverse	tgaacttcagtgcaggctga
SND1	forward	gggtaccatccttcatccaa
	reverse	acagcgtgcgaaaccttc
STAU1	forward	atggtatcggcaaggatgtg
	reverse	tggtccaactcagacagcaa
IGFBP2	forward	aagggtggcaagcatcac
	reverse	ctggtccagttcctgttgg
PEX3	forward	ggctgagttctttcgacc
	reverse	tccaatagtaaacggacag

8.2 List of quantitative real-time PCR primers

All primers were obtained from Metabion (Planegg, Germany). Primers and probes were designed by using the online Roche Assay Design Center

Target Gene	Primer	Sequence (5'→ 3')
HPRT	forward	tgaccttgatttattttgcatacc
	reverse	cgagcaagacgttcagtcct
IFN-ß	forward	cgacactgttcgtgttgtca
	reverse	gaggcacaacaggagagcaa
MAVS	forward	tgtctgccagcacagtcc
	reverse	gagctgctggggtctcct
RIG-I	forward	tggaccctacctacatcctga
	reverse	ggcccttgttgtttttctca
MDA5	forward	aggcaccatgggaagtgat
	reverse	ggtaaggcctgagctggag
NLRX1	forward	gcctggtactgggcatca
	reverse	gcccaaacactcgtggaa
EIF2AK	forward	tttggacaaagcttccaacc
	reverse	cggtatgtattaagttcctccatga

HNRNPL	forward	agcggctcaagactgacaa
	reverse	gtgcgggtcatcgtagttct
DDX18	forward	gcctcccttcgttgatctg
	reverse	ctttcttggttttctggtagcc
SERPINA3	forward	actccagacagacggctttg
	reverse	attctctccattctcaactctgc
ACIN1	forward	cctgctgcctcctgacttt
	reverse	ttcagaaattgaggagctttttc
ILF3	forward	tgacatcccctgttgtcaga
	reverse	tctgcctgtccagaacgtc
EDC4	forward	aagagcctggccttccac
	reverse	cacctcatcatcatggtcactt
PCBP2	forward	tgccatctttaaggctttcg
	reverse	ttggtcatggagctgttgat
SOD2	forward	aagtaccaggaggcgttgg
	reverse	tgaacttcagtgcaggctga
SND1	forward	gggtaccatccttcatccaa
	reverse	acagcgtgcgaaaccttc
STAU1	forward	atggtatcggcaaggatgtg
	reverse	tggtccaactcagacagcaa
IGFBP2	forward	aagggtggcaagcatcac
	reverse	ctggtccagttcctgttgg
PEX3	forward	ggctgagttctttcgacc
	reverse	tccaatagtaaacggacag

8.3 Small interfering RNA sequences

All small interfering RNAs were designed via the WI siRNA selection program [261] and purchased from Eurofins MWG (Ebersberg, Germany).

Target	siRNA	Sequence (5' → 3')
RIG-I	1	aucacggauuagcgacaaatt
	2	ccuuaacaaucuacugaaatt
MDA5	1	guaucguguuauuggauuatt
MAVS	1	cagaggagaaugaguauaatt
	2	ccaccuugaugccugugaatt
HNRNPL	1	guccauacccuuacacucu
	2	uaagaugaacugugaccga
EIF2AK2	1	gcagggaguaguacuuaaaua
	2	ggcaguuaguccuuuauua
DDX18	1	cgaugaaacuccugcguaa
	2	agggaaaucugaagaagaa
SERPINA3	1	gccuguacaagcaguuagu
	2	acuauaaccugaacgacau
ACIN1	1	cccacagguuccacuuuau
	2	gccagaucguucagaaaga
ILF3	1	gagcuccugugugagaaau
	2	guacgaaauacugcaaucu
EDC4	1	ggauggagaucggcauaau
	2	gauaucuucagcucaguga
PCBP2	1	atacgagagagtacagggg
	2	ggacagtatgccattccac
SOD2	1	guuccuuugacaaguuuaa
	2	gguggucauaucaaucaua
SND1	1	cagcaaaggtctagccaca
	2	ccggcuuucagaaugugaa
STAU1	1	cucccacaguuguauaaau
	2	gcugcgcugaacaucuuaa
IGFBP2	1	cagugcaagaugucucuga
	2	aaccucaaacagugcaagaug

NLRX1	1	gacccuuacaagcaucuau
	2	ccuugucucagcucuuuaa
CO4	1	gcgcuauccagcuuacgua

8.4 List of candidate proteins identified by SILAC screening

Overview of proteins regulated by >1.5 fold detected in three SILAC datasets.
SILAC ratios are depicted as log2 values, with (A) and (B) indicating reversed labeling conditions at each stimulation time point.

Complete mitochondria

30min

SILAC ratio (A)	SILAC ratio (B)	protein name	gene name
-0,7808346	-0,716683	Actin-related protein 2/3 complex subunit 4	ARPC4-TTLL3;ARPC4
-3,029146	-0,836893	Chromodomain-helicase-DNA-binding protein 4	CHD4
-0,735908	-0,785508	Actin-related protein 2/3 complex subunit 3	ARPC3
-3,167604	-0,7201909	Heterogeneous nuclear ribonucleoprotein L	HNRNPL
-3,348177	-0,7936878	Histone H1,2	HIST1H1C
-2,337302	-2,1431	Interferon-induced, double-stranded RNA-activated protein kinase	EIF2AK2
-0,7403359	-0,8946044	Src substrate cortactin	CTTN
-1,354686	-0,6100385		UGP2
-3,010541	-0,8117998	ATP-dependent RNA helicase DDX18	DDX18

90min

SILAC ratio (A)	SILAC ratio (B)	protein name	gene name
0,8225262	1,927304	Homeobox protein cut-like 1	CUX1
0,7481177	0,8406808	Lamina-associated polypeptide 2, isoform alpha;Thymopoietin;Thymopentin	TMPO

360min

SILAC ratio (A)	SILAC ratio (B)	protein name	gene name
-0,6241543	-0,7812338	Ankycorbin	RAI14
0,9138755	0,6236651	Tenascin	TNC
-0,6599962	-0,8747576	Myosin-10	MYH10
-0,8291519	-1,427928	Myosin light polypeptide 6	MYL6
0,8399596	1,082561	Alpha-1-antichymotrypsin;Alpha-1-antichymotrypsin His-Pro-less	SERPINA3
0,9981233	0,6973358	Amyloid beta A4 protein;	APP
-1,081583	-1,137962	Myosin light chain 3;Myosin light chain 1/3, skeletal muscle isoform	MYL3;MYL1

1,282796	1,312187	SPARC	SPARC
-1,076645	-1,337654	Myosin regulatory light chain 12A	MYL12A
-2,247765	-3,199013	Interferon-induced, double-stranded RNA-activated protein kinase	EIF2AK2
-0,8568678	-1,351515	Myosin-9	MYH9
-0,6473997	-1,136585	F-actin-capping protein subunit beta	CAPZB
-0,8357544	-0,9974008	F-actin-capping protein subunit alpha-1	CAPZA1
-0,6964472	-0,6655747	Unconventional myosin-Ie	MYO1E

Mitochondrial surface

30min

SILAC ratio (A)	SILAC ratio (B)	protein name	gene name
-0,745672	-0,822934	Src substrate cortactin	CTTN
-1,984617	-0,946281	Apoptotic chromatin condensation inducer in the nucleus	ACIN1
-2,905521	-0,815165	Thyroid hormone receptor-associated protein 3	THRAP3

90min

SILAC ratio (A)	SILAC ratio (B)	protein name	gene name
-1,60621	-1,48011	Gelsolin	GSN
-1,214542	-1,275663	CLIP-associating protein 1	CLASP1
-1,256425	-1,353154	Interleukin enhancer-binding factor 3	ILF3
-0,9347034	-0,811553	Supervillin	SVIL
-0,7315417	-0,790772	Galectin-1	LGALS1
-0,8571553	-0,951289	Peptidyl-prolyl cis-trans isomerase FKBP2;Peptidyl-prolyl cis-trans isomerase	FKBP2
-1,35487	-1,0202	Enhancer of mRNA-decapping protein 4	EDC4
-0,6213775	-1,144895	60S acidic ribosomal protein P2	RPLP2
0,7918558	1,10036	Poly(rC)-binding protein 2	PCBP2
0,6331987	0,8712316	Trifunctional enzyme subunit alpha, mitochondrial;Long-chain enoyl-CoA hydratase	HADHA
-0,6286977	-1,582556	Emerin	EMD
-0,6028323	-1,15043	Syntaxin-12	STX12
-1,273831	-0,909965	Protein disulfide-isomerase A3	PDIA3
0,7024803	0,9201066	Matrix-remodeling-associated protein 7	MXRA7
-1,096591	-0,918233	Superoxide dismutase [Mn], mitochondrial;Superoxide dismutase	SOD2
-0,8277941	-1,104605	Splicing factor 3A subunit 1	SF3A1
-0,7900352	-1,014784	Staphylococcal nuclease domain-containing protein 1	SND1
0,9611788	0,660589	Thioredoxin, mitochondrial	TXN2
-0,9648547	-0,767654	Sideroflexin-1	SFXN1
-1,055411	-0,641915	Tropomodulin-3	TMOD3
-0,9222921	-0,724126	LIM domain and actin-binding protein 1	LIMA1

360min

SILAC ratio (A)	SILAC ratio (B)	protein name	gene name
-0,6870096	-1,180339	Poly(rC)-binding protein 2	PCBP2
0,9017261	0,6250663	NADH-ubiquinone oxidoreductase 75 kDa subunit, mitochondrial	NDUFS1
-0,7927569	-1,418784	Apoptotic chromatin condensation inducer in the nucleus	ACIN1
-0,7076895	-0,862669	Double-stranded RNA-binding protein Staufen homolog 1	STAU1
1,252416	0,8108397	Insulin-like growth factor-binding protein 2	IGFBP2
0,913033	0,6750743	Cytochrome b-c1 complex subunit 2, mitochondrial	UQCRC2
0,6793337	0,6761111	Beta-sarcoglycan	SGCB
-0,9239882	-0,950916	Pinin	PNN

Mitochondrial surface

30 min

SILAC ratio (A)	SILAC ratio (B)	protein name	gene name
-0,7664287	-1,575992	Pre-mRNA-processing factor 19	PRPF19
-1,380524	-1,375542	Serine/arginine repetitive matrix protein 2	SRRM2
-0,7727277	-1,482090	RuvB-like 1	RUVBL1
-0,6743401	-1,819746	Chromatin target of PRMT1 protein	CHTOP
-0,7664287	-1,575992	Pre-mRNA-processing factor 19	PRPF19
-1,380524	-1,375542	Serine/arginine repetitive matrix protein 2	SRRM2
-0,7727277	-1,482090	RuvB-like 1	RUVBL1
-0,6743401	-1,819746	Chromatin target of PRMT1 protein	CHTOP
-0,6551143	-1,955916	Putative rRNA methyltransferase 3	FTSJ3
-0,7451819	-1,413265	Proline-, glutamic acid- and leucine-rich protein 1	PELP1
-0,6952621	-1,260397	ATP-dependent RNA helicase DDX51	DDX51
-0,725674	-1,567245	Exosome complex component RRP43	EXOSC8;DKFZp564C0482
-0,6316303	-1,811052	Probable ATP-dependent RNA helicase DDX27	DDX27
-0,614184	-1,798142	Probable rRNA-processing protein EBP2	EBNA1BP2
-0,623026	-0,879434	Extended synaptotagmin-1	ESYT1
-0,6710679	-1,980204	Guanine nucleotide-binding protein-like 3	GNL3
-0,6829718	-1,333524	Transcription intermediary factor 1-beta	TRIM28
-0,7398723	-1,347425	Splicing factor 3B subunit 2	SF3B2
-0,7187547	-1,236379	Ribosome biogenesis protein BOP1	BOP1;KM-PA-2
-0,7995152	-1,842765	Nucleolar and coiled-body phosphoprotein 1	NOLC1
-0,6050752	-1,187210	Ribosome biogenesis regulatory protein homolog	RRS1
-0,7753842	-1,484477	WD repeat-containing protein 43	WDR43
-0,7363559	-1,465772	Splicing factor 3B subunit 3	SF3B3
-0,7068248	-1,682907	Splicing factor 3A subunit 1	SF3A1
-0,678685	-1,550847	RNA-binding protein Raly	RALY
-0,6697434	-1,665895	CCAAT/enhancer-binding protein zeta	CEBPZ
-0,6581228	-1,553122	Heterogeneous nuclear ribonucleoprotein A1;	HNRNPA1;HNRNPA1L2

-0,9677635	-1,631108	ATP-dependent RNA helicase DDX24	DDX24
-0,6447377	-1,640880	Pre-mRNA 3-end-processing factor FIP1	FIP1L1
-0,862618	-1,354821	U4/U6,U5 tri-snRNP-associated protein 1	SART1
-0,6300152	-1,621943	U3 small nucleolar RNA-interacting protein 2	RRP9
-0,6700964	-1,357427	Splicing factor 3B subunit 1	SF3B1
-0,8962162	-1,711642	U5 small nuclear ribonucleoprotein 200 kDa helicase	SNRNP200
-0,6306507	-1,403469	Surfeit locus protein 6	SURF6
-0,6435758	-1,799927	Ribosomal L1 domain-containing protein 1	RSL1D1
-0,6571951	-1,331697	Metastasis-associated protein MTA2	MTA2;DKFZp686F2281
-0,7729932	-1,996672	Ribosome biogenesis protein NSA2 homolog	NSA2
-0,6044677	-0,697453	Fructose-bisphosphate aldolase A	ALDOA
-1,1647584	-0,886173	Non-histone chromosomal protein HMG-17;	HMGN2;HMGN3
-0,751781	-1,461518	Histone H1,0	H1F0
-0,6965562	-0,670355	Medium-chain specific acyl-CoA dehydrogenase, mitochondrial	ACADM
-0,6425188	-1,512651	Splicing factor U2AF 65 kDa subunit	U2AF2
-0,7085825	-0,639079	Succinyl-CoA ligase [ADP/GDP-forming] subunit alpha, mitochondrial	SUCLG1
-0,601249	-1,581076	Eukaryotic translation initiation factor 6	EIF6
-0,8474847	-1,098876	Small nuclear ribonucleoprotein Sm D1	SNRPD1
-0,6732426	-1,277867	60S ribosomal protein L10a	RPL10A
-0,8628803	-1,564602	Heterogeneous nuclear ribonucleoprotein U	HNRNPU
-0,6542583	-0,983989	60S ribosomal protein L18	RPL18
-0,6028322	-1,460264	ATP-dependent RNA helicase A	DHX9
-0,66701	-1,674355	Transducin beta-like protein 3	TBL3
-0,7604202	-1,262125	Interleukin enhancer-binding factor 2	ILF2
-0,8980346	-1,424109	Heterogeneous nuclear ribonucleoproteins C1/C2	HNRNPC
-0,6579127	-1,486613	U3 small nucleolar RNA-associated protein 18 homolog	UTP18
-0,6448938	-1,702057	116 kDa U5 small nuclear ribonucleoprotein component	EFTUD2
-0,9710223	-2,277061	RNA-binding protein FUS	FUS
-0,7883955	-1,491449	Heterogeneous nuclear ribonucleoprotein D0	HNRNPD
-0,7574159	-1,689842	Nucleolar GTP-binding protein 1	GTPBP4
-0,8028021	-1,627687	DNA topoisomerase 2-alpha;DNA topoisomerase 2	TOP2A
-0,7956579	-1,823847	Probable ATP-dependent RNA helicase DDX56	DDX56
-0,652391	-1,203987	H/ACA ribonucleoprotein complex subunit 2	NHP2
-0,7827339	-1,185289	Double-stranded RNA-specific adenosine deaminase	ADAR
-0,7169661	-0,823066	Transmembrane protein 109	TMEM109
-0,7195036	-1,435553	THO complex subunit 4	ALYREF
-0,7892582	-1,439969	RRP12-like protein	RRP12
-0,6376251	-1,556490	U3 small nucleolar RNA-associated protein 14 homolog A	UTP14A
-0,6697434	-1,665895	CCAAT/enhancer-binding protein zeta	CEBPZ
-0,6581228	-1,553122	Heterogeneous nuclear ribonucleoprotein A1	HNRNPA1;HNRNPA1L2
-0,9677635	-1,631108	ATP-dependent RNA helicase DDX24	DDX24
-0,6447377	-1,640880	Pre-mRNA 3-end-processing factor FIP1	FIP1L1
-0,862618	-1,354821	U4/U6,U5 tri-snRNP-associated protein 1	SART1
-0,6300152	-1,621943	U3 small nucleolar RNA-interacting protein 2	RRP9
-0,6700964	-1,357427	Splicing factor 3B subunit 1	SF3B1
-0,8962162	-1,711642	U5 small nuclear ribonucleoprotein 200 kDa helicase	SNRNP200

-0,6306507	-1,403469	Surfeit locus protein 6	SURF6
-0,6435758	-1,799927	Ribosomal L1 domain-containing protein 1	RSL1D1
-0,6571951	-1,331697	Metastasis-associated protein MTA2	MTA2;DKFZp686F2281
-0,7729932	-1,996672	Ribosome biogenesis protein NSA2 homolog	NSA2
-0,6044677	-0,697453	Fructose-bisphosphate aldolase A	ALDOA
-1,1647584	-0,886173	Non-histone chromosomal protein HMG-17	HMGN2;HMGN3
-0,751781	-1,461518	Histone H1,0	H1F0
-0,6965562	-0,670355	Medium-chain specific acyl-CoA dehydrogenase, mitochondrial	ACADM
-0,6425188	-1,512651	Splicing factor U2AF 65 kDa subunit	U2AF2
-0,7085825	-0,639079	Succinyl-CoA ligase [ADP/GDP-forming] subunit alpha, mitochondrial	SUCLG1
-0,601249	-1,581076	Eukaryotic translation initiation factor 6	EIF6
-0,8474847	-1,098876	Small nuclear ribonucleoprotein Sm D1	SNRPD1
-0,6732426	-1,277867	60S ribosomal protein L10a	RPL10A
-0,8628803	-1,564602	Heterogeneous nuclear ribonucleoprotein U	HNRNPU
-0,6542583	-0,983989	60S ribosomal protein L18	RPL18
-0,6028322	-1,460264	ATP-dependent RNA helicase A	DHX9
-0,66701	-1,674355	Transducin beta-like protein 3	TBL3
-0,7604202	-1,262125	Interleukin enhancer-binding factor 2	ILF2

90 min

SILAC ratio (A)	SILAC ratio (B)	protein name	gene name
0,99964	0,786973	Nucleoporin p54	NUP54
3,070634	0,6773325	Epididymal secretory protein E1	NPC2

360min

SILAC ratio (A)	SILAC ratio (B)	protein name	gene name
0,99964	0,786973	Nucleoporin p54	NUP54
-0,950141	-1,580105	Zinc finger CCCH-type antiviral protein 1	ZC3HAV1
-1,212292	-1,572638	Heat shock protein beta-1	HSPB1
-0,620465	-0,892330	Aspartate--tRNA ligase, cytoplasmic	DARS;DKFZp781B11202
-0,967615	-0,769541	Metalloproteinase inhibitor 3	TIMP3
-0,6791706	-0,751765	Cytoplasmic dynein 1 heavy chain 1	DYNC1H1

8.5 List of protein interactions detected by BRET screening

Overview of luciferase and VENUS signals detected in BRET screening assay

Protein1	Protein2	Luc1	Luc2	Venus1	Venus2	$BRET_{mean}$
MAVS	PEX5d	23010	25540	7500	8655	0.0404
MAVS	PEX19	9281	10326	3084	3542	0.0466
MAVS	PEX5b	14900	13558	4927	4521	0.0447
MAVSpex	PEX5b	10546	12275	3477	4092	0.0458
MAVS	STING	10441	14643	7293	9516	0.3869
MAVSmito	STING	12401	15157	4519	5737	0.0797
MAVS	SOD1	22669	14578	7684	4905	0.0457
MAVSpex	DECR2	6219	6771	2133	2223	0.044
MAVSpex	MVK	11731	11211	3725	3687	0.0403
MAVSpex	PEX11B	8508	10256	2907	3366	0.0464
MAVSpex	ACOX2	8349	7926	2675	2822	0.0526
STING	DDO	8758	9119	2922	2720	0.0272
MAVS	PEX19	12874	18192	4521	6252	0.0623
MAVSmito	PEX5d	9143	8187	3328	2868	0.0675
MAVSmito	ACSL4	7788	8272	2369	2687	0.0323
MAVS	ACAA1A	15865	17551	4844	5678	0.0301
MAVSmito	HCAL1	14516	14015	4539	4670	0.0352
MAVSpex	PECI	19890	22383	6277	6852	0.0326
STING	ACSL6	4690	4503	1417	1591	0.0488
MAVSpex	FIS1	14438	17994	4775	6175	0.0363
MAVSpex	ALDH3A2	18586	24483	6097	7332	0.036
MAVSpex	PEX11G	17309	19034	5716	6058	0.0354
MAVSmito	RHOC	8389	5715	2652	1940	0.0509
MAVSmito	CAT	7235	8907	2377	2772	0.0345
MAVSmito	ACOT1	16558	19768	4949	6163	0.0401
MAVS	PMVK	23239	25848	7138	7928	0.0417
MAVSmito	TMEM135	13443	14959	3865	4700	0.0356
MAVSmito	ACOT4	13009	11003	4089	3654	0.0369

8.6 Abbreviations

ACIN1	Apoptotic Chromatin Condensation Inducer 1
APEX	ascorbate peroxidase enzymatic tag
BRET	Bioluminescence resonance transfer
BSA	Bovine serum albumin
CARD	Caspase activation and recruitment domain
Cardif	CARD adapter inducing interferon-beta
Cat	Catalase
CpG	Oligonucleotide with cytosine-(phosphate)-guanine motifs
CytC	Cytochrome C
DAPI	4',6-Diamidin-2'-phenylindoldihydrochlorid
DDX18	DEAD box protein-18
DMEM	Dulbecco's modified Eagle's medium
DMSO	Dimethyl sulfoxid
DNA	Deoxyribonucleic acid
ds	Double-stranded
e.g.	exempli gratia
EDC4	Enhancer of mRNA decapping 4
EIF2AK	eIF2alpha kinase
ELISA	Enzyme-linkedimmunosorbent assay
FACS	Fluorescent activated cell sorting
FCCP	Carbonyl cyanide-*p*-trifluoromethoxyphenylhydrazone
FCS	Fetal calf serum
FITC	Fluorescine
HCV	Hepatitis C virus
HNRNPL	Heterogeneous ribonucleoprotein-L
HSP60	Heat shock protein 60
Huh-7	Human hepatoma cell line-7
i.e.	id est
IFN	Interferon
IGFBP2	Insulin-like growth factor binding protein 2
IL6	Interleukine 6
ILF3	Interleukin enhancer binding factor 3
IP10	Interferon-gamma induced protein 10 kDa
IPS-1	Interferon-beta promoter stimulator 1
IRF3	IFN regulatory factor 3

ISG	Interferon-stimulated gene
JAK	Janus kinase
kDa	Kilo Dalton
LAMP	Lysosome associated membrane protein
LGP2	Laboratory of genetics and physiology-2
LPS	Lipopolysaccharide
MACS	Magnetic-activated cell sorting
MAM	Mitochondria-associated membrane
MAVS	Mitochondrial antiviral signaling protein
MDA5	Melanoma differentiation-associated gene 5
min	Minute
MOI	Multiplicity of infection
mRNA	Messenger RNA
nd	Not determined
NFκB	Nuclear factor kappa B
NLRX1	NOD-like receptor family member X1
ns	Not significant
NV	Norwalk virus
OCR	Oxygen consumption rate
OM	Outer mitochondrial membrane
p.i.	Post-infection
PAMP	Pathogen-associated molecular pattern
PBCP2	Poly(rC)-binding protein 2
PBS	Phosphate-buffered saline
PCR	Polymerase chain reaction
PEX	Peroxin
PI	Propidium iodide
PMP70	Peroxisome marker protein 70
PRR	Pattern recognition receptor
PTPC	Permeability transition pore complex
qRT-PCR	Quantitative real-time polymerase chain reaction
RIG-I	Retinoic acid-inducible gene I
RLR	RIG-I-like receptor
RNA	Ribonucleic acid
RT	Room temperature
SDS-PAGE	Sodium dodecyl sulfate-polyacrylamide gel electrophoresis
sec	Second

SERPINA3	Serpin peptidase inhibitor clade A, member 3
SILAC	Stable isotope labeling of amino acids in cell culture
SOD2	Super oxide dismutase-2
ss	Single-stranded
STAT	Signal transducer and activator of transcription
STAU1	Staufen homolog 1
STN1	Staphylococcal nuclease and tudor domain containing 1
TBK1	TANK-binding kinase 1
$TCID_{50}$	50% tissue culture infective dose
TLR	Toll-like receptor
TOM40	Translocase of the outer membrane 40
TRAF	Tumor necrosis factor receptor-associated factor
VISA	Virus-induced signaling adapter
VSV	Vesicular stomatitis virus
wt	Wild-type
$\Delta\Psi_m$	Mitochondria inner membrane potential

8.7 Publications

Original publications

Schmitt S*****, **Saathoff F***, Meissner L, Schropp EM, Lichtmannegger J, Schulz S, Eberhagen C, Borchard S, Aichler M, Adamski J, Plesnila N, Rothenfusser S, Kroemer G, Zischka H. (2013). "A semi-automated method for isolating functionally intact mitochondria from cultured cells and tissue biopsies." Anal Biochem **443**(1): 66-74. *****shared first authorship

Senft D, **Saathoff F**, Berking C, Kammerbauer C, Weber A, Häcker G, Rothenfusser S, Heppt M, Kellner S, Ruzicka T, Besch R. Cell survival depends on antiapoptotic Bcl-2 proteins in the absence of apoptotic stimuli. Manuscript in preparation, 2014

Oral presentations

Saathoff F, Characterization of the antiviral signaling molecule MAVS. 5th Annual Retreat, Graduiertenkolleg 1202, Sylvensteinsee, Germany, 2010

Saathoff F, SILAC – A new tool for the characterization of innate immune signaling. 3rd Autumn School, Deutsche Gesellschaft für Immunologie, Bad Schandau, Germany, 2011

Saathoff F, Powering through viral infection - The role of mitochondria in innate immunity. 7th Annual Retreat, Graduiertenkolleg 1202, Frauenchiemsee, Germany, 2012

Saathoff F, The role of mitochondria in innate immunity. Symposium Gentianum, Frauenchiemsee, Germany, 2013

Poster presentations

Lietke S, Schmidt S, Holbein W, **Saathoff F**, Höchter D, Linder N, Endres S, Rothenfusser S. Characterization of the novel antiviral protein SFP1. TOLL2011 – Decoding innate immunity. Riva del Garda, Italy

Saathoff F, Schmitt S, Schmidt A, Wisskirchen C, Hirschberger S, Macke L, Lietke S, Meissner F, Zischka H, Endres S, Rothenfusser S. Proteomic screening of mitochondria: A new tool to identify novel antiviral proteins. Cell Symposia: Mitochondria – from signaling to disease, Lisbon, Portugal, 2013

Antón S, Pandey D, Rueckel J, **Saathoff F**, Protzer U, Endres S, Rothenfußer S. TRIM9, a new modulator of innate immune responses. 44. Jahrestagung der Deutschen Gesellschaft für Immunologie DGfI, Bonn, Germany, 2014

9 Acknowledgement

First of all, I would like to sincerely thank Prof. Dr. med. Simon Rothenfusser and Prof. Dr. med. Dr. rer. nat. Carole Bourquin for giving me the opportunity to perform my PhD thesis in this highly interesting field of research and creating an atmosphere of independent working routine. Their personal encouragement and scientific input were truly inspiring.

I also thank Prof. Dr. med. Stefan Endres for the possibility to work in the division of Clinical Pharmacology as a member of the DFG Graduiertenkolleg 1202 "Oligonukleotide in Zellbiologie und Therapie".

Furthermore, I particularly thank my collaboration partners Dr.rer.nat Felix Meissner, Dr. rer. nat Hans Zischka, Dr. med Soeren Gersting, Dr. med Amelie Lotz-Havla and Dr. rer. hum. biol. Robert Besch for their active contribution to the presented research projects and partially ongoing publications.

Last but not least, I thank my fellow doctoral students and co-workers for their contribution to the experimental outcome of this work and for a highly inspiring and extraordinary working atmosphere.

10 Curriculum vitae